Fluid-structure interaction in the aortic heart valve : a three-dimensional computational analysis

Fluid-Structure Interaction in the Aortic Heart Valve

a three-dimensional computational analysis

CIP-DATA LIBRARY TECHNISCHE UNIVERSITEIT EINDHOVEN

Hart, Jurgen de

Fluid-structure interaction in the aortic heart valve : a three-dimensional computational analysis / by Jurgen de Hart. - Eindhoven : Technische Universiteit Eindhoven, 2002.
Proefschrift. - ISBN 90-386-2803-X
NUGI 743
Trefwoorden: aortaklep / hartklepprothesen / aortaklepbewegingen / cardiovasculaire bloedstroming / vloeistof-vaste stof interactie / eindige-elementenmethode / fictitious domain methode / arbitrary Lagrange-Euler methode / vezelversterking / aortawortel-compliantie / materiaalspanningen / vloeistofsnelheidsvelden
Subject headings: aortic valve / heart valve prostheses / aortic valve motion / cardiovascular bloodflow / fluid-structure interaction / finite element method / fictitious domain method / arbitrary Lagrange-Euler method / leaflet fiber-reinforcement / aortic root compliance / structural stresses / fluid velocity fields

Reproduction: Universiteitsdrukkerij TU Eindhoven, Eindhoven, the Netherlands

Fluid-Structure Interaction in the Aortic Heart Valve

a three-dimensional computational analysis

PROEFSCHRIFT

ter verkrijging van de graad van doctor aan de
Technische Universiteit Eindhoven, op gezag van de
Rector Magnificus, prof.dr. R.A. van Santen, voor een
commissie aangewezen door het College voor
Promoties in het openbaar te verdedigen
op vrijdag 1 maart 2002 om 16.00 uur

door

Jurgen de Hart

geboren te Nieuwkuijk

Dit proefschrift is goedgekeurd door de promotoren:

prof.dr.ir. F. P. T. Baaijens
en
prof.dr.ir. H.E.H. Meijer

Copromotor:
dr.ir. G.W. M. Peters

Contents

Summary

Quality of life can be improved if a diseased heart valve is replaced by a prosthetic device. Although diseases of any of the heart valves can compromise health, diseases of the aortic valve occur most frequently and result in more dire consequences, which therefore puts greater importance on the function of this valve. The natural aortic valve is unique in its accomplishment, since no prosthetic device yet can serve the function with the same efficiency and durability. Studies on medical complications in currently used substitutes involve many expensive and time-consuming experiments. Moreover, the development of improved prostheses or new concepts is still largely based on empirical knowledge and understanding. The application of numerical techniques in valve modeling has mainly been focused on the valve structure rather than considering the fluid-structure interaction. This complex interaction between the blood and the valve leaflets, aortic root and wall is essential in the response of the system to its physiological loading. Consequently, clinical assessment of a valve prosthesis requires that both mechanical and hemodynamical aspects need to be evaluated.

A fluid-structure interaction model, based on the Galerkin finite element method, is developed which is used to study the effect of fluid-structure interaction, leaflet fiber-reinforcement and aortic root compliance on the systolic aortic valve functioning. In general, the model can be used to resolve problems associated with failure and medical complications of diseased valves and currently used prosthetic devices.

Modeling of such a fluid-structure interaction system is complicated by the large but finite motion of the thin leaflets through the computational fluid domain. The mathematical formulation of the equation of motion for the fluid is most conveniently described with respect to an Eulerian reference frame. This is, however, incompatible with the Lagrangian formulation, which is more appropriate to describe the structure. Conventional mesh update strategies (e.g. remeshing and arbitrary Lagrange-Euler techniques) to accommodate the fluid domain for the leaflet motion are, for their limitations, not adopted in this study. Instead, a Lagrange multiplier based fictitious domain method is used to describe the interaction with the valve leaflets. With this method, the different mathematical descriptions for the fluid and structure can be maintained, allowing convenient classical formulations for each of these phases. Moreover, the fluid mesh is not altered or interrupted by the presence of the immersed domain, which therefore preserves its quality. This method is validated experimentally for the two-dimensional case and has proven to be applicable for describing the blood-leaflet interaction. The interaction between the blood and the compliant aortic root and wall is, on the other hand, described with the commonly adopted arbitrary Lagrange-Euler method, for which a proper fluid mesh quality is maintained throughout the analysis.

The geometrical properties of the valve model are taken from available literature on the natural valve and synthetic prototype valve prostheses. The fluid is modeled as a Newtonian fluid with blood analog characteristics. The non-linear, anisotropic material behaviour of the leaflets is incorporated by applying fiber-reinforcement resulting in a stress-strain relation, which is physiologically representative. The material behaviour of the aortic root and wall is assumed to be linear elastic and isotropic. Flow and pressure variables are used to feed the model, giving a characteristic Reynolds and Strouhal number of 1500 and 0.12, respectively.

The system is solved in a fully coupled manner leading to a simultaneously obtained solution of the fluid and structure unknowns. Consequently, these unknowns are directly in equilibrium obviating the need for additional iteration schemes to couple the two phases. The fluid mesh is accommodated explicitly for the moving aortic root and wall and a Newton-Raphson iteration process is used to arrive at an equilibrium state of the total, non-linear system, i.e. blood, leaflets and aortic root and wall. The BiCGStab iterative solver is adopted to solve the linearized equations using an appropriate preconditioning matrix based on an incomplete LU factorization.

The application of leaflet fiber-reinforcement substantially improves the mechanical properties of the structure, while the fluid dynamical performance is preserved. Aortic root compliance appears to be important for the valve opening configurations and significantly reduces leaflet bending deformations. The combination of the fictitious domain method for blood-leaflet interaction and arbitrary Lagrange-Euler method for blood-wall interaction successfully describes systolic valve functioning. Applying the adopted method to the diastolic phase remains a problem as the number of blood-leaflet coupling constraints must be increased to prevent flow through the leaflet structure. This involves application of additional Lagrange multipliers, which affects the solvability of the system matrix. However, since the fluid dynamics are less significantly present during this phase, the diastolic valve mechanics can be analyzed with appropriate, previously developed, structural models.

In conclusion the model presented in this thesis is useful as an analysis tool to improve existing valve prosthesis and to develop new prosthetic valve concepts. Moreover, within the clinical practice the model can, in the near future, serve as a possible diagnostic tool giving additional input for choosing the time and type of surgical intervention in the diseased aortic valve system.

Notation

Quantities

a	scalar
$\vec{a}$	vector
$\boldsymbol{A}$	second order tensor
$\boldsymbol{I}$	second order unity tensor
${}^4\boldsymbol{A}$	fourth order tensor
$\underline{A}$	matrix
$\underset{\sim}{a}$	column

Operations

$\vec{\nabla}a$, $\vec{\nabla}\vec{a}$	gradient
$\boldsymbol{A}^T$, $\underline{A}^T$, $\underset{\sim}{a}^T$	transposition
$\boldsymbol{A}^{-1}$, $\underline{A}^{-1}$	inversion
$\vec{a} \cdot \vec{b}$	inner vector product
$\boldsymbol{A} \cdot \boldsymbol{B}$	inner tensor product
$\boldsymbol{A} : \boldsymbol{B}$	double inner product
$\det(\boldsymbol{A})$	determinant of a tensor
$\mathrm{tr}(\underline{A})$	trace of a matrix
$\frac{\mathrm{D}a}{\mathrm{D}t}$	material time derivative
$\frac{\partial a}{\partial t}$	spatial time derivative
$\lvert\vec{a}\rvert$	maxnorm of a vector
$\lVert\underline{A}\rVert$	determinant of a matrix

Dimensionless numbers

Re	Reynolds number
Sr	Strouhal number
α	Womersly number

Chapter 1

General Introduction

The study on improved aortic valve prostheses that are able to adopt the physiological performance and durability of the healthy natural valve requires knowledge of the interaction between the valve and the blood. A short introduction is given on the morphology and functioning of the natural aortic valve system. The mechanical and hemodynamical complications of currently used substitute valves are summarized, expressing the strong need for numerical fluid-structure interaction models that are applicable to predict the functioning of existing and new prosthetic designs or to analyze the performance of diseased valves. The objective of this study is given followed by the outline of the thesis.

1.1 Introduction

The aortic valve is one of the four valves which control the blood flow through the heart. It is situated at the outlet of the left ventricle just prior to the ascending aorta (Figure 1.1). This valve opens with minimal resistance to allow blood to flow into the aorta, and closes to prevent non-trivial back flow into the ventricle. Although diseases of any of the heart valves can compromise health, diseases of the aortic valve occur most frequently and result in more dire consequences (Schoen *et al.*, 1999), which therefore puts greater importance on the function of this valve. There are several ways by which the aortic valve can become diseased, however, all diseased valves present themselves as being stenotic, incompetent, or both (Thubrikar, 1990).

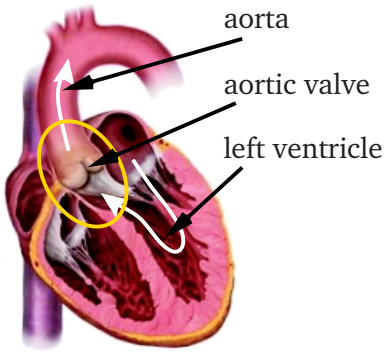

Figure 1.1: *Schematic sagittal cross section of the heart showing the aortic valve.*

Aortic stenosis offers significant obstruction to the forward blood flow. Common causes for pure aortic stenosis are calcification and cuspid fibrosis (Passik *et al.*, 1987; Subramanian *et al.*, 1984). Incompetent aortic valves allow blood to flow back into the left ventricle, thereby reducing the net forward flow. This insufficiency has been observed to occur either by itself or in association with aortic stenosis. Common causes for pure aortic insufficiency are rheumatic heart disease, permanent aortic root dilation and congenital effects (e.g. bicuspid or quadricuspid valves) (Olson *et al.*, 1984; Thubrikar, 1990).

Some degree of valve stenosis or incompetence can be tolerated without compromising health. In many cases, however, valve replacement is desired using a prosthetic device. Although currently used prosthetic valves perform the same task, the natural aortic valve is unique in its accomplishments, since no prosthetic device, to date, can serve that function with the same efficiency and durability. Hence, there is still a need for design improvement of existing valves and/or development of new concepts.

1.2 The natural aortic valve

1.2.1 Morphology

The natural valve consists of three highly flexible leaflets and three sinus cavities ('sinuses of Valsalva'), see Figure 1.2. Two functional areas can be distinguished in each leaflet. The area near the free edge is known as the coaptive area and is called the

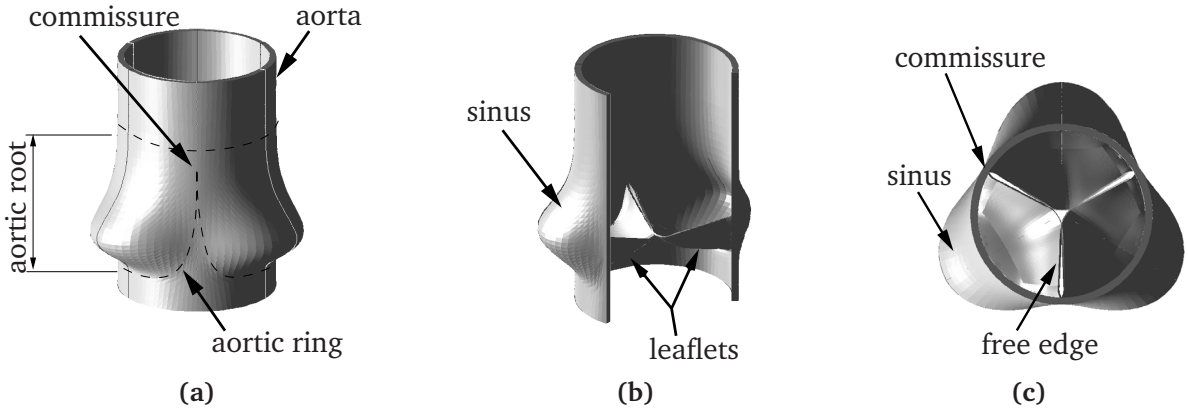

Figure 1.2: *Schematic representation of the aortic valve: (a) side view of the complete valve, (b) after dissection of one leaflet with corresponding sinus wall and, (c) aortic view.*

lunulea because of its semilunar shape. When the valve is closed the outlet orifice of the left ventricle is sealed because the lunulea of adjacent leaflets are coincident with each other. In the middle of the free edge of each lunulea a structural thickening ('nodulus of Arantius') is located, which is believed to permit a significant reduction in the height of the lunulea without causing central regurgitation during a closed valve configuration.

The remaining, non-coaptive area of the leaflet surface is referred to as the load bearing portion. This part constitutes a fiber-reinforced composite texture of elastin, but mainly collagen, fibers embedded in a matrix of endothelial cells. More precisely, this texture has a three-layered structure containing elastin and collagen fibers at the ventricular surface (*ventricularis*), acid mucopolysaccharides and some collagen fibers in the central layer (*spongiosa*) and a dense network of collagen fibers near the aortic surface (*fibrosa*). A similar layered structure is present in the lunulea, however, the arrangement of the fibers may be very irregular.

The dense collagen network in the *fibrosa* is essential for the mechanical behaviour of the leaflets. Originating at the commissures these collagen fibers run circumferential like the free edge and spread out over the whole leaflet as shown in Figure 1.3. In addition to these commissural fibers, discrete macroscopically visible bundles perpendicular to the attachment line, which is referred to as annulus fibrosis or aortic ring, anchor the

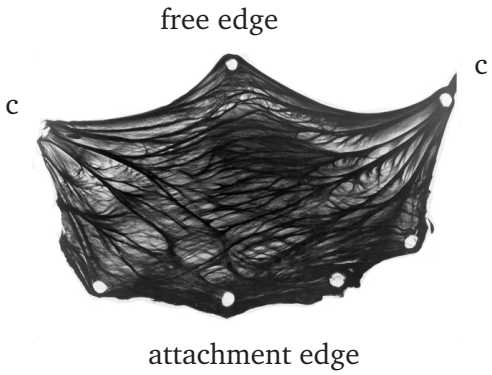

Figure 1.3: *Typical fiber structure in the aortic valve leaflets (from Sauren (1981), with permission). The commissural points are denoted by 'c'.*

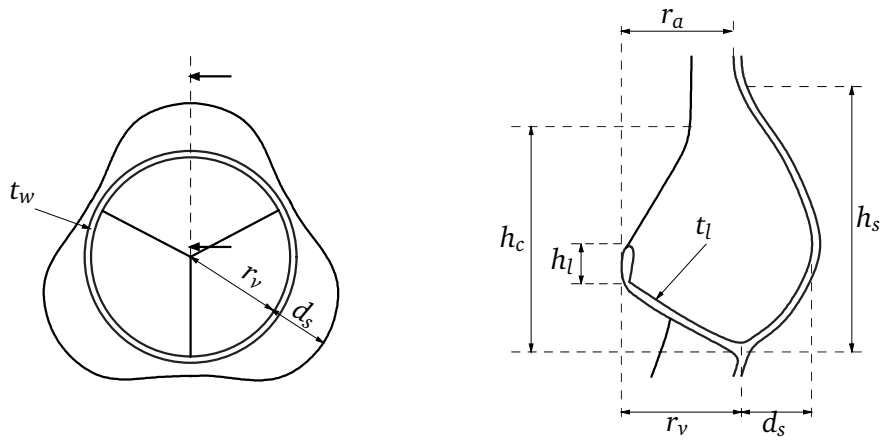

Figure 1.4: *Definition of relevant dimensions, which are frequently used to describe the geometry of the aortic valve: r_v denotes the ventricular valve radius, r_a the aortic valve radius, d_s the sinus depth, h_s the sinus height, h_c the commissural height, h_l the coaptation height of the lunulea, t_l the leaflet thickness and t_w the aortic wall thickness.*

middle portion of the leaflet to the aortic wall (Sauren, 1981). This line of attachment of each leaflet forms a U-shaped arch, which also bounds the sinus behind the leaflet. The top of the arches where the lunulea of adjacent leaflets merge into the aortic ring, are called commissures.

The sinuses are dilated pouches of the aortic root (Figure 1.2(a)), which are thinner than the aortic wall. The wall texture contains mainly circumferential arranged smooth muscular tissue embedded in a network of arbitrarily oriented elastin fibers with scattered small collagen fibers.

The term ”aortic valve” will be taken to apply to the part of the aortic root consisting of the leaflets and the sinus walls, bounded at the ventricular or inflow side by the aortic ring and at the aortic or outflow side by the circle that is obtained by the intersection of the transversal plane through the sinus tops and the aortic wall (Sauren, 1981). This definition includes the portions of the aortic wall, that are bounded by this circle and the aortic ring (Figure 1.2(a)).

The difficulty in describing the geometry of the aortic valve is illustrated by the paucity of available data. Various dimensions of the aortic valve have been measured using different techniques in several mammalian species (Reid *et al.*, 1970; Sands *et al.*, 1969; Swanson *et al.*, 1974). The dynamical behaviour of the valve is attended with variation of these dimensions (Van Renterghem, 1983). Figure 1.4 shows some definitions of relevant dimensions that have frequently been used to describe the geometry of the valve and Table 1.1 summarizes typical values measured in adult humans. Al-

	r_v	r_a	d_s	h_s	h_c	h_l	t_l	t_w
Dimension [mm]	12.0	11.4	5.52	20.9	17.5	4.08	0.20	1.03
Authors	[1]	[1]	[1]	[1]	[1]	[1]	[2]	[3]

Table 1.1: *Typical dimensions of the unloaded human aortic valve measured by [1] Swanson et al. (1974), [2] Clark et al. (1974) and [3] Shunk et al. (2001).*

though, the three leaflets are not precisely identical, it is assumed that they are similar enough to permit a general description of a valve with trileaflet symmetry.

The morphological description of blood is confined to a concentrated suspension of red blood cells (erythrocytes), white blood cells (leucocytes) and platelets in plasma. Plasma is the continuous liquid medium in which the blood cells are suspended. It is an aqueous saline solution containing proteins. The deformable red blood cells occupy 45% of the blood volume and dominate the rheological behaviour of blood. They aggregate when brought in contact with each other at low shear rates, emphasizing the importance of blood wash-out in potential stagnant flow regions, such as the sinus cavities. The far less numerous white blood cells are of minor importance if their relation to the rheological characteristics of blood is considered. Platelets are much smaller constituents of blood, which exhibit a considerably higher rigidity. In contact with adenosine diphosphate (ADP) they tend to aggregate and can form a thrombus; a phenomenon which is frequently observed in stenotic valves. The composition of blood as described above, as well as the properties of the constituents, lead to a complex rheological behaviour, which shows shear thinning and viscoelasticity.

A study on valve and blood morphology would far exceed the scope of this thesis. The interested reader is referred to Thubrikar (1990) and Caro *et al.* (1978) for a more complete description of the aortic valve and blood.

1.2.2 Functioning

The cardiac cycle can be divided into a systolic and diastolic interval, see Figure 1.5. During systole an isovolumic contraction of the left ventricle is followed by the ejection of blood into the aorta. The aortic valve remains open during this interval. At diastole an isovolumic relaxation precedes a filling of the left ventricle with blood from the atria. During this interval the aortic valve remains closed. Both mechanical and kinematical aspects are involved in valve functioning and differ in importance during the course of the cardiac cycle.

In one cardiac cycle three main phases can be distinguished in valve performance: the opening and closing phases during systole and the closed phase during diastole

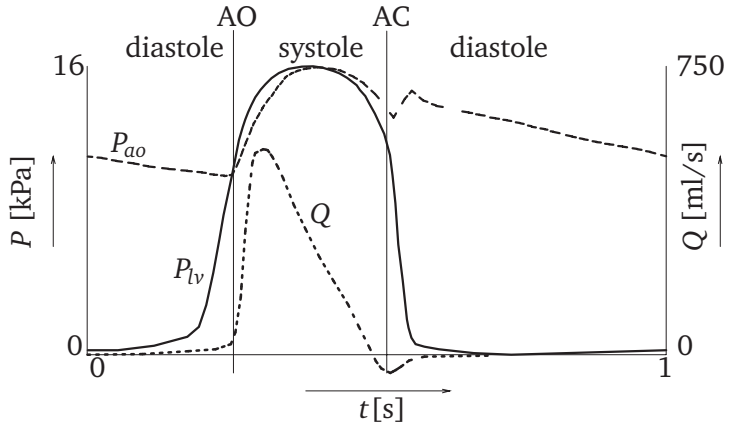

Figure 1.5: *Sketch of the aortic (P_{ao}: dashed line) and left ventricular (P_{lv}: solid line) pressure curves during the cardiac cycle. The associated flow curve is also given (Q: dotted line). AO denotes the onset of valve opening and AC the moment of complete closure.*

(Sauren, 1981). In the normal situation valve opening is very fast (25 to 35 [ms]). The leaflets start to bulge towards the aorta just before ventricular ejection begins. The valve is completely open when the peak flow in the ascending aorta has reached 75% of its maximum (Van Steenhoven *et al.*, 1981). Although the Reynolds number[1] reaches up to 4500 at peak flow, it appears that in the case of properly working heart valves, the fluid flow remains laminar (Nerem *et al.*, 1972). Only when a valve exhibits a malfunctioning, some turbulence might be expected.

As to valve closing two phases can be distinguished. The first is the gradual closing of the valve that starts during the deceleration of the aortic flow, resulting in about 80% valve closure at the moment of zero flow in the ascending aorta at the end of the systole (Thubrikar, 1990). The flow phenomena during this phase are rather complex and can be characterized by the Strouhal number[1] ($Sr \approx 0.06$). In this phase vortices are initiated in the sinus cavities, which are thought to instigate early valve closure. Followed by the adverse pressure gradient during flow deceleration, a small reverse flow finally completes closure. Similar findings were reported by Van Steenhoven (1979) and Van Steenhoven *et al.* (1981) in *in vivo* experiments. Moreover, they observed that the valve has already closed by about 10% at the onset of flow deceleration and that complete closure coincides with maximum back flow in the ascending aorta.

Being thin and highly flexible membrane-like structures, the valve leaflets cannot withstand any significant pressure difference during the opening and first closing phase. During these phases the leaflets may be expected to move with the fluid in an essentially kinematical process governed by the fluid motion. In the course of diastole the leaflets have to withstand a slowly varying but nonetheless considerable pressure load (Figure 1.5). Numerical modeling of the valve behaviour during systole is complex, but challenging, because of its highly dynamical character, and important as it provides insight in system responses, which are difficult to obtain experimentally.

The aortic valve has been generally thought of as a passive structure where all of its mobile components move only as a result of blood flow. It has been shown, however, that the commissures move outward in a passive response to pressure resulting in an increase of the aortic valve radius (r_a in Figure 1.4) (Brewer *et al.*, 1976). Moreover, the ventricular valve radius (r_v) decreases in an active response to myocardial contraction in systole (Thubrikar *et al.*, 1980). Commissural movement is made possible because of the elasticity of the sinus walls. When the aortic root is not dilated, valve function and geometry become abnormal and high leaflet deformations occur that initiate calcification and/or tearing, ultimately leading to a diseased valve (Fisher, 1995).

1.3 Prosthetic heart valves

Quality of life can be improved if a diseased heart valve is replaced by a prosthetic device. There are several types of substitutes for replacement of the aortic valve. The most commonly used devices are mechanical and bioprosthetic valves. More than 170,000 patients receive a prosthesis worldwide each year. Of the valves used, 50 to 55% are mechanical and the remaining are bioprostheses. The clinical performance of the pros-

[1] Flow phenomena are frequently characterized by the Reynolds number (*Re*), defining the ratio of stationary inertia and viscous forces, Strouhal number (*Sr*) defining the ratio of instationary and stationary inertia forces or Womersly number (α) defining the ratio of instationary inertia and viscous forces.

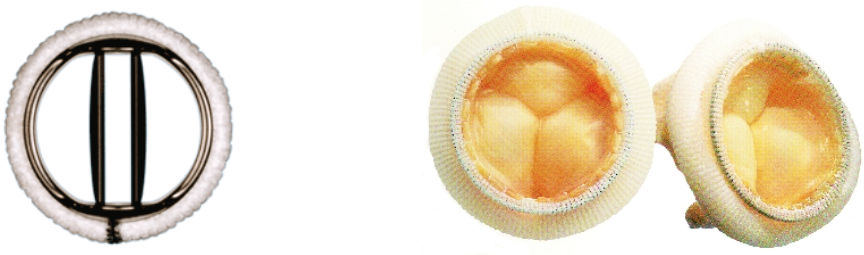

(a) **(b)**

Figure 1.6: *Heart valve prostheses: (a) St. Jude Medical bileaflet prosthesis, (b) Hancock porcine bioprosthesis.*

thesis is evaluated by its hemodynamics, e.g. obstruction to forward flow, and durability, which for both valve types differ significantly. Within 10 years postoperative complications necessitate re-operation or cause death in 50 to 60% of the patients having either prosthetic type (Schoen *et al.*, 1999). Moreover, the failure rate is nearly 100% in 5 years for patients with a biological substitute that are younger than 35 years old.

Mechanical valves are available in different designs of which the ball and cage (e.g. Starr-Edwards ball valve) or tilting disc (e.g. Bjork-Shiley tilting disc valve or St. Jude Medical bileaflet valve (Figure 1.6(a)) types are most frequently used (Morse *et al.*, 1985). In designing a mechanical valve several aspects should be considered. The weight of the ball or disc, contact surface, reactivity to blood components, tendency to cause hemolysis, and flow characteristics are some of the parameters that must be controlled. These prostheses are characterized by their good durability. However, the rigid structure also reflects in poor hemodynamical performance, requiring a life-long pharmaceutical support to prevent thromboembolic complications. If these valves could be made non-thrombogenic in the future, their use could become a much more desirable treatment for diseased heart valves in humans.

Bioprosthetic valves are made of chemically treated animal tissue. In particular porcine aortic valves (e.g. Hancock porcine valve, see Figure 1.6(b)) or bovine pericardium (e.g. Ionescu-Shiley pericardial valve), both treated with buffered gluteraldehyde, are used. The treatment of gluteraldehyde prevents tissue digestion by enzymes or bacteria, preserves the tissue, and eliminates tissue rejection (Schoen, 1987). However, this treatment also stiffens the tissue, although unintentionally. Flexible, trileaflet, biological tissue valves mimic their natural counterparts more closely than do mechanical valves. Their central flow characteristics enhance hemodynamic efficiency and their biological surface enhances thromboresistance as compared to mechanical prostheses. However, most bioprostheses fail by calcific degeneration and/or tissue degeneration caused by mechanical stress. Research towards improved bioprostheses is therefore mainly focused on increasing the tissue strength and thus its durability.

Besides these commercially available prosthetic types there is a growing interest in the development of synthetic valves. They allow more freedom in optimizing the design in terms of durability and valve hemodynamics. Most synthetic prostheses are stented flexible trileaflet valves of polyurethane. *In vitro* tests show, however, that durability is up to now not significantly improved to use these valves for implantation. The concept of fiber-reinforcement has been used by Cacciola (1998) to strengthen the valve leaflets preserving its flexibility, and thus its hemodynamics. Numerical studies by De Hart *et*

al. (1998) and Cacciola (2000) have shown that leaflet fiber-reinforcement significantly reduces peak stresses at areas that are susceptible to degeneration. These prototype valve prostheses require further investigation on their applicability for implantation.

Particularly exciting in concept, yet early in practice are tissue engineered heart valves. Recently, there is considerable activity in basic research and clinical investigation to develop this technique in which an anatomically appropriate construct containing cells seeded on a resorbable scaffold is fabricated *in vitro*. Stimulated and guided by appropriate mechanical and chemical signals, biological remodeling is intended to recapitulate normal function architecture (Hoerstrup *et al.*, 2000; Sodian *et al.*, 2000). Moreover, remodeling of the tissue is inclined to proceed after implantation of the construct. Possibly, these features make tissue-engineered valves desired substitutes in the future.

1.4 Objective and outline of this study

From the previous section it is clear that there is a strong need for an aortic valve prosthesis that can mimic the function of the natural valve with such an efficiency and durability that postoperative medical treatment becomes redundant. At this time the development of improved prostheses involves many expensive and time-consuming experiments to gain knowledge and understanding of such a complex system. The delicate interaction between the valve and the surrounding blood requires that in these experiments both the mechanical and hemodynamical aspects of the valve must be considered. It should be emphasized that this strong interaction is essential for the response of the system to its physiological loading.

The application of numerical models enhances the development of improved valve prostheses by significantly reducing the number of experiments required and giving insight in system responses that cannot or hardly be obtained experimentally. However, the models currently used lack the capacity to analyze the systolic mechanical and hemodynamical valve behaviour for physiological conditions. The objective of this study is to develop a numerical model to investigate the effect of fluid-structure interaction, leaflet fiber-reinforcement and aortic root compliance on systolic aortic valve functioning. In general, this model could be used to resolve the problems associated with the failure and medical complications of diseased valves and currently used prosthetic devices.

To enhance clinical relevance a three-dimensional finite element model is developed to perform analyses that closely resemble the physiological conditions under which the aortic valve system operates. Realistic material characteristics are adopted to incorporate the fiber-reinforced leaflet structure. The model is based on a set of geometrical parameters, material parameters and appropriate boundary conditions, such that it can be used to analyze different valve designs under various loading conditions. Hence, the model can possibly be used as a numerical design tool for valve prostheses as well as a diagnostic tool for clinical purposes in the near future. Moreover, the methods used in this model can generally be applied to study blood-tissue interaction within other cardiovascular subsystems, such as flow in large arteries, carotid artery bifurcation or coronary arteries.

Based on the fictitious domain method a new fluid-structure interaction algorithm is

developed, which allows for finite motion of flexible structures such as the valve leaflets. This algorithm is experimentally validated for a 'quasi' two-dimensional situation that mimics the aortic valve system (Chapter 2). To study the effect of fluid-structure interaction on the behaviour of the leaflets a three-dimensional representation is required. To this end, the fictitious domain method is extended for three-dimensional situations and applied to a stented aortic valve (Chapter 3). Biological and synthetic prostheses tend to fail due to material degeneration induced by high stresses. These stresses are assumed to be reduced by applying fiber-reinforcement to strengthen the leaflets. The impact of fiber-reinforcement on the mechanical and hemodynamical performance of a stented valve during the systolic phase is investigated using the three-dimensional model (Chapter 4). The effect of the compliance of the aortic root on the kinematics of the valve is investigated next for non-reinforced and reinforced valve types (Chapter 5). For this purpose the fictitious domain method and the arbitrary Lagrange-Euler method are combined to incorporate interaction of the fluid with the leaflets, aortic root and wall. Finally, a discussion of the presented techniques and results precedes the conclusions, which completes this thesis (Chapter 6).

The contents of Chapters 2 to 5 are based on separate articles, i.e. De Hart *et al.* (2000), De Hart *et al.* (2001a), De Hart *et al.* (2001b) and De Hart *et al.* (2002), which are published or have been submitted for publication. Hence, recurrence and overlap of methods and modeling descriptions occurs between these chapters.

References

Brewer, R.J., Deck, J.D., Capati, B., Nolan, S.P., 1976. The dynamic aortic root. *Journal of Thoracic and Cardiovascular Surgery*, **72**(3): 413-417.

Cacciola, G., 1998. *Design, Simulation and Manufacturing of Fiber-Reinforced Polymer Heart Valves.* Ph.D. thesis, Eindhoven University of Technology, Eindhoven. *http://www.mate.tue.nl/mate/publications*.

Cacciola, G., Peters, G.W.M., Schreurs, P.J.G., 2000. A three-dimensional mechanical analysis of a stentless fibre-reinforced aortic valve prosthesis. *Journal of Biomechanics*, **33**(5): 521-530.

Caro, C.G., Pedley, J.G., Schroter, R.C., Seed, W.A., 1978. *The Mechanics of the Circulation*. Oxford University Press, Oxford.

Clark, R.E., Finke, E.H., 1974. Scanning and light microscopy of human aortic leaflets in stressed and relaxed states. *Journal of Thoracic and Cardiovascular Surgery*, **67**(5): 792-804.

De Hart, J., Cacciola, G., Schreurs, P.J.G., Peters, G.W.M., 1998. A three-dimensional analysis of a fibre-reinforced aortic valve prosthesis. *Journal of Biomechanics*, **31**(7): 629-638.

De Hart, J., Peters, G.W.M., Schreurs, P.J.G., Baaijens, F.P.T., 2000. A two-dimensional fluid-structure interaction model of the aortic valve. *Journal of Biomechanics*, **33**(9):1079-1088.

De Hart, J., Peters, G.W.M., Schreurs, P.J.G., Baaijens, F.P.T., 2001a. A three-dimensional computational analysis of fluid-structure interaction in the aortic heart valve. Submitted to *Journal of Biomechanics*.

De Hart, J., Peters, G.W.M., Schreurs, P.J.G., Baaijens, F.P.T., 2001b. A computational fluid-structure interaction analysis of a fiber-reinforced stented aortic valve. Submitted to *Journal of Biomechanics*.

De Hart, J., Peters, G.W.M., Schreurs, P.J.G., Baaijens, F.P.T., 2002. A computational fluid-structure interaction analysis of a fiber-reinforced stentless aortic valve. Submitted to *Journal of Biomechanics*.

Fisher, J., 1995. Porcine bioprosthesis valves prepared with permanent predilitation of the aortic root: a review. *Journal of Heart Valve Disease*, **4**(1): S81-S83.

Hoerstrup, S.P., Sodian, R., Daebritz, S., Wang, J., Bacha, E.A., Martin, D.P., Moran, A.M., Guleserian, K.J., Sperling, J.S., Kaushal, S., Vacanti, J.P., Schoen, F.J., Mayer, J.E. Jr., 2000. Functional living trileaflet heart valves grown *in vitro*. *Circulation*, **102**(19 Suppl 3): 44-49.

Morse, D., Steiner, R.M., Fernandez, J., 1985. *Guide to prosthetic cardiac valves.* Springer-Verlag, NY.

Nerem, R.M., Seed, W.A., 1972. An *in vivo* study of aortic flow disturbances. *Cardiovascular Research*, **6**(1): 1-14.

Olson, L.J., Subramanian, R., Edwards, W.D., 1984. Surgical pathology of pure aortic insufficiency: a study of 225 cases. *Mayo Clinic Proceedings*, **59**(12): 835-841.

Passik, C.S., Ackermann, D.M., Pluth, J.R., Edwards, W.D., 1987. Temporal changes in the causes of aortic stenosis: a surgical pathologic study of 646 cases. *Mayo Clinic Proceedings*, **62**(2): 119-123.

Reid, K., 1970. The anatomy of the sinus of Valsalva. *Thorax*, **25**(1): 79-85.

Sands, M.P., Rittenhouse, E.A., Mohri, H., and Merendino, K.A., 1969. An anatomical comparison of human, pig, calf and sheep aortic valves. *The Annals of Thoracic Surgery*, **8**(5): 407-414.

Sauren, A.A.H.J., 1981. *The Mechanical Behaviour of the Aortic Valve*. Ph.D. thesis, Eindhoven University of Technology, Eindhoven.

Schoen, F.J., 1987. Cardiac valve prostheses: pathological and bioengineering considerations. *Journal of Cardiac Surgery*, **2**(1): 65-108.

Schoen, F.J., Levy, R.J., 1999. Tissue heart valves: current challenges and future research perspectives. *Journal of Biomedical Materials Research*, **47**(4): 439-465.

Shunk, K.A., Garot, J., Atalar, E., Lima, J.A.C., 2001. Transesophageal Magnetic Resonance Imaging of the aortic arch and descending thoracic aorta in patients with aortic atherosclerosis. *Journal of the American College of Cardiology*, **37**(8): 2031-2035.

Sodian, R., Hoerstrup, S.P., Sperling, J.S., Daebritz, S., Martin, D.P., Moran, A.M., Kim, B.S., Schoen, F.J., Vacanti, J.P., Mayer, J.E. Jr., 2000. Early *in vivo* experience with tissue-engineered trileaflet heart valves. *Circulation*, **102**(19 Suppl 3): 22-29.

Subramanian, R., Olson, L.J., Edwards, W.D., 1984. Surgical pathology of pure aortic stenosis: a study of 374 cases. *Mayo Clinic Proceedings*, **59**(10): 683-690.

Swanson, W.M., Clark, R.E., 1974. Dimensions and geometric relationships of the human aortic valve as a function of pressure. *Circulation Research*, **35**(6): 871-882.

Thubrikar, M., Nolan, S.P, Bosher, L.P., Deck, J.D., 1980. The cyclic changes and structure of the base of the aortic valve. *American Heart Journal*, **99**(2): 217-224.

Thubrikar, M., 1990. *The Aortic Valve*. CRC Press, Boca Raton, Florida.

Van Renterghem, R.J., 1983. *Aortic Valve Geometry During the Cardiac Cycle*. Ph.D. thesis, Eindhoven University of Technology, Eindhoven.

Van Steenhoven, A.A., van Dongen, M.E.H., 1979. Model studies of the closing behaviour of the aortic valve. *Journal of Fluid Mechanics*, **90**(1): 21-32.

Van Steenhoven, A.A., Verlaan, C.W.J., Veenstra, P.C., Reneman, R.S., 1981. An in-vivo cinematographic analysis of the behaviour of the aortic valve. *American Journal of Physiology*, **240**(2): H286-H292.

Chapter 2

A Fictitious Domain Method for Fluid-Structure Interaction in the Aortic Heart Valve[1]

The dynamic interaction of the aortic valve with the surrounding fluid is essential for the local deformations and stresses in the structure. A detailed analysis of the valve's kinematics and hemodynamics benefits from numerical modeling of this interaction. However, the large differences in material properties of the fluid and structure and the finite motion of the leaflets complicate blood-valve interaction modeling. This has impeded numerical analyses of valves operating under physiological conditions. A Lagrange multiplier based fictitious domain method is used to develop a new fluid-structure interaction algorithm, which allows for deformation of flexible structures such as the valve leaflets. The applicability is investigated for a two-dimensional representation that mimics the aortic valve system. The algorithm is validated experimentally using Laser Doppler anemometry to measure fluid flow phenomena and digitized High Speed video recordings to visualize the leaflet motion in corresponding geometries. Results show that the applied numerical techniques can be used to describe both the fluid and leaflet behaviour for different leaflet thicknesses.

[1]The contents of this chapter are published in the *Journal of Biomechanics*, **33**(9), 1079-1088, 2000:

A two-dimensional fluid-structure interaction model of the aortic valve
De Hart, J., Peters, G.W.M., Schreurs, P.J.G., Baaijens, F.P.T.

2.1 Introduction

Three-dimensional numerical models of artificial fiber-reinforced prototype valves have been developed by De Hart *et al.* (1998) and Cacciola (1998). In these models the physiological situation was simplified by applying the diastolic pressure difference over the valve, neglecting the interaction with the surrounding fluid. In reality, the opening and closing behaviour of the valve is a delicate interaction between blood flow, aorta and the heart valve leaflets. Numerical analysis of the opening and closing behaviour is complicated by the large three-dimensional motion of the highly flexible leaflets in a compliant system of fluid and structure. Fluid-structure interaction models of the heart valve have been developed before, e.g. see Peskin and McQueen (1994); Horsten (1990). However, none of these models represents the physiological conditions under which the valve functions because of numerical problems regarding the stability and solvability of the system.

In modeling fluid-structure interaction, the fluid is most conveniently described with respect to an Eulerian reference frame (material moves through the computational domain) while a Lagrangian formulation (computational domain moves with the material) is more appropriate for the structure. However, these formulations are incompatible. A solution to this problem is the use of an arbitrary Lagrange-Euler (ALE) formulation. This method involves a continuous adaptation of the mesh without modifying the mesh topology. ALE techniques are most commonly used in the aerospace field, where solid structures are subjected to complex airflows, e.g. see Farhat *et al.* (1998). In heart valves, however, the large deformation of the thin leaflets within the computational fluid domain complicates mesh adaptation without changing the topology, while preserving a proper mesh quality.

Alternatively, remeshing can be performed, either continuously or in conjunction with an ALE formulation, where remeshing is performed if the mesh quality has degenerated too much. Remeshing, however, not only introduces artificial diffusivity, it also may be difficult to perform with sufficient robustness and accuracy for three dimensional problems. To resolve this a fictitious domain method (Glowinski *et al.*, 1994; Bertrand *et al.*, 1997) is used where the fluid is described in an Eulerian setting, and the structure in a Lagrangian setting, allowing the use of the classical finite element method (FEM) with available software.

The method is based on the imposition of velocity constraints associated with moving internal boundaries by means of Lagrange multipliers. It has similarity with the so-called immersed boundary technique of Peskin and McQueen (1994) in which at a number of control points tension forces are imposed and distributed to neighbouring nodes. Numerical instabilities, however, limited Peskin and McQueen to analyze physiological flows. The method described in this chapter allows coupling of domains with dissimilar element distributions and/or interpolation order using Lagrange multipliers on a fictitious boundary representing the actual structure, see Baaijens (2001). The current implementation will be described for the two-dimensional case, is validated experimentally.

First, the fluid and structural problems are defined and the equations governing these problems are given. Next, the fluid-structure coupling, using Lagrange multipliers, is discussed. A description is given of the adopted solution techniques to solve the

resulting set of equations associated with a two-dimensional model of a flexible leaflet in a pulsatile flow. The experimental techniques to measure the physical quantities, which are used to validate the numerical model, are outlined. Finally, the numerical results are compared with the data obtained from the experiments for both the leaflet motion and fluid flow.

2.2 Problem definition and governing equations

A two-dimensional representation of the valve is shown in Figure 2.1, where a flexible leaflet is immersed in a pulsatile flow within, for this case, a rigid channel. The channel has height h and length $6h$ and contains a sinus cavity in the middle at the top wall with radius r. A flexible leaflet with length l and thickness t_l is attached to the top wall, just before the sinus cavity, at an angle α. The fluid domain is denoted by Ω_f and structural domain by Ω_s. The fluid-structure interface boundary is denoted by γ.

In this system a laminar flow is assumed of a fluid which behaves isothermal, incompressible and Newtonian. The momentum and continuity equations, which govern the mathematical formulation of the fluid domain Ω_f, are given by

$$\rho_f \frac{\partial \vec{v}_f}{\partial t} + \rho_f \vec{v}_f \cdot \vec{\nabla} \vec{v}_f = \vec{\nabla} \cdot (-p_f \boldsymbol{I} + \boldsymbol{\tau}_f), \tag{2.1}$$

$$\vec{\nabla} \cdot \vec{v}_f = 0, \tag{2.2}$$

where ρ_f denotes the density, t the time, $\vec{v}_f$ the velocity, p_f the pressure, $\boldsymbol{\tau}_f$ the extra stress tensor and $\vec{\nabla}$ the gradient operator. For Newtonian fluids the extra stress tensor $\boldsymbol{\tau}_f$ can be written as a function of the rate of deformation tensor $\boldsymbol{D}_f = \frac{1}{2}(\vec{\nabla}\vec{v}_f + (\vec{\nabla}\vec{v}_f)^T)$:

$$\boldsymbol{\tau}_f = 2\eta \boldsymbol{D}_f, \tag{2.3}$$

where η denotes the dynamic viscosity of the fluid. The well-known Navier-Stokes equation results from substitution of (2.3) into (2.1).

Scaling spatial coordinates with a characteristic length, e.g. the channel height h, velocities with a characteristic velocity, e.g. the peak velocity V of the mainstream and time with a characteristic time, e.g. the flow deceleration time τ, the dimensionless (*)

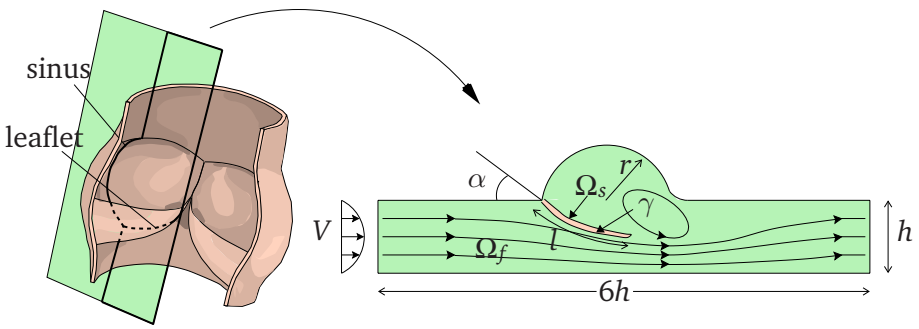

Figure 2.1: *Two-dimensional representation of the aortic valve.*

representation of the Navier-Stokes equation is given by

$$Sr\frac{\partial \vec{v}_f^*}{\partial t^*} + \vec{v}_f^* \cdot \vec{\nabla}^* \vec{v}_f^* = -\vec{\nabla}^* p_f^* + \frac{1}{Re} 2\vec{\nabla}^* \cdot \boldsymbol{D}_f^*, \tag{2.4}$$

where the Strouhal number Sr and the Reynolds number Re are defined as

$$Sr = \frac{h}{\tau V}, \qquad Re = \frac{\rho_f V h}{\eta}. \tag{2.5}$$

The density of the leaflet material is taken equal to the fluid density, so that buoyancy forces can be neglected. Moreover, the contribution of the leaflet's inertia is not taken into account, since the leaflet mass is negligible with respect to the considered fluid mass. In absence of any body forces the momentum equation for the structural domain Ω_s thus yields

$$\vec{\nabla} \cdot \boldsymbol{\sigma}_s = \vec{0}, \tag{2.6}$$

where $\boldsymbol{\sigma}_s$ is the structural Cauchy stress tensor. The large rotations of the nearly incompressible, isotropic leaflet are accompanied by small strains. For this reason the leaflet is assumed to behave linear elastic according to Hooke's law:

$$\boldsymbol{\sigma}_s = {}^4\boldsymbol{C} : \varepsilon_s; \qquad \varepsilon_s = \frac{1}{2}\left(\vec{\nabla}\vec{u}_s + (\vec{\nabla}\vec{u}_s)^T\right), \tag{2.7}$$

where ${}^4\boldsymbol{C}$ represents the fourth-order Hookean elasticity tensor, ε_s the elastic strain tensor and $\vec{u}_s$ the structural displacement field. The material properties of this structure are fully determined by the Young's modulus E and the Poisson's ratio ν.

There is a distinct difference between Equation (2.1) and (2.6) that in the momentum equation of the fluid the domain is known and fixed in space (Eulerian), while the position of the structural domain is not known *a priori*. As a consequence the gradient operator in (2.6) depends on the solution, i.e. the leaflet position, while the gradient operator in (2.1) is independent of the velocity field $\vec{v}_f$. This situation changes whenever the computational domain of the fluid is adapted to the computed velocity field, for instance to follow the motion of the immersed structure. In the method described here the fluid domain is fixed in space.

The above set of equations will be complemented with appropriate coupling and boundary conditions, which will be discussed next.

2.3 Fluid-structure coupling and implementation

In the Lagrange formulation of the structure the displacement field $\vec{u}_s$, defined as the difference in position at two successive time points t^n and t^{n+1}, is the unknown. The structural velocity $\vec{v}_s$ during time interval $t^n \rightarrow t^{n+1}$ is taken to be related to the structural displacement $\vec{u}_s$ by the following first-order approximation:

$$\vec{v}_s = \frac{\vec{u}_s}{\Delta t}, \tag{2.8}$$

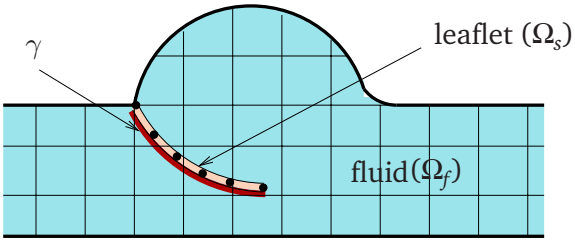

Figure 2.2: *Alignment of interface γ with the structure, which is positioned arbitrarily in the fluid mesh.*

with time step $\Delta t = t^{n+1} - t^n$. Coupling between the fluid and structure is achieved by enforcing the velocity constraint

$$\vec{v}_s - \vec{v}_f = \vec{0}, \tag{2.9}$$

along the fluid-structure interface γ.

Straightforward coupling of the fluid and structural domain requires that their boundaries and nodal points coincide along the interface, which implies equal order finite elements for both domains. Coincident boundaries with non-conforming discretizations can be realized by using Lagrange multipliers. The Lagrange multiplier $\vec{\lambda}$ weakly enforces the constraint (2.9) along the interface γ:

$$\int_\gamma \vec{\lambda} \cdot (\vec{v}_s - \vec{v}_f) d\gamma = 0. \tag{2.10}$$

The above equation is added to the total system of equations and implicitly introduces a surface force ($\vec{\lambda}$) exerted on the fluid and structure along γ to maintain the coupling between the two phases.

The approach used here is based on the fictitious domain method, described by Glowinski (Glowinski *et al.*, 1994). An essential feature of this method is that the fluid mesh is not altered or interrupted in any way by the presence of the immersed structure. The surface γ lies fictitious within the computational fluid domain and thus, does not necessarily have to be aligned with element boundaries of the fluid domain. It is convenient that it coincides with the boundary of the structural domain, although even this is not necessary. A typical example is given in Figure 2.2. Clearly, the interface γ intersects the fluid domain in an arbitrary way. In practice, the position of this boundary with respect to the fluid computational domain needs to be determined for every new deformed state of the structure to be able to define new coupling constraints. The method is described in detail by Baaijens (2001).

Temporal discretization of the Navier-Stokes equation (2.4) is achieved using an implicit backward-Euler scheme. Newton's method is used to linearize the non-linear convective term $\vec{v}_f \cdot \vec{\nabla}\vec{v}_f$. Spatial discretization is obtained using 202 Crouzeix-Raviart elements (Figure 2.3) based on a mixed velocity-pressure formulation with bi-quadratic interpolation for the velocity and a linear, discontinuous interpolation for the pressure.

For the structure spatial discretization is obtained using 8 quadratic beam elements with two displacements and one rotation as degrees of freedom. Beam elements, which are in fact line elements, are suitable for the analysis of slender structures where the

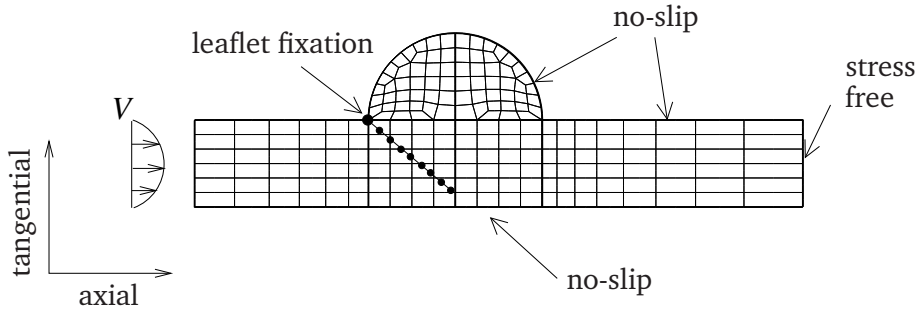

Figure 2.3: *Fluid and structure mesh. Boundary conditions are given for the fluid velocity at the inlet, outlet and walls and for the structural displacements and rotations at the leaflet fixation point.*

thickness is very small compared to the other dimensions. The bending stiffness of the structure, however, is incorporated in these elements.

The discretization of the Lagrange multiplier $\vec{\lambda}$ has been chosen linear, discontinuous and spatially coincident with element boundaries of the structural domain, i.e. along each element boundary of the structural domain that coincides with γ (which is always true for beam elements). The integral in Equation (2.10) along γ is computed using a Gaussian integration rule.

At the top and bottom wall of the channel no-slip boundary conditions are applied (Figure 2.3). The fluid outlet is assumed to be stress free and the inlet is fed with a pulsatile flow taken from corresponding experiments discussed further on. The leaflet is attached at the top wall just before the sinus cavity and the displacements and rotation at this fixation point are suppressed. The no-slip condition along the fluid-structure boundary is implicitly implemented by the coupling constraints of Equation (2.10).

The values of the geometric parameters, i.e. h, r, l, t_l, α, and material parameters, i.e. E, ν, η, ρ_f, are given in Table 2.1. The results will be shown for two different leaflet thicknesses to illustrate the influence on the flow phenomena.

The total system of equations is solved directly with an updated Lagrange procedure for large displacement analyses. Consequently, both the fluid and structure unknowns are solved simultaneously. The Newton-Raphson iteration method is used to obtain a converged solution. Additional coupling constraints defined by Equation (2.10) are added to the system at each Newton iteration using the most recently computed location of the boundary γ. This degrades the quadratic convergence rate of the Newton scheme, but has proven to give satisfactory results.

Geometrical parameters		Material parameters	
h, r [mm]	20	E [N/m^2]	$1.5{\cdot}10^6$
l [mm]	26	ν [$-$]	0.49
t_l [mm]	0.16; 0.3	η [kg/(m·s)]	$4.3{\cdot}\ 10^{-3}$
α [^{o}]	45	ρ_f [kg/m^3]	$1{\cdot}10^3$

Table 2.1: *Geometric and material parameters of the analyzed system.*

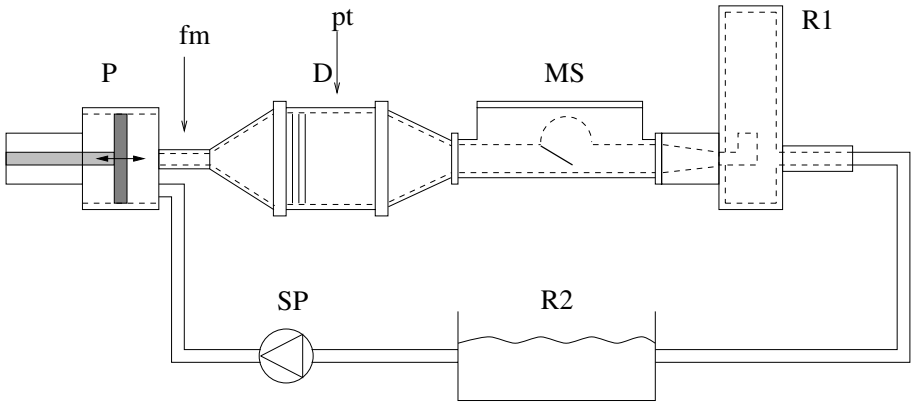

Figure 2.4: *Schematic drawing of the pulse duplicator. P: piston; D: diffuser; MS: measurement section; R1, R2: reservoirs; SP: steady pump; fm: flow meter; pt: pressure transducer.*

2.4 Validating experiments

The two-dimensional valve model is validated for the computed leaflet motion and altered fluid flow, since these quantities are a direct result of the fluid-structure interaction. To this end, a pulse duplicator is adopted to perform experiments in corresponding geometries, which are constructed from Plexiglas. Laser Doppler anemometry (LDA) is used to investigate the fluid velocity field and high speed video recordings to detect the leaflet positions. A schematic drawing of the experimental setup is given in Figure 2.4.

The setup is composed of rigid elements, i.e. a piston, a steady pump, a diffuser, a measurement section, and additionally, a resistance and reservoirs. The piston moves within a closed cylinder and is connected to a control card from which it receives a cosinusoidal signal with a frequency of 1 [Hz]. The steady pump is used to superpose a stationary flow on the pulsatile one such that only a forward flow results. The diffuser is composed of networks to break down the vortices induced by the piston motion, and to generate a fully developed laminar flow just before the entrance to the measurement section. The measurement section is shown in more detail in Figure 2.5. The inlet and outlet channels have a rectangular shaped cross section of height $h = 20$ [mm] and width $w = 120$ [mm]. The height/width ratio is such that approximately a two-dimensional situation is created, as will be shown below. The radius of the sinus is also taken conform the numerical model discussed before ($r = h$). The internal pressure in the system is increased using a closed reservoir (R1) at the outlet, resulting in a smoother motion of both fluid and leaflet. This reservoir is completely filled, such to prevent the introduction of additional compliance to the system. Hence, the pressure gradient inside the system is not affected by the reservoir.

A glycerol solution (36% glycerol solved in water) is used giving the fluid a density of $\rho_f = 1001$ [kg/m^3] and a viscosity of $\eta = 4.3 \cdot 10^{-3}$ [kg/m·s]. The solution approximates the density and viscosity of blood. The rubber sheet simulating the leaflet is made of EPDM rubber (ethylene-propylene-diene-monomer) having a density of 890 [kg/m^3] and a low swell-grade in the fluid. It is assumed to behave nearly incompressible, isotropic and linear elastic with a Young's modulus $E \approx 1.5$ [MPa]. Leaflets with a length $l = 26$ [mm] are analyzed for different thicknesses.

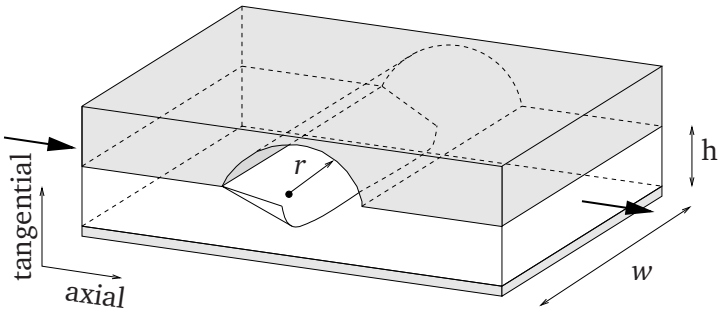

Figure 2.5: *Schematic drawing of the measurement section with leaflet.*

LDA equipment (Dantec type 60X11) is used to measure the fluid velocities two-dimensionally. The method is based on the dual beam backward-scattered principle (Goldstein, 1983) and is suitable to detect high speed flow velocities. PMMA particles (poly-methyl-met-acrylate) of 10 [μm] diameter were added to the solution as a seeding to scatter back the laser light generated by the LDA system. A high speed video camera (Kodak Ektapro HS 4540) is used to record the leaflet motion at a frequency of 100 frames per second with a spatial resolution of 256 $\times$ 256 pixels. The video images are digitized such that the leaflet profile is tracked to get an approximated position at a sufficient number of discrete points in time. The flow is measured with an electromagnetic flow probe (Skalar, type EC18-9044) with a capacity of 20 [l/min] for which a small amount of sodium chloride is added to the solution. The addition of PMMA and sodium chloride particles does not affect the fluid viscosity, which was measured with a Rheometrics RFS-II Couette viscosimeter. Finally, a pressure transducer (Gould, type P50) is used to measure the pressure. Specifications of the accuracy of the experimental techniques are given by Papa (1999).

2.5 Results

The first experiments are carried out to investigate the two-dimensional character of the system for two different thicknesses of the leaflet ($t_l = 0.16$ [mm] and 0.3 [mm]). Figure 2.6 shows the tangential and axial velocity components as a function of time and the position along the channel width measured at 30 [mm] upstream and 80 [mm] downstream the leaflet fixation point, respectively. For all cases, a two-dimensional flow field is observed of which the tangential velocity component is much smaller than the axial one. Three-dimensional effects occur at the channel walls, as expected, because of the no-slip conditions along these walls.

The velocity profiles measured at 50 [mm] before the leaflet fixation point are used as input for the numerical model. The LDA measurements are performed at half the width the channel where three-dimensional effects are supposed to balance because of the symmetry of the channel. The relevant experimental variables for the different cases are given in Table 2.2. The numerical parameters were already given in Table 2.1. The flow is characterized by the Reynolds number, $Re \approx 800$, and the Strouhal number, $Sr \approx 0.19$, which are approximately the same for all analyzed leaflets.

The computed leaflet positions are compared to the tracked leaflet motion obtained

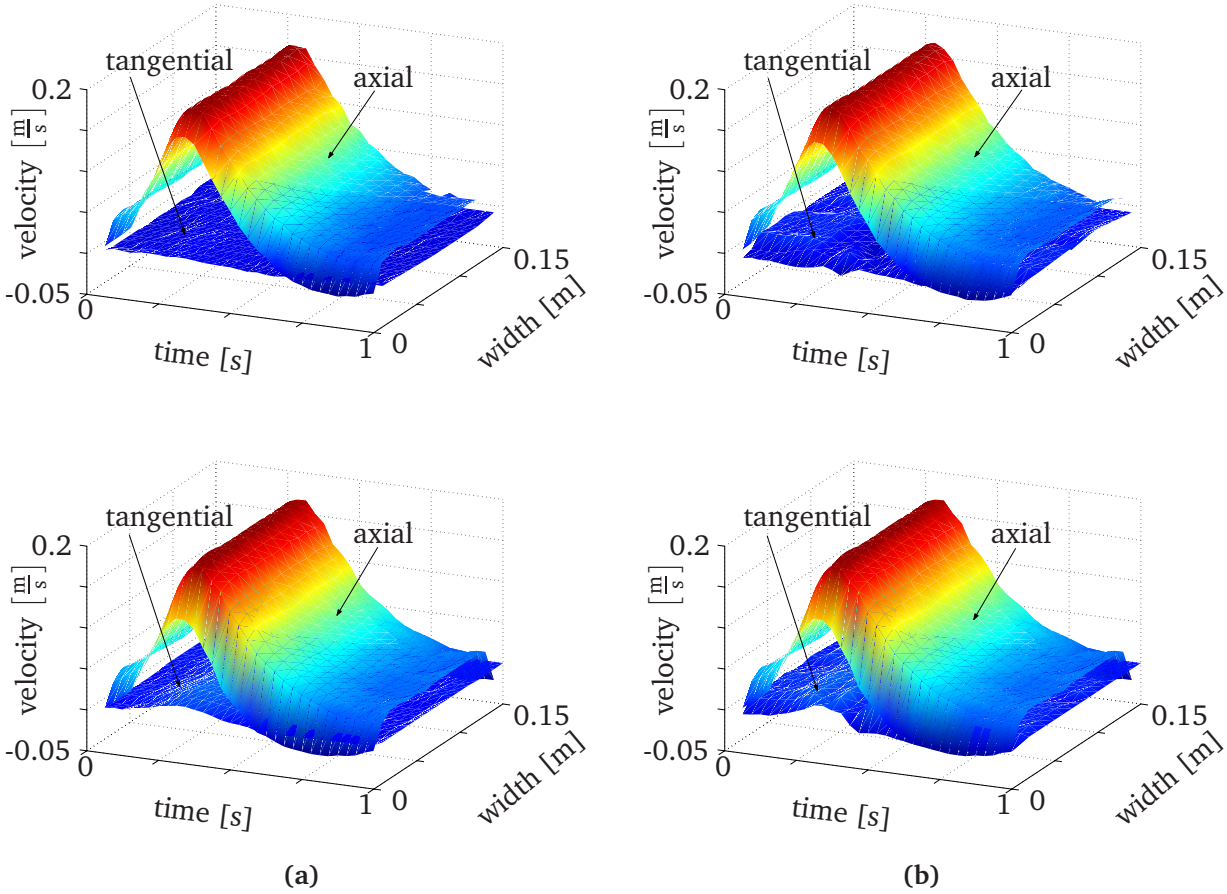

Figure 2.6: *Axial and tangential velocity components measured upstream (top) and downstream (bottom) the leaflet for $t_l = 0.16$ mm (a) and $t_l = 0.3$ mm (b).*

Leaflet number	1	2
t_l [mm]	0.16	0.3
l [mm]	26	26
w (leaflet) [mm]	117	117
stationary flow [l/min]	8.8	8.8
maximum flow [l/min]	22.46	23.44
minimum flow [l/min]	-0.78	1.16
σ of axial velocity [m/s]	$2.6{\cdot}10^{-3}$	$2.5{\cdot}10^{-3}$
σ of tang. velocity [m/s]	$0.89{\cdot}10^{-3}$	$1.2{\cdot}10^{-3}$
peak pressure [kPa]	42	42
Re [–]	795	813
Sr [–]	0.192	0.184

Table 2.2: *Relevant experimental variables*

with the digitized high speed recordings. The results of the thin leaflet ($t_l = 0.16$ [mm]) are shown in Figure 2.7(a). The experimentally observed motion of this leaflet is not perfectly two-dimensional. Instead, it slightly bends in the third dimension at the side edges because of its high flexibility, as illustrated in Figure 2.5. This is due to the fact that the fluid passes through the narrow space between the leaflet edges and the channel wall, which prevents the leaflet from slipping along the side walls. For this reason the upper and lower leaflet profiles have been tracked and are represented with the dashed lines in Figure 2.7(a).

The solid line represents the computed position of the leaflet at the same instant in time. The associated measured flow pulse is also shown to give the corresponding time points in the cycle. The motion of the thicker leaflet is more two-dimensional because of its larger thickness resulting in a higher bending stiffness. The results of this leaflet are shown in Figure 2.7(b) for identical points in time as used for the thin leaflet. Although

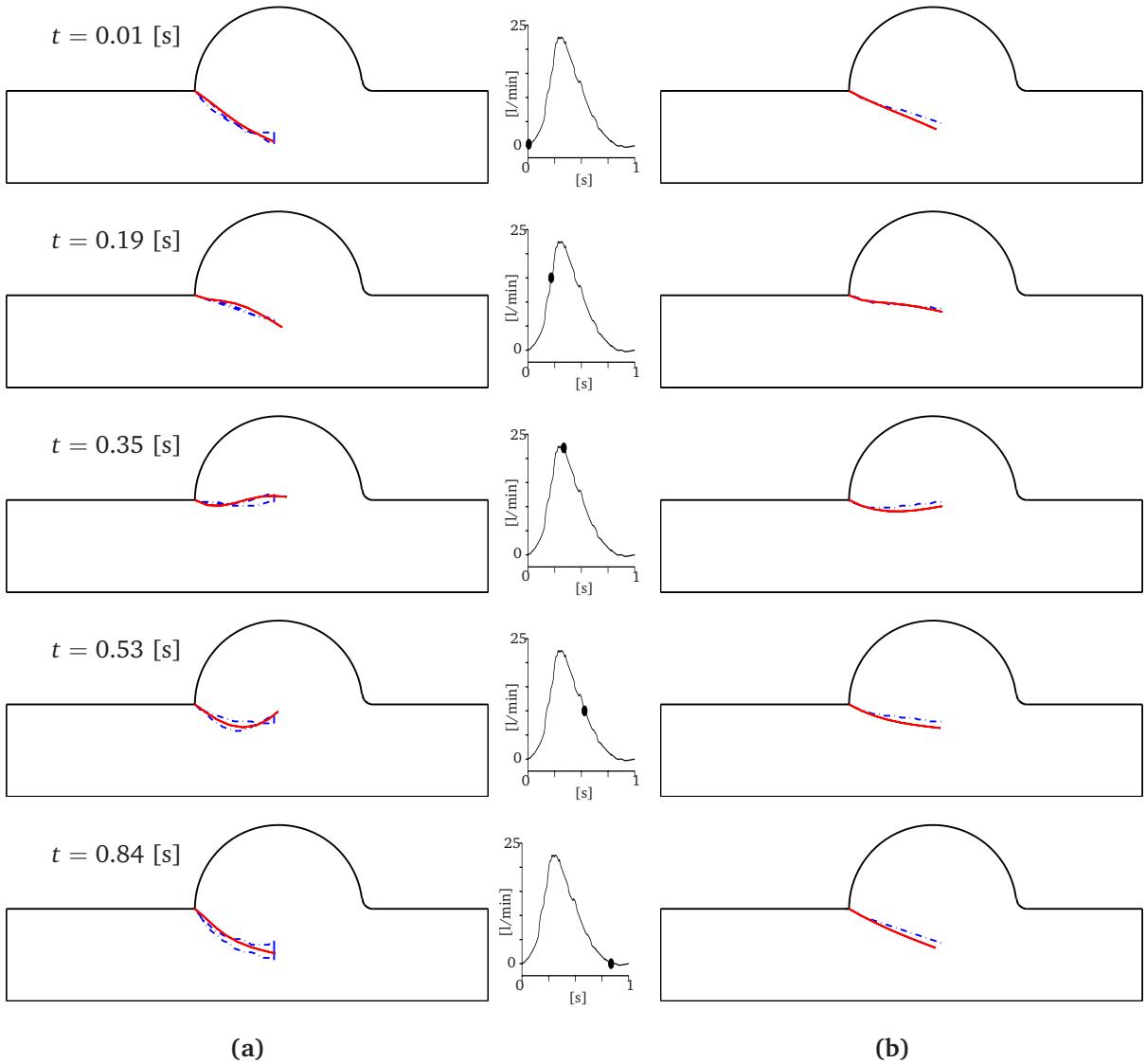

Figure 2.7: *Numerical (solid) and experimental (dashed) leaflet positions at successive time points for $t_l = 0.16$ [mm] (a) and t_l =0.3 [mm] (b). The flow pulse is given in the middle.*

maximum and minimum flow slightly differ between both leaflets (Table 2.2), the pulse shape shown in this figure can be used in both cases. These figures demonstrate that the numerical leaflet position lags behind the experimental leaflet position. Probable cause is the difference in fluid and leaflet density, which results in a buoyancy force acting on the leaflet. As mentioned before this force has not been taken into account in the numerical model. This phenomenon is negligible for the highly flexible leaflet, since this leaflet easily follows the fluid flow.

The axial velocity profiles at different cross sections along the center of the channel are analyzed for different points in time. Figure 2.8(a) shows the situation for the thin leaflet and Figure 2.8(b) for the thicker leaflet. Again, the dashed lines represent the measured profiles, whereas the solid lines are the computed profiles. Scattering and moving particles are required for LDA measurements to produce data. Obviously, at the position of the leaflet in the channel no such particles are present. Moreover, the light path of the laser is blocked by the semi-transparent leaflet. For the thinner leaflet,

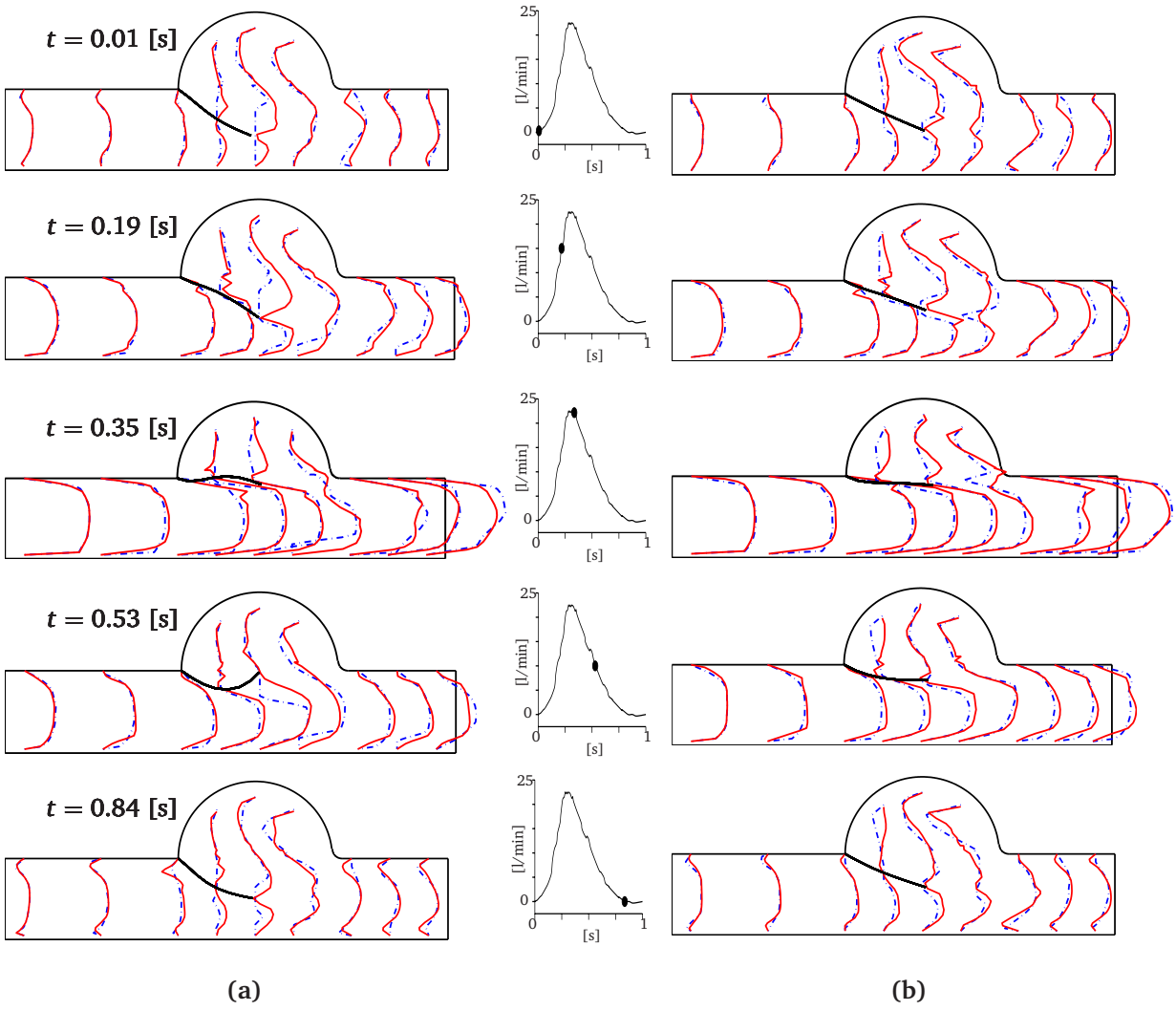

Figure 2.8: *Numerical (solid) and experimental (dashed) axial velocity profiles at successive time points for t_l = 0.16 [mm] (a) and t_l =0.3 [mm] (b). The flow pulse is given in the middle.*

which bends at the channel walls in the direction of its width, this results in a large area of non-detectable fluid velocities. These areas are shown in Figure 2.8(a) as straight, vertical (zero velocity) line-segments of the profiles close to the tip of the leaflet. For the thicker leaflet, these areas are much smaller, as can be seen in Figure 2.8(b). In this figure a difference in fluid velocity is observed near the left sinus wall. A small vortex is present in the simulations near the leaflet fixation point (solid line). This vortex could not be detected in the LDA experiments with the applied settings.

Finally, vector plots associated with the thin leaflet are given in Figure 2.9 for a global assessment of the flow phenomena. The leaflet positions are included in these figures. Although the grid density of the numerical model is much higher, velocity vectors are given only for a selective number of points such that the numerical grid corresponds better to the experimental grid which is used for the LDA measurements. As the flow starts to decelerate, pressure at the leaflet tip exceeds the pressure in the sinus cavity, resulting in a vortex which develops at the leaflet tip moving towards the center of the sinus. Next, the leaflet starts a downward motion at a still forward flow. When the fluid has reached a minimum flow and the leaflet is in its lowest position a second vortex develops at the bottom wall downstream of the leaflet followed by a weaker vortex at the top wall downstream of the sinus. These vortices vanish when the flow accelerates again at the beginning of a new cycle and the procedure repeats. The flow phenomena observed here are typical for an instationary viscous flow in such a geometry with a flexible leaflet (Van Steenhoven, 1979) and are present for both leaflets.

Discussion on detailed observations for these two-dimensional analyses and on the results considering the comparison between both cases of different leaflets is beyond the scope of this chapter. Instead, validation of the numerical methods, applied to a representative problem, is discussed and the most important observations are given in the next section.

2.6 Discussion

A two-dimensional fluid-structure interaction model of the aortic valve is developed, which is based on the finite element method. The fictitious domain technique is used to couple the fluid and the structure phases. The features of the presented approach are: 1. the fluid computation is done on a fixed, Eulerian grid, and the structure computation is done on a Lagrangian grid, 2. both grids are independent of each other, 3. coupling of the fluid and structure is done by additional velocity constraints using Lagrange multipliers, 4. The fluid and structure unknowns are solved simultaneously.

Features 1 and 2 are particularly interesting when analyzing geometries that are complicated because of immersed complex bodies. The independence of the fluid and structure mesh allows the use of well-established computational software developed for fluid and structural problems. Feature 3 has proven to be suitable to couple the two phases. Alternatively, a penalty function or an augmented Lagrange multiplier method can be used. However, these methods affect the matrix condition, such that numerical problems may arise. The system is solved in a direct, fully coupled manner which implies that both fluid and structure unknowns are solved simultaneously (feature 4). Although the condition of the system matrix is degenerated because fluid and structure

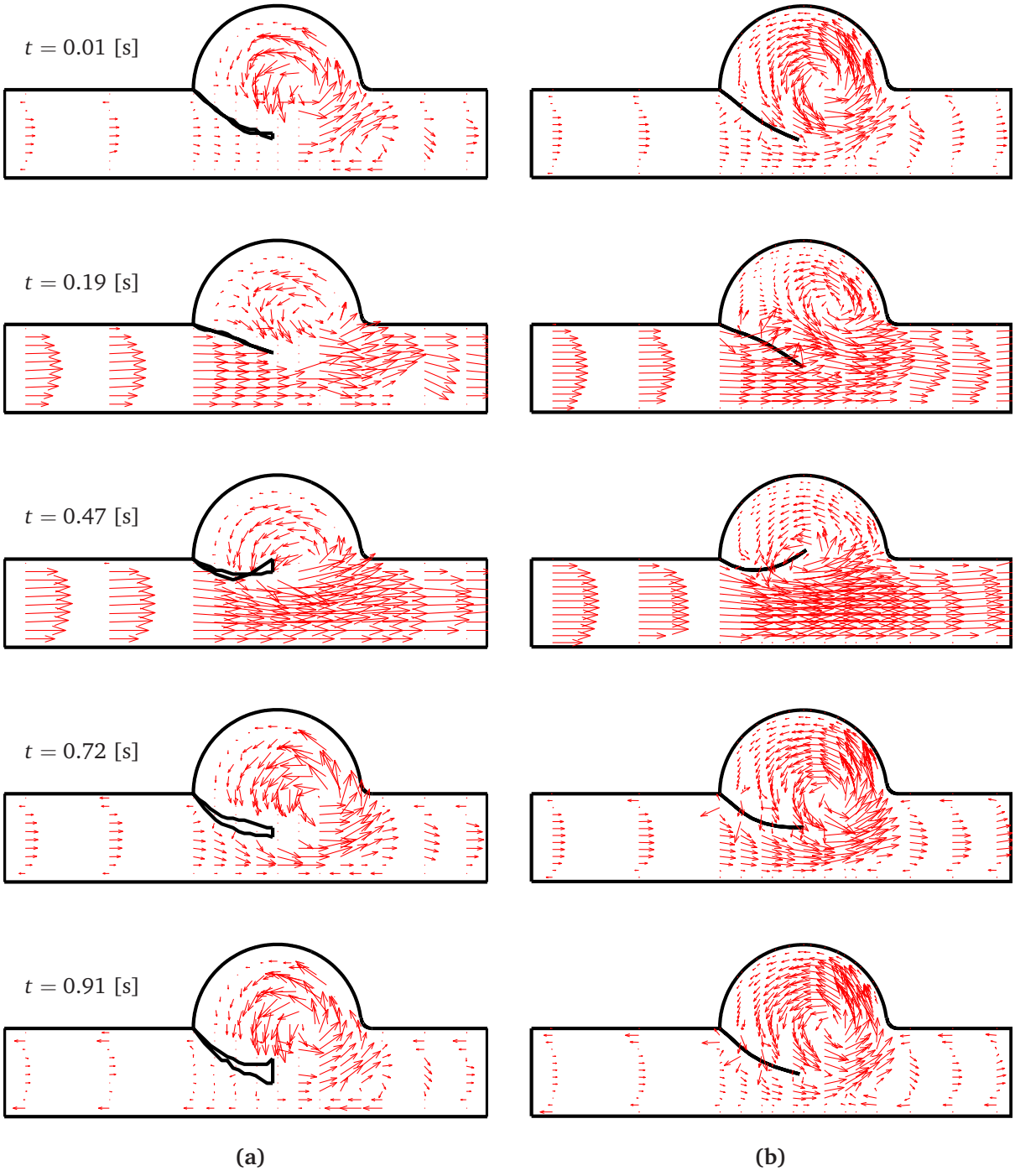

Figure 2.9: *Velocity vector plots of experimental (a) and computational (b) data for leaflet thickness $t_l = 0.16$ [mm].*

entries differ several orders of magnitude and additional Lagrange multipliers alter the matrix structure, no numerical problems occurred for solving the two-dimensional case.

A staggered approach can be used to solve the system uncoupled, (Farhat *et al.*, 1998). One way to do this is to solve the structural problem, extracting the structural velocities and apply those to the fluid system. Next, advance the fluid system and en-

force the fluid pressure to the structure. Numerical tests, however, have shown that in the case of conditions typical for flow through the heart valve, instability problems occur, which are instigated by the high flexibility of the structure (Appendix D). Peskin's approach (see the introduction) appears to be more suitable in solving the system uncoupled.

The model has been validated with experiments on corresponding geometries using LDA measurements and digitized high speed video recordings. Both the leaflet motion and the altered fluid flow are used for comparison, since these quantities are a direct result of the fluid-leaflet interaction. Leaflet motion is predicted within the experimental error. Most of the details of the complicated transient flow, such as the moving vortex in the sinus cavity, the vortices downstream the leaflet and the magnitudes of the velocities, are reproduced numerically. From the results it is concluded that the fictitious domain method can be used to describe the fluid-leaflet interaction. The presence of buoyancy forces, acting on the structure, probably results in a discrepancy between the computed and measured leaflet position, during the diastolic phase. Tests have shown that the effect of this force vanishes with decreasing bending stiffness of the leaflet. A difference in velocity profiles is observed near the sinus wall close to the leaflet fixation point. The numerical model predicts a small secondary vortex near the leaflet fixation point, preventing the large vortex to fully develop over the complete sinus area. This secondary vortex has not been observed in the experiments. LDA experiments focused on this area should reveal that this is an inaccuracy of the measurement rather than an incorrectness in the computed velocity field.

The applied methods are described for the two-dimensional case. The natural aortic valve consists of three flexible leaflets of thickness in the order of 0.2 [mm], which come in contact with each other during the closing phase, and three sinus cavities, which are constituted within the compliant aortic root (Thubrikar, 1990). Moreover, the flow conditions used here result in a Reynolds number $Re \approx 800$ and a Strouhal number $Sr \approx 0.19$, which are different from the physiological numbers, i.e. 4500 and 0.06, respectively. The two-dimensional representation described in this chapter is therefore not realistic to analyze the physiological situation. However, the model is used to test the applied methods for predicting the interacting behaviour of such systems as a first step towards full three-dimensional numerical models of fluid-structure interaction in heart valves. The presented theory will be extended to three-dimensional cases by taking also into account the third dimension in Equations (2.1) to (2.10). However, such analyses require much more memory and CPU-time. Furthermore, contact between two adjacent leaflets and compliance of the aorta applied to three-dimensional test models need to be considered. These extensions will be elaborated in the next chapters.

References

Baaijens, F.P.T., 2001. A fictitious domain/mortar element method for fluid-structure interaction. *International Journal for Numerical Methods in Fluids*, **35**(7): 743-761.

Bertrand, F., Tanguy, P.A., Thibault, F., 1997. A three-dimensional fictitious domain method for incompressible fluid flow problems. *International Journal for Numerical Methods in Fluids*, **25**(6): 719-736.

Cacciola, G., De Hart, J., Peters, G.W.M., Schreurs, P.J.G., Baaijens, F.P.T., 1998. A synthetic fibre-reinforced heart valve. *In Proceedings 716 of European Conference on Composite Materials.* Woodhead Publishing Limited, Cambridge, UK.

De Hart, J., Cacciola, G., Schreurs, P.J.G., Peters, G.W.M., 1998. A three-dimensional analysis of a fibre-reinforced aortic valve prosthesis. *Journal of Biomechanics*, **31**(7): 629-638.

Farhat, C., Lesoinne, M., LeTallec, P., 1998. Load and motion transfer algorithms for fluid/structure interaction problems with non-matching discrete interfaces: momentum and energy conservation, optimal discretization and application to aeroelastics. *Computer Methods in Applied Mechanics and Engineering*, **157**: 95-114.

Glowinski, R., Pan, T.-W., Periaux, J., 1994. A fictitious domain method for Dirichlet problem and applications. *Computer Methods in Applied Mechanics and Engineering*, **111**: 283-303.

Horsten, J.B.A.M., 1990. *On the analysis of moving heart valves: a numerical fluid-structure interaction model.* Ph.D. thesis, Eindhoven University of Technology, Eindhoven.

Papa, V., 1999. *Fluid-Structure Interaction of a Flexible Leaflet in a Pulsatile Flow.* Master's thesis WFW 99.037, Eindhoven University of Technology, Eindhoven.

Peskin, C.S., McQueen, D.M., 1994. Mechanical equilibrium determines the fractal fiber architecture of the aortic heart valve leaflets. *American Journal of Physiology*, **35**: 319-328.

Thubrikar, M., 1990. *The Aortic Valve*. CRC Press, Boca Raton, Florida.

Van Steenhoven, A.A., van Dongen, M.E.H., 1979. Model studies of the closing behaviour of the aortic valve. *Journal of Fluid Mechanics*, **90**(1): 21-32.

Chapter 3

Three-Dimensional Analysis of Fluid-Structure Interaction in the Aortic Heart Valve[1]

Numerical analysis of the aortic valve has mainly been focused on the closing behaviour during the diastolic phase rather than the kinematic opening and closing behaviour during the systolic phase of the cardiac cycle. Moreover, the fluid-structure interaction in the aortic valve system is most frequently ignored in numerical modeling. The effect of this interaction on the valve's behaviour during systolic functioning is investigated. The large differences in material properties of fluid and structure and the finite motion of the leaflets complicate blood-valve interaction modeling. This has impeded numerical analyses of valves operating under physiological conditions. A numerical method, known as the Lagrange multiplier based fictitious domain method, is used to describe the large leaflet motion within the computational fluid domain. This method is applied to a three-dimensional finite element model of a stented aortic valve. The model provides both the mechanical behaviour of the valve and the blood flow through it. Results show that during systole the leaflets of the stented valve appear to be moving with the fluid in an essentially kinematical process governed by the fluid motion.

[1]The contents of this chapter are submitted to the *Journal of Biomechanics*, under the title:

A three-dimensional computational analysis of fluid-structure interaction in the aortic heart valve
De Hart, J., Peters, G.W.M., Schreurs, P.J.G., Baaijens, F.P.T.

3.1 Introduction

Many numerical structural models have been developed that describe the behaviour of the aortic valve ignoring its interaction with the blood, e.g. see Black *et al.* (1991); Chandran *et al.* (1991); Krucinski *et al.* (1993); De Hart *et al.* (1998); Cacciola (2000). The opening and closing behaviour of this valve during systole involves, however, a strong interaction between blood and the surrounding tissue. Several attempts have been made to analyze the valve kinematics using numerical fluid-structure interaction models. Horsten (1990) modeled the interaction of a two-dimensional leaflet with a rigid channel flow. Peskin and McQueen (1995) developed a three-dimensional model including the surrounding vessel walls. However, these models used simplified descriptions for the structures and were only applicable for relatively low, non-physiological Reynolds numbers. Fluid-structure simulation of bioprosthetic aortic valve functioning is performed by Makhijani *et al.* (1997), where the leaflet structure has a much higher resistance to bending compared to the natural leaflets. A physiological realistic fluid-structure interaction model of the natural valve, accounting for the phenomena occurring during systolic phase, has not been developed to date.

Modeling of such a fluid-structure interaction system is complicated due to the large motion of the thin leaflets through the computational fluid domain. The mathematical formulation of the equation of motion for a fluid is most conveniently described with respect to an Eulerian reference frame. However, this is incompatible with the Lagrangian formulation which is more appropriate to describe a structural phase. The arbitrary Lagrangian-Eulerian (ALE) method, first proposed by Donea *et al.* (1982), effectively combines the two different formulations and is frequently used in fluid-structure interaction analyses. Applied to the fluid phase, the ALE method requires a continuous adaptation of the fluid mesh without modification of the topology.

In heart valves, it is difficult to adapt the fluid mesh in such a way that a proper mesh quality is maintained without changing the topology, see Baaijens (2001). Alternatively, remeshing of the fluid domain may be performed in conjunction with an ALE method, where remeshing is only performed if the mesh has degenerated too much. The change in topology during remeshing requires the use of interpolation techniques to recover state variables on the newly generated mesh. This not only introduces artificial diffusivity, but it is also difficult and/or time-consuming to perform with sufficient robustness and accuracy for three-dimensional problems. This method is therefore not adopted in this work.

To resolve the limitations of these mesh update strategies we use a fictitious domain method to describe the interaction of the valve leaflets with the surrounding fluid. In this method, the different mathematical descriptions of the equations of motion of the fluid and structure can be maintained, allowing convenient classical formulations for each of these subsystems. Moreover, the fluid mesh is not altered or interrupted by the presence of the immersed domain, and therefore preserves its original quality. Fictitious domain related methods were first applied by Hyman (1952) among others. Later Saul'ev (1963) introduced the term "fictitious domain". To date many applications of fictitious domain related techniques have been reported, e.g. see Perng *et al.* (1993); Rai (1985); Glowinski *et al.* (1994); Sheehy *et al.* (1994). Within the same concept, Peskin (1977) devised the immersed interface method, to carry out simulations of blood

flow in the heart. In this method a fixed mesh is used and the moving bodies (the muscular heart walls and valve leaflets) are approximated by a series of control points at which tension forces are not known *a priori*. A variant to this technique, known as the immersed interface method, was presented by LeVeque and Li (1997).

More recently a new class of fictitious domain methods has been developed, which is based on the explicit use of Lagrange multipliers for the treatment of the internal parts of the geometry (Glowinski *et al.*, 1998). These parts, which may be moving, are not meshed as such. Instead, they are taken into account by means of a set of pointwise kinematical constraints that are coupled with the equations of motion using a Lagrangian method. Although similar to Peskin and McQueens's approach in as much as it is based upon control points for the characterization of the internal parts, this type of fictitious domain method does not resort to empirical forces. Velocity constraints are imposed on the control points through Lagrange multipliers so that only kinematics of the internal part must be known *a priori*, see Sheehy *et al.* (1994); Glowinski *et al.* (1998). A similar approach described in Bertrand *et al.* (1997) is the basis for the method adopted in this work. It is extended for finite element applications where the motion of a deformable internal part is not known *a priori* but depends on the surrounding fluid flow. Experimental validation of this method applied to a two-dimensional aortic valve is demonstrated in Chapter 2 and by De Hart *et al.* (2000). The application to a three-dimensional model is described in this chapter. This model is used to study the effect of fluid-structure interaction on the valve behaviour.

First, the problem definition and governing equations are given for the fluid and structure computations. Next, the coupling between these two phases is described and a fictitious domain formulation is derived. The discretization of each of the subproblems is discussed followed by a description of the solution procedure. Finally, the application to the aortic valve is analyzed and the presented results are discussed.

3.2 Problem definition and governing equations

The objective is to analyze the three-dimensional fluid-structure interaction in the aortic valve, as sketched two-dimensionally in Figure 3.1. The analysis is confined to a stented aortic valve of which the geometrical properties, material properties and boundary conditions are given in the application section. The mathematical formulations describing the fluid and structure are presented first.

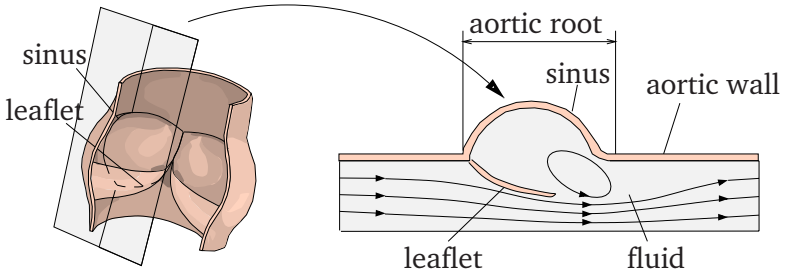

Figure 3.1: *Two-dimensional sketch of the aortic valve.*

3.2.1 Fluid domain

The blood flow is considered to be isothermal and incompressible. The equation of motion and continuity equation within the fluid domain Ω_f bounded by $\Gamma_f = \Gamma_f^v \cup \Gamma_f^t$ are, in absence of body forces

$$\rho_f(\frac{\partial \vec{v}_f}{\partial t} + \vec{v}_f \cdot \vec{\nabla}\vec{v}_f) = \vec{\nabla} \cdot \boldsymbol{\sigma}_f \qquad \text{in} \quad \Omega_f, \tag{3.1}$$

$$\vec{\nabla} \cdot \vec{v}_f = 0 \qquad \text{in} \quad \Omega_f, \tag{3.2}$$

where ρ_f denotes the density, t the time, $\vec{v}_f$ is the velocity, $\boldsymbol{\sigma}_f$ the Cauchy stress tensor and $\vec{\nabla}$ the gradient operator with respect to the current configuration. The Dirichlet and Neumann boundary conditions at Γ_f^v and Γ_f^t, respectively, read for this set:

$$\vec{v}_f = \vec{v}_f^p \qquad \text{on} \quad \Gamma_f^v, \tag{3.3}$$

$$\boldsymbol{\sigma}_f \cdot \vec{n} = \vec{t}_f^{\,p} \qquad \text{on} \quad \Gamma_f^t, \tag{3.4}$$

where $\vec{n}$ denotes the outward normal of Γ_f^t and $\vec{v}_f^p$, $\vec{t}_f^{\,p}$ denote the prescribed velocity and surface traction. The constitutive behaviour of the blood is assumed to be Newtonian (Caro *et al.*, 1978), hence

$$\boldsymbol{\sigma}_f = -p_f \boldsymbol{I} + 2\eta \boldsymbol{D}_f, \tag{3.5}$$

with p_f the pressure, $\boldsymbol{I}$ the second-order unit tensor, η the dynamic viscosity of the fluid and $\boldsymbol{D}_f$ the rate-of-deformation tensor defined as $\boldsymbol{D}_f = \frac{1}{2}(\vec{\nabla}\vec{v}_f + (\vec{\nabla}\vec{v}_f)^T)$. Substituting this constitutive relation into Equation (3.1) yields the well-known Navier-Stokes equation:

$$\rho_f(\frac{\partial \vec{v}_f}{\partial t} + \vec{v}_f \cdot \vec{\nabla}\vec{v}_f) = -\vec{\nabla} p_f + \vec{\nabla} \cdot 2\eta \boldsymbol{D}_f \qquad \text{in} \quad \Omega_f. \tag{3.6}$$

Within the framework of the finite element method (FEM) the weak form of the Navier-Stokes and continuity equation can be written as:

$$\int_{\Omega_f} \left(\vec{w}_f \cdot (\rho_f \frac{\partial \vec{v}_f}{\partial t} + \rho_f \vec{v}_f \cdot \vec{\nabla}\vec{v}_f) + (\vec{\nabla}\vec{w}_f)^T : 2\eta \boldsymbol{D}_f \right) d\Omega_f - \int_{\Omega_f} (\vec{\nabla} \cdot \vec{w}_f)\, p_f \, d\Omega_f = \int_{\Gamma_f} \vec{w}_f \cdot \vec{t}_f \, d\Gamma_f, \tag{3.7}$$

$$\int_{\Omega_f} q_f \, (\vec{\nabla} \cdot \vec{v}_f) \, d\Omega_f = 0,$$

which must hold for all admissible weighting functions $\vec{w}_f$ and q_f.

3.2.2 Structural domain

In absence of body forces and with inertia terms neglected, the equation of motion and the continuity equation for the incompressible structural domain Ω_s, i.e. the leaflets, bounded by $\Gamma_s = \Gamma_s^u \cup \Gamma_s^t$ read:

$$\vec{\nabla} \cdot \boldsymbol{\sigma}_s = \vec{0} \qquad \text{in} \quad \Omega_s, \tag{3.8}$$

$$\det(\boldsymbol{F}) = 1 \qquad \text{in} \quad \Omega_s, \tag{3.9}$$

where $\boldsymbol{\sigma}_s$ is the Cauchy stress tensor. The deformation tensor is defined as $\boldsymbol{F} = (\vec{\nabla}_0 \vec{x}_s)^T$, with $\vec{\nabla}_0$ the gradient operator with respect to the initial configuration and $\vec{x}_s$ the field of structural material points. This set of equations is completed with suitable Dirichlet conditions similar to Equation (3.3).

The aortic valve leaflets are assumed to behave linear elastic and isotropic according to a Neo-Hookean constitutive law:

$$\boldsymbol{\sigma}_s = -p_s \boldsymbol{I} + \boldsymbol{\tau}_s \quad ; \qquad \boldsymbol{\tau}_s = G(\boldsymbol{B} - \boldsymbol{I}), \tag{3.10}$$

where p_s denotes the hydrostatic pressure, and $\boldsymbol{\tau}_s$ the extra stress tensor. The definition of $\boldsymbol{\tau}_s$ represents an isotropic hyperelastic behaviour with G the shear modulus and $\boldsymbol{B}$ the Finger or left Cauchy-Green strain tensor, defined as $\boldsymbol{B} = \boldsymbol{F} \cdot \boldsymbol{F}^T$.

For the structural domain an updated Lagrange formulation is used to describe the deformation throughout the analysis. Let $\boldsymbol{F}^n$ denote the deformation tensor from the initial configuration to the configuration at $t = t^n$ and $\boldsymbol{F}^\Delta$ the deformation tensor from $t = t^n$ to $t = t^{n+1}$, then the tensor defining the deformation from the initial state to the current state ($t = t^{n+1}$) is

$$\boldsymbol{F}^{n+1} = \boldsymbol{F}^\Delta \cdot \boldsymbol{F}^n. \tag{3.11}$$

The extra stress tensor at the current time t can now be written as

$$\boldsymbol{\tau}_s = \boldsymbol{F}^\Delta \cdot \boldsymbol{\tau}_s^n \cdot (\boldsymbol{F}^\Delta)^T + G(\boldsymbol{F}^\Delta \cdot (\boldsymbol{F}^\Delta)^T - \boldsymbol{I}), \tag{3.12}$$

where $\boldsymbol{\tau}_s^n$ refers to the extra stress at time $t = t^n$. Hence, the weak form of the structural problem, assuming absence of externally applied surfaces loads, yields:

$$\begin{aligned} &\int_{\Omega_s} (\vec{\nabla}\vec{w}_s)^T : \left(\boldsymbol{F}^\Delta \cdot \boldsymbol{\tau}_s^n \cdot (\boldsymbol{F}^\Delta)^T + G(\boldsymbol{F}^\Delta \cdot (\boldsymbol{F}^\Delta)^T - \boldsymbol{I}) \right) d\Omega_s - \\ &\qquad\qquad \int_{\Omega_s} (\vec{\nabla} \cdot \vec{w}_s)\, p_s d\Omega_s = 0, \\ &\int_{\Omega_s} q_s \left(\det(\boldsymbol{F}^\Delta) - 1 \right) d\Omega_s = 0, \end{aligned} \tag{3.13}$$

which must hold for all admissible weighting functions $\vec{w}_s$ and q_s.

In the Lagrange formulation it is customary to take the displacement field $\vec{u}_s$ as the unknown. During a time interval $t^n \to t^{n+1}$ this field is defined as

$$\vec{u}_s = \vec{x}_s^{n+1} - \vec{x}_s^n, \tag{3.14}$$

where $\vec{x}_s^n$ and $\vec{x}_s^{n+1}$ denote the position of a material point at time $t = t^n$ and $t = t^{n+1}$ respectively. In view of the fluid-structure interaction the structural velocity field is considered rather than the displacement field. Hence, the velocity during time step $\Delta t = t^{n+1} - t^n$ is defined as

$$\vec{v}_s = \frac{1}{\Delta t}(\vec{x}_s^{n+1} - \vec{x}_s^n) = \frac{\vec{u}_s}{\Delta t}, \tag{3.15}$$

which represents a first-order approximation for the structural velocity field.

3.3 Fluid-structure interaction

In this analysis the fluid-structure interaction is considered between the fluid domain (blood) and the immersed structures, i.e. the valve leaflets, while assuming the aortic root to be rigid (Figure 3.1). The fluid-structure coupling is straightforward if equal-order discretization of the fluid and structural domain is used and nodes and element boundaries coincide along the fluid-structure interface. To allow independence between the fluid and structural discretizations a fictitious domain method is adopted here.

Consider the domain Ω_s^i, with fluid-structure interface boundary γ, to be the part of Ω_s immersed in Ω_f, see Figure 3.2. Then fluid-structure coupling is realized by enforcing the (no-slip) constraint

$$\vec{v}_f - \vec{v}_s = \vec{0} \qquad \text{on} \quad \gamma. \tag{3.16}$$

Physically Ω_f and Ω_s^i cannot occupy the same domain in space; interaction occurs only at the interface γ. Thus, a new definition for the fluid domain would hold: $\Omega_f^* = \Omega_f \backslash \Omega_s^i$. In fluid-structure interaction analyses the set of (3.7) and (3.13) and the no-slip constraint (3.16) are most commonly adopted with the fluid domain defined as $\Omega_f \backslash \Omega_s^i$ using for example an ALE technique. The basic idea of the fictitious domain method is to extend the fluid problem defined in $\Omega_f \backslash \Omega_s^i$ to a problem defined in all of Ω_f, while still forcing the solution to satisfy (3.16). However, the fluid contents enclosed by Ω_s^i may not affect the structural deformation, since it is physically not present. On the other hand, the enclosed fluid contents must move according to the inner structural deformation, to preserve conservation of fluid mass. For thin-walled structures, such as the heart valve leaflets, the complications arising from enclosing a part of the fluid domain may be neglected, since the inner fluid volume is much smaller than the outside volume. Moreover, assuming the thickness to be negligible as far as the interaction with the fluid is considered, alignment of the interface γ with one side of the leaflet is particularly suitable. Hence, in a fictitious domain formulation of the aortic valve leaflets the definition Ω_f for the entire fluid domain, including the immersed structures, can be maintained.

The constraint Equation (3.16) must be incorporated into the weak formulations of the fluid and structural problem (formulation (3.7) and (3.13) respectively). To this end one of three approaches is commonly pursued: a Lagrange multiplier method, a penalty method or an augmented Lagrange method (Fortin *et al.*, 1983; Bathe, 1982).

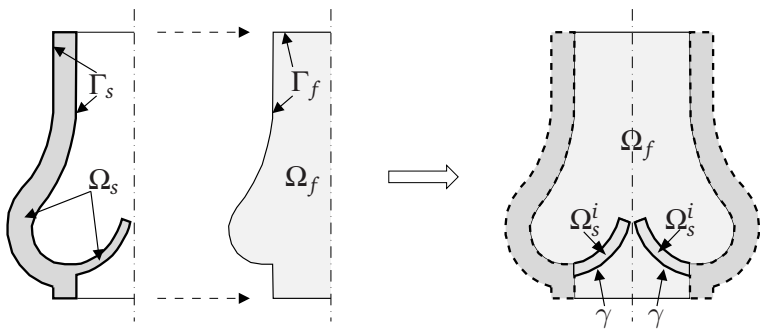

Figure 3.2: *Sample of an immersed domain Ω_s^i with boundary γ in Ω_f.*

Here the Lagrange multiplier method is adopted to avoid the introduction of the penalty parameter, which affects the matrix condition due to its large value. In this method the Lagrange multiplier $\vec{\lambda}$ is used to weakly enforce the coupling constraint on the fluid-structure interface γ. The resulting set of equations is given by

$$\int_{\Omega_f} \vec{w}_f \cdot (\rho_f \frac{\partial \vec{v}_f}{\partial t} + \rho_f \vec{v}_f \cdot \vec{\nabla}\vec{v}_f)\, d\Omega_f + \int_{\Omega_f} (\vec{\nabla}\vec{w}_f)^T : 2\eta \boldsymbol{D}_f \, d\Omega_f - \int_{\Omega_f} (\vec{\nabla} \cdot \vec{w}_f) p_f \, d\Omega_f + \int_{\gamma} \vec{w}_f \cdot \vec{\lambda} \, d\gamma = \int_{\Gamma_f} \vec{w}_f \cdot \vec{t}_f \, d\Gamma_f, \tag{3.17}$$

$$\int_{\Omega_f} q_f (\vec{\nabla} \cdot \vec{v}_f)\, d\Omega_f = 0,$$

$$\int_{\Omega_s} (\vec{\nabla}\vec{w}_s)^T : \left(\boldsymbol{F}^{\Delta} \cdot \boldsymbol{\tau}_s^n \cdot (\boldsymbol{F}^{\Delta})^T + G(\boldsymbol{F}^{\Delta} \cdot (\boldsymbol{F}^{\Delta})^T - \boldsymbol{I}) \right) d\Omega_s - \int_{\Omega_s} (\vec{\nabla} \cdot \vec{w}_s) p_s \, d\Omega_s - \int_{\gamma} \vec{w}_s \cdot \vec{\lambda} \, d\gamma = 0, \tag{3.18}$$

$$\int_{\Omega_s} q_s (\det(\boldsymbol{F}^{\Delta}) - 1)\, d\Omega_s = 0,$$

$$\int_{\gamma} \vec{\ell} \cdot (\vec{v}_f - \vec{v}_s)\, d\gamma = 0, \tag{3.19}$$

where $\vec{\ell}$ denotes the weighting function associated with Equation (3.19). In this formulation $\vec{\lambda}$ may be interpreted as the surface force exerted on the fluid and structure along γ to maintain the coupling between them.

The appearance of the Lagrange multiplier in (3.17) to (3.19) frequently has been based on invoking stationarity of the system energy functional to which Equation (3.16) is imposed using Lagrange multipliers, e.g. see Baaijens (2001); Bertrand *et al.* (1997); Glowinski *et al.* (1998) and Appendix B. A sufficient condition for the existence of an equivalent energy functional of partial differential equations is that the differential operators must be linear. However, the application of Lagrange multipliers is most commonly generalized to hold for non-linear problems to which the classical Galerkin finite element method is applied (Cuvelier *et al.*, 1986; Bathe, 1982).

3.4 Discretization

The spatial discretizations of the fluid domain Ω_f and structural domain Ω_s are denoted by $\mathcal{T}_f$ and $\mathcal{T}_s$, respectively, and are based on triquadratic hexahedral elements. It is well established that the mixed velocity/pressure and displacement/pressure formulations defined above need to satisfy the so-called inf-sup stability condition (Bathe (1982); Hughes (1987) and references therein). A variety of discretization schemes is available that satisfy this condition. Here the Crouzeix-Raviart family has been chosen, where the velocity/displacement field is approximated by a full triquadratic approximation and the pressure is approximated linearly and is discontinuous.

In combination with the constraint Equation (3.16) applied on an arbitrary location of the fluid-structure interface γ in the fluid domain Ω_f, a discontinuous interpolation of

the fluid pressure appears to be mandatory, see Baaijens (2001). A continuous interpolation of the fluid pressure, as in the Taylor-Hood family of discretization schemes, produces unsatisfactory results. Assuming, for example, homogeneous Dirichlet conditions along an immersed interface aligned with fluid element boundaries, the fluid pressure will be discontinuous across this interface. Hence, the use of a continuously interpolated pressure leads to erroneous results. Although in the fictitious domain method the interface γ is not necessarily aligned with element boundaries of the fluid domain, a discontinuity in the pressure field may be expected.

The discretization of the thin-walled valve leaflets requires that the element aspect ratio, defined as the ratio between the smallest and largest dimension of an element, should not exceed 1:7 to simulate a correct bending behaviour. Numerical experiments showed that larger ratios introduce artificial stiffness leading to incorrect motion of the leaflets.

The discretizations $\mathcal{T}_f$ and $\mathcal{T}_s$ can be chosen irrespective of each other. Moreover, the discretization of the Lagrange multipliers, i.e. $\mathcal{T}_\gamma$, that operate on the fluid-structure boundary γ can be chosen independently of $\mathcal{T}_f$ and $\mathcal{T}_s$. This kind of decoupling between $\mathcal{T}_f$, $\mathcal{T}_s$ and $\mathcal{T}_\gamma$ makes the fictitious domain approach very attractive for problems with moving boundaries. However, $\mathcal{T}_\gamma$ has to be chosen such that it does not introduce spurious modes or locking in the other degrees of freedom (Brezzi, 1974), and is therefore subjected to similar stability considerations as the discretization of the pressure degrees of freedom in the mixed formulation. So, here we encounter the limitation of the fictitious domain method. Stability reasons require for the mesh sizes that $h_{\Omega_f} < h_\gamma$ and $h_{\Omega_s} < h_\gamma$. However, the accuracy with respect to fluid-structure coupling is enhanced by requiring $h_{\Omega_f} > h_\gamma$ and $h_{\Omega_s} > h_\gamma$. As a result it is complicated to generate a discretization of the (moving) surface on which the Lagrange multiplier is applied.

In De Hart *et al.* (2000) and Chapter 2, where $h_{\Omega_f} \approx h_{\Omega_s}$ was used, this discrepancy is dealt with by choosing the discretization of $\vec{\lambda}$, and hence also $\vec{\ell}$, linear, discontinuous and spatially coincident with element boundaries of the structural domain: In general, the interpolation of the Lagrange multiplier field should be chosen at least one order lower than the interpolation order of the velocity and displacement field, as otherwise locking in the other degrees of freedom is introduced.

Considering the restrictions of the aspect ratio for $\mathcal{T}_s$ the relation between the mesh sizes h_{Ω_f} and h_{Ω_s} is such that $h_{\Omega_f} > h_{\Omega_s}$. Consequently, a discretization as used by De Hart *et al.* (2000) and in Chapter 2 is not applied here. Instead, each component of $\vec{\lambda}$ is approximated with a piecewise constant, making the distance between two points in $\mathcal{T}_\gamma$ less constrained. Here, N control points, $\vec{x}_{\lambda_k}, k = 1, 2, \ldots, N$ are introduced on the boundary γ and positioned in the centers of the structural element sides coinciding with γ (Figure 3.3). At these control points the fluid-structure coupling (3.16) is enforced. A similar approach was adopted by Bertrand *et al.* (1997). Now the approximation of the weighting function $\vec{\ell}^h$ that expresses the local operation of the Lagrange multiplier is a Dirac function $\delta(\vec{x})$, with $\vec{x}$ the field of material points, yielding

$$\vec{\ell}^h = \sum_{k=1}^{N} \vec{\ell}_k \delta(\vec{x} - \vec{x}_{\lambda_k}). \tag{3.20}$$

It should be mentioned that many other approaches are possible to define the interpolation for the weighting functions of the Lagrange multipliers. The above choice is

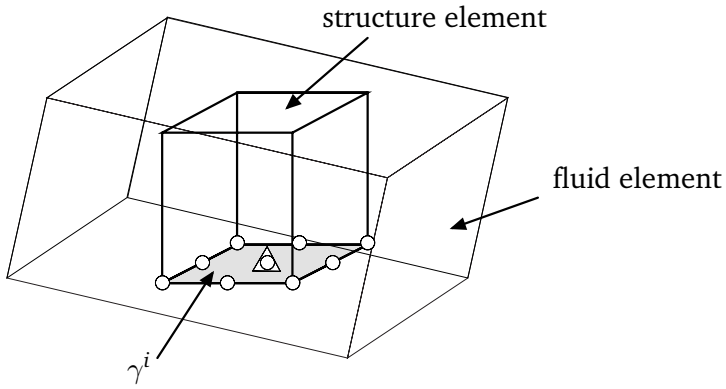

Figure 3.3: *Sample of a structural element inside a fluid element. The structural nodal points at the interface γ are denoted by $\circ$. The control point at which the Lagrange multiplier is defined is denoted by $\triangle$.*

founded on experiences from numerical experiments.

Time discretization of (3.17) is achieved using an implicit, backward-Euler scheme. Consider the time interval $t^n \rightarrow t^{n+1}$, with time step $\Delta t = t^{n+1} - t^n$, then

$$\frac{\partial \vec{v}_f}{\partial t} \approx \frac{\vec{v}_f^{\,n+1} - \vec{v}_f^{\,n}}{\Delta t}. \tag{3.21}$$

This choice leads to a scheme that is first-order accurate in time.

All integrals appearing in the formulations (3.17) to (3.19) are computed by means of a Gaussian quadrature integration rule, except for the integrals defined on γ, which are, with the above choice for the weighting functions, reduced to piecewise constants. For each control point at which the Lagrange multiplier related constant is computed, the structural velocity is obtained trivially since the spatial location of the control point coincides with the center of the associated structural element side along γ (Figure 3.3). However, the interpolation of the fluid velocity to the control points must be computed. This requires identification of the fluid element and the isoparametric coordinates of the fluid particle coincident with the spatial location of the control point. Once these coordinates are known, the fluid velocity at the control point can be expressed in terms of the nodal fluid velocities.

After discretization the finite element equations can be derived. Detail on the finite element implementation of the fluid-structure interaction problem can be found in Appendix A.

3.5 Solution procedure

The problem defined by (3.17) to (3.19) renders a non-linear system of algebraic equations which is linearized using Newton's method. The procedure used in this work to solve this coupled problem is based on a fully coupled approach (Appendix D) using a BiCGStab iterative solver with a preconditioner according to an incomplete LU factorization (Saad, 1996). Hence, the fluid and structure unknowns are solved simultaneously based on the integrated method (Cuvelier *et al.*, 1986). Within each time

step a Newton-Raphson iterative procedure is adopted to obtain a converged solution with respect to the fluid and structural velocity fields, the pressure fields and Lagrange multipliers. At each iteration the velocity field of the structure is fully coupled to the velocity field of the fluid. This obviates the need for an iterative procedure between the fluid and structural subproblems circumventing numerical instabilities, which will be discussed briefly hereafter. During the iterative procedure the fluid-structure coupling through Equation (3.19) is enforced using the location of γ defined at the beginning of the current time step. Enforcement on the most recently computed location of γ, as is done in the two-dimensional case (De Hart *et al.*, 2000, and Chapter 2), reduces the convergence rate of the three-dimensional application leading to a computationally inefficient procedure.

A weakly coupled strategy (appendix D) to solve the fluid and structural problem separately, as used in the staggered procedures described by Felippa *et al.* (1998) and Lesoinne M. *et al.* (1998), fails for stability reasons. This strategy involves transport of surface tractions from the fluid domain to the structural domain and displacement fields vice versa (Farhat *et al.*, 1998; Rutten, 1998; Wall *et al.*, 1998). During the opening and closing phase of the aortic valve the leaflets show very low resistance to bending. Enforcing the surface tractions computed from the fluid problem will result in an over-estimated displacement field for the leaflet to obtain internal stresses that balance the tractions. Application of this displacement field to the fluid domain invokes instability of the system. An alternative strategy involves transport of the computed fluid velocity field to the structural domain. However, the leaflet structure is designed to bear tensile stresses rather than compressive stresses. Consequently, application of the computed fluid velocity field to the leaflet structure may introduce unrealistic internal stresses, which would lead to erroneous results initiating instability when coupled back to the fluid. Attempts to make these, from a computational point of view, efficient procedures successful, using for example underrelaxation schemes, unfortunately failed.

3.6 Application to the aortic valve

The motion of a stented aortic valve and the blood flow through it are analyzed. In this section, the results are presented in terms of the computed fluid velocities, structural displacements and structural stresses. First, the model properties, such as geometrical and material properties are given, followed by the appropriate boundary conditions required for this system. A discussion on these results is given in the last subsection.

3.6.1 Model properties

The aortic valve consists of three highly flexible leaflets, which are attached to the aortic root from one commissural point along a doubly curved line (aortic ring) towards a second commissural point, see Figure 3.4(a) to (c). Behind each leaflet the aortic root bulbs into a sinus cavity to form the beginning of the ascending aorta. Figure 3.5 shows the relevant dimensions, which have frequently been used to describe the valve's geometry. The values of these dimensions, based on the geometry of previously developed prototype valves (Cacciola, 1998; De Hart *et al.*, 1998), are summarized in Table 3.1. The adopted values of the material parameters are also given in this table.

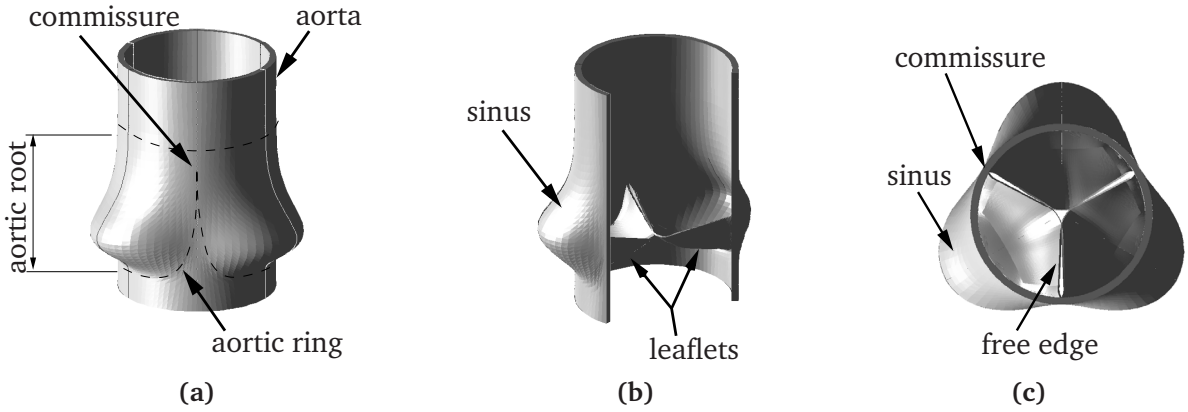

Figure 3.4: *Sketches of the aortic valve: side view of the complete valve (a), after dissection of one leaflet with corresponding sinus wall (b), and top view.*

Although in reality the three leaflets are not precisely identical, it is assumed that they are similar enough to permit a general description of a valve with trileaflet symmetry. Hence, only $\frac{1}{6}$ of the valve is considered in the model (Figure 3.6(b)), which contains approximately 20,000 fluid and 6,500 structural degrees of freedom. The configuration shown in this figure is taken as the initial, stress free condition of the model. The model is bounded in circumferential direction by the symmetry surface, which intersects through half of one leaflet, and by the contact surface, at which two adjacent leaflets come into contact during the closing phase (Figure 3.6(a)). In axial direction the model is bounded by the ventricular (inflow) and aortic (outflow) plane (Figure 3.6(c)), and obviously, in radial direction by the aortic wall, which is assumed to be rigid to mimic a stented valve. The leaflet is fixed to the aortic wall using homogeneous Dirichlet conditions imposed over the full thickness of the valve. Moreover, homogeneous Dirichlet conditions are imposed to suppress out of plane motion for the fluid and leaflet at the symmetry surface and for the fluid only at the contact surface. No-slip conditions are enforced at the fluid-wall surface. The fluid-structure coupling at the contact surface prevents the leaflet from penetrating this surface for sufficiently small time steps. The model is loaded during the systolic phase by ventricular and aortic pressure curves (Figure 3.7), to demonstrate the applicability of the presented method. The pressures are applied to the fluid domain at the inflow and outflow surfaces in 100 successive time steps for this time span.

Geometric properties					Material properties		
r [mm]	d_s [mm]	h_s [mm]	h_c [mm]	t_l [μm]	η_f [Pa·s]	ρ_f [$\frac{\text{kg}}{\text{m}^3}$]	G [MPa]
12.0	5.75	21.0	10.5	200.0	$4.0{\cdot}10^{-3}$	$1.0{\cdot}10^{3}$	$3.0{\cdot}10^{-2}$

Table 3.1: *Geometrical and material properties of the valve model .*

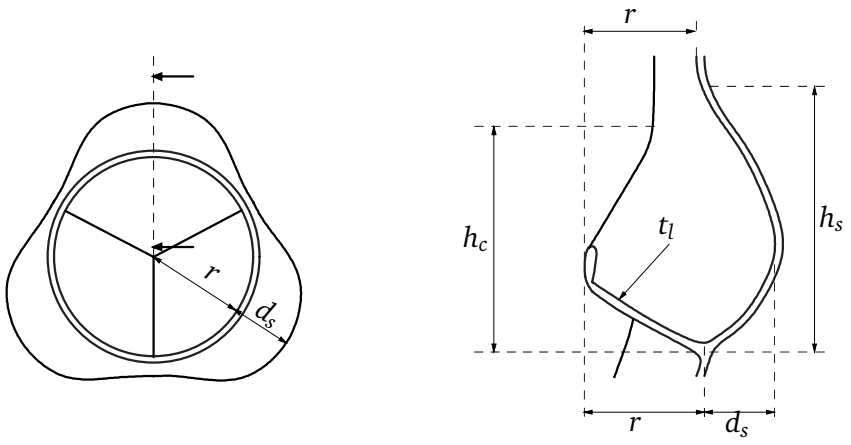

Figure 3.5: *Definition of relevant dimensions, which are used to describe the geometry of the model: r denotes the valve radius, d_s the sinus depth, h_s the sinus height, h_c the commissural height and t_l the leaflet thickness.*

3.6.2 Results

To obtain a global assessment of the system response to the applied load, 6 successive configurations of the valve with the corresponding fluid velocity vector field are shown in Figure 3.8. The opening behaviour is typical for stented valves (Cacciola, 1998) showing high curvatures of the free edge (Figure 3.8(b)). The Reynolds number, defined as $Re = \frac{\rho_f V r}{\eta_f}$, reaches a value of 900 at peak systolic mainstream velocity, i.e. $V = 300$ [mm/s] at $t = 0.065$ [s]. However, the moment of complete opening corresponds to Figure 3.8(c), i.e. at $t = 0.0875$ [s]. The Strouhal number, defined as $Sr = \frac{r}{V\tau}$, with $\tau(\approx 0.12)$ the time span from maximum systolic flow to the onset of flow reversal (Figure 3.8(f)), is approximately 0.3. The physiological values of these numbers, however, read

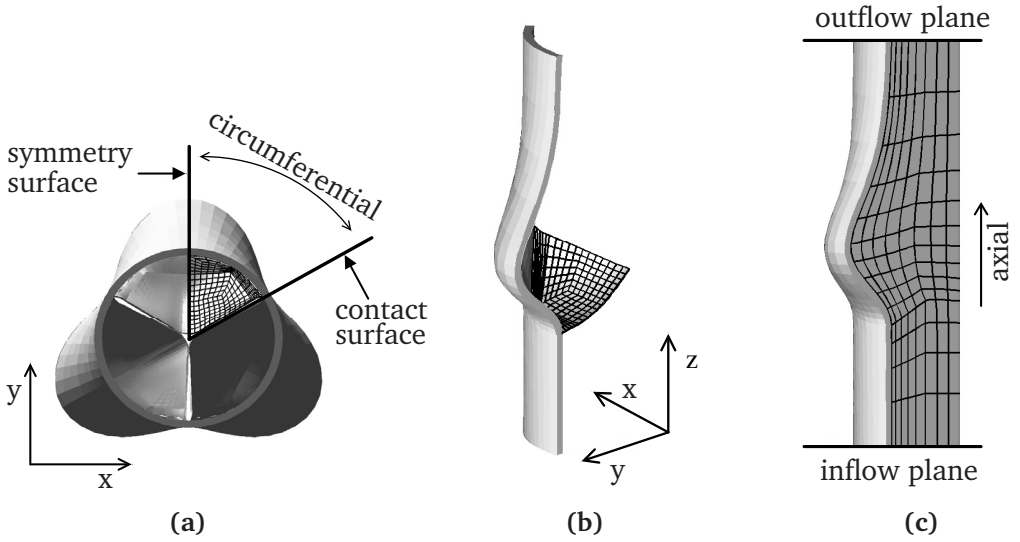

Figure 3.6: *Three-dimensional FEM model of the stented aortic valve: (a) part of the valve used for the computation, (b) structure mesh and (c) fluid mesh.*

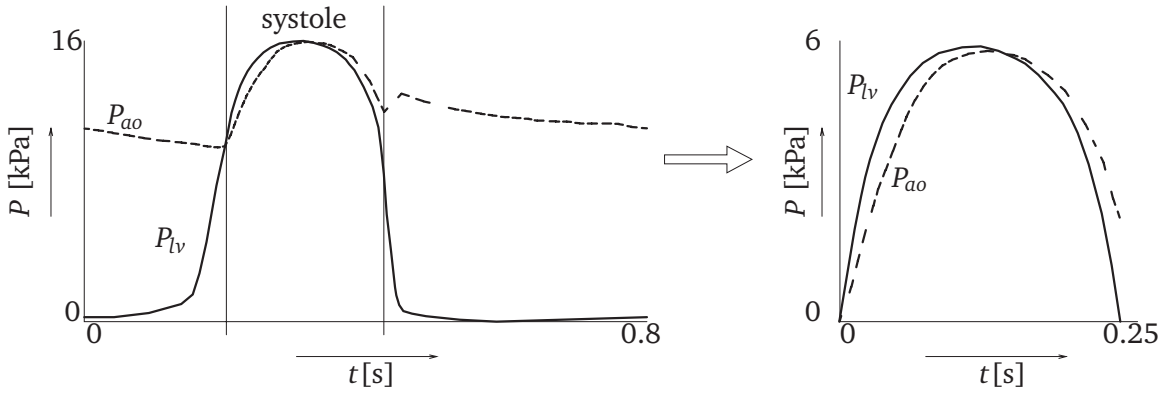

Figure 3.7: *Aortic (P_{ao}: dashed line) and left ventricular (P_{lv}: solid line) pressure curves during the cardiac cycle. The applied systolic pressures are given on the right hand side.*

$Re \approx 4500$ and $Sr \approx 0.06$. The application of these values is not feasible in view of the rather coarse fluid mesh, which is chosen such that both memory and CPU time are reasonable to demonstrate the proposed numerical method. On the other hand, the Womersly number $\alpha \approx 16.4$ is in fair agreement with the physiological value $(15-16)$, yielding that the instationary inertia forces dominate the viscous forces.

In Figure 3.9 the maximum principle Cauchy stresses are given. The stress scale is given in kPa and the maximum principle stresses vary from -50 [kPa] to 60 [kPa]. In the diastolic phase stress values in the order of MPa have been reported, e.g. see Black *et al.* (1991); Cacciola (1998); Chandran *et al.* (1991); De Hart *et al.* (1998); Krucinski *et al.* (1993). During the opening of the valve (Figure 3.9(a) and (b)) tensile stresses in the middle of the leaflets are more dominant on the aortic side of the leaflets, whereas compressive stresses are present at the ventricular side. This can clearly be observed in the left hand side figures and is caused by the high curvature in the symmetry plane, which intersects through half of the leaflets. Similar configurations have been measured by Gao *et al.* (2000) monitoring the leaflet motion in bioprosthetic heart valves with dual camera stereo photogrammetry. Near the fixation edge, however, tensile stresses appear on the ventricular side and compressive stresses on the aortic side. The stress distribution is rather inhomogeneous during this phase. The middle frame represents the initial phase of valve closing, which shows significant stresses in the middle of the leaflet. For this configuration the compressive stresses appear on the aortic side, whereas tensile stresses are more dominant on the ventricular side. This phenomenon shows a cyclic loading pattern of the aortic leaflets, which is believed to be important in the analysis of fatigue behaviour. The last two frames are taken at the end of the systolic phase, where a rapid closure of the valve occurs. The stresses in the leaflets are significantly increasing in this phase as they have to bear the increasing pressure gradient across the valve. As stated before, the simulation does not include the diastolic phase. Moreover, with the applied material parameters, the leaflet would undergo excessive deformations to balance the diastolic pressure gradient. In reality, the natural valve shows a complex fiber-reinforced composite texture to be able to bear diastolic pressures.

The velocity vector field near the leaflets is given in Figure 3.10(a) to (f). In frame (a) the valve is shown in its initial (stress free) configuration, which corresponds to a closed position. During the acceleration phase (frame (b)) a forward flow is observed

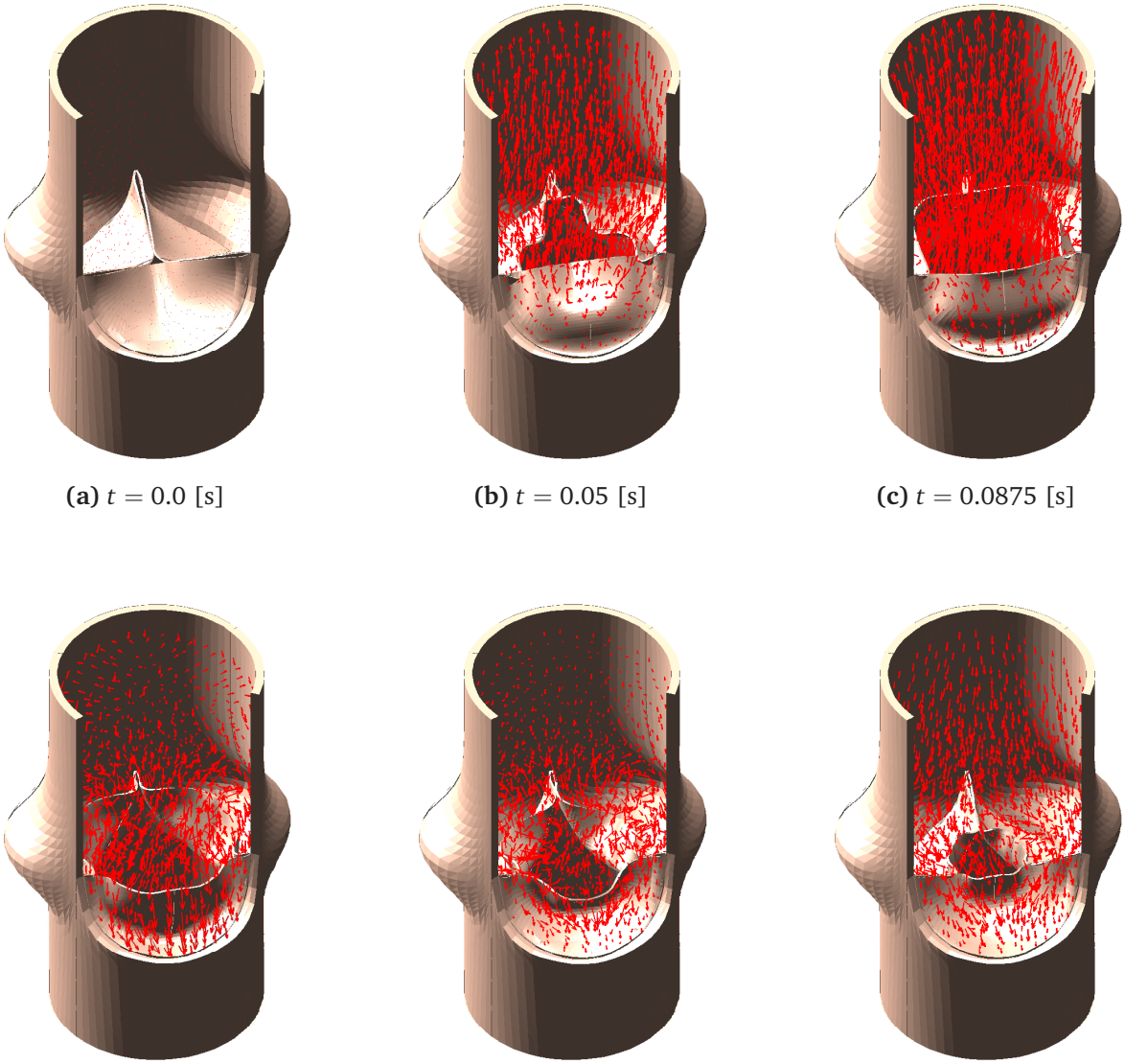

(a) $t = 0.0$ [s] **(b)** $t = 0.05$ [s] **(c)** $t = 0.0875$ [s]

(d) $t = 0.125$ [s] **(e)** $t = 0.175$ [s] **(f)** $t = 0.2125$ [s]

Figure 3.8: *Configurations of the stented valve taken at 6 successive points in time during the systolic phase. The fluid velocity vector field is also shown.*

for every point of the fluid domain, including in the sinus cavity (i.e. wash-out). For the fully opened valve (frame (c)) the flow is more central and very little flow in the sinus cavity is observed. At the moment of complete valve opening, however, the flow has started to decelerate already. During the deceleration phase recirculation at the leaflet free edge precedes vortex development in the sinus cavity and the valve is driven to a closed position (frames (d) and (e)). Similar results were found by Van Steenhoven *et al.* (1982) for *in vivo* experiments with approximately the same peak systolic velocity. A completely closed valve is obtained after reversal of the pressure gradient, leading to a little amount of back flow (frame (f)). This last phase of the leaflets motion results in a quick final closure of the valve. In conclusion the leaflets of the stented valve appear to be moving in an essentially kinematical process governed by the fluid flow.

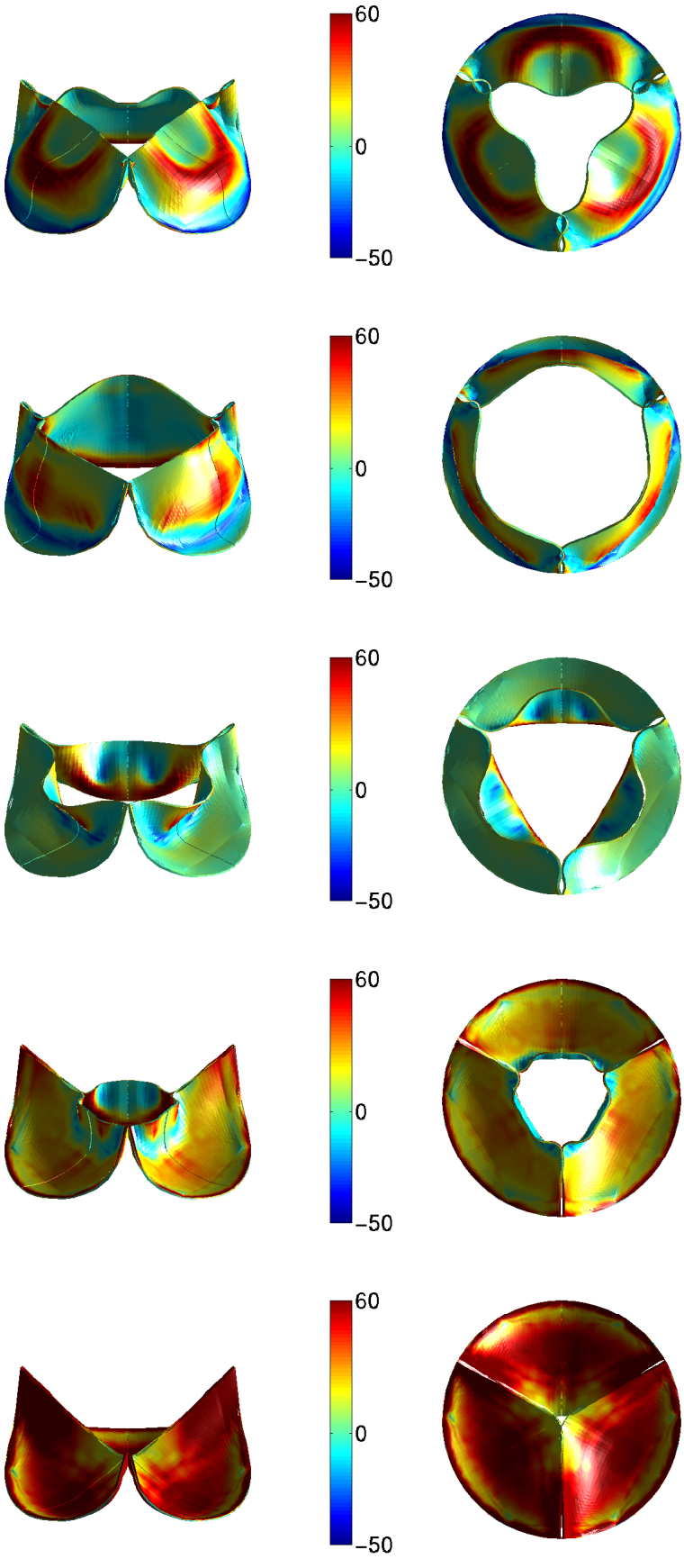

(a) $t = 0.05$ [s]

(b) $t = 0.0875$ [s]

(c) $t = 0.175$ [s]

(d) $t = 0.2125$ [s]

(e) $t = 0.25$ [s]

Figure 3.9: *Maximum principle Cauchy stresses in the leaflets during the systolic phase of the cardiac cycle. The stress scale is given in [kPa].*

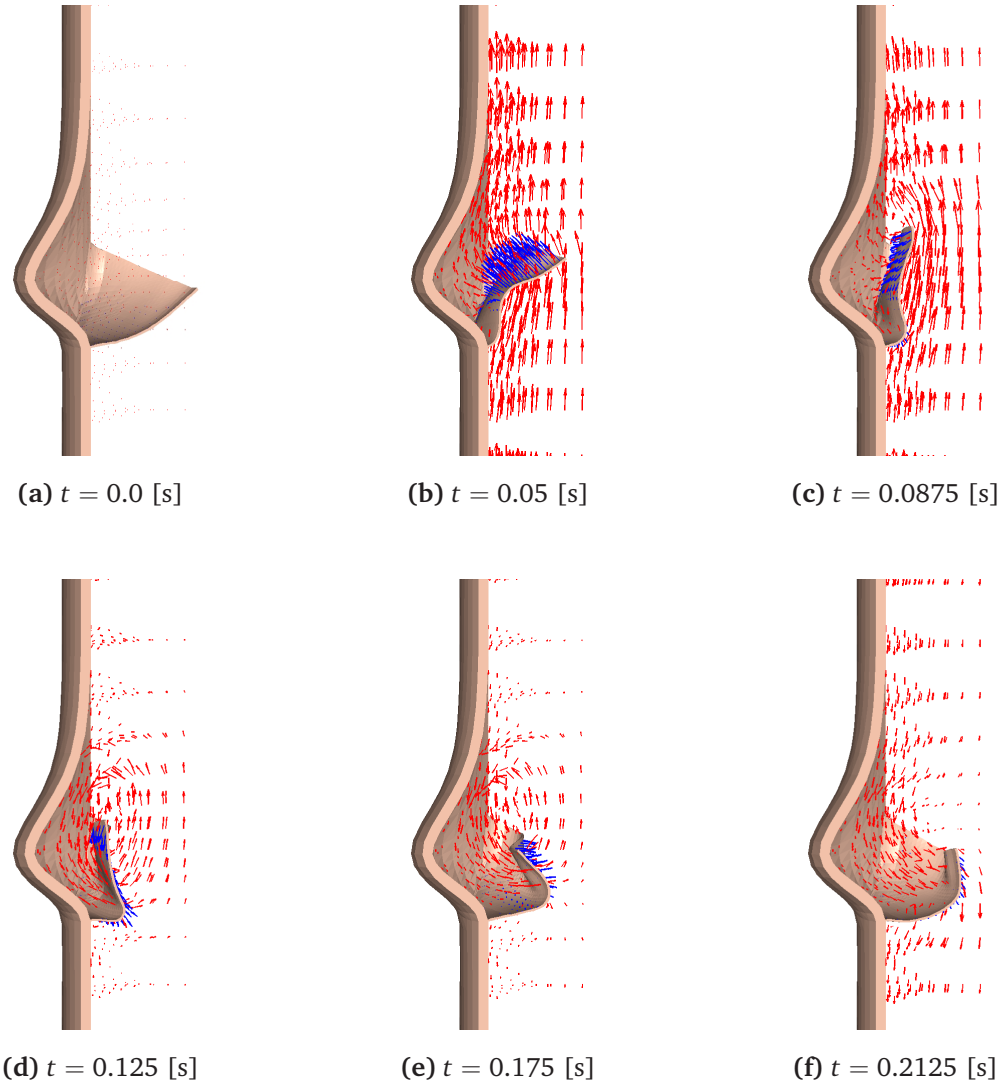

(a) $t = 0.0$ [s] **(b)** $t = 0.05$ [s] **(c)** $t = 0.0875$ [s]

(d) $t = 0.125$ [s] **(e)** $t = 0.175$ [s] **(f)** $t = 0.2125$ [s]

Figure 3.10: *Velocity vector field for 6 successive points in time.*

3.7 Discussion

A three-dimensional fictitious domain method is applied to model fluid-structure interaction in the aortic valve. The method is based on the imposition of kinematical constraints, using Lagrange multipliers, which represent the no-slip conditions along the fluid-structure interface. The implementation of this numerical technique is performed within the framework of the finite element method encoded in the SEPRAN software package (Segal, 2000). The essential feature of this approach is that independent discretizations of the computational domains are allowed. This yields that the fluid finite element mesh is not altered or interrupted in any way by the presence of submerged structures. Conventional mesh update strategies, such as remeshing or arbitrary Lagrange-Euler techniques, consequently are superfluous.

The set of discretized linear algebraic equations is solved in a fully coupled manner. This leads to a solution procedure in which the fluid and structure unknowns are solved simultaneously, circumventing the judicious choice of the state variables to be trans-

ported from one system to the other, which is common practice in staggered procedures. However, the condition of the finite element matrix of the total system is affected, since the matrix entries display large variations caused by the difference in magnitude of the material parameters that describe the fluid and structure. Moreover, the solvability appears to be highly influenced by the number of additional Lagrange multipliers with respect to the number of fluid unknowns. For the application presented in this chapter, the number of coupling constraints is chosen such that a BiCGStab iterative solver with a preconditioner based on an incomplete LU factorization using extra fill-in (Saad, 1996) is still feasible for reasonable amounts of both memory and CPU time. The convergence criterion for the BiCGStab iteration process is based on the maximum residual norm for which the tolerance is set to 10^{-4}. In the Newton-Raphson iteration process the convergence criterion is based on the norm of the change of the state variables in two successive iterations relative to the norm computed from the last converged solution with the tolerance set to 10^{-5}. These settings appeared to be sufficient for obtaining a solution indifferent to sharper tolerances.

The system is solved on a 64-bit Alpha 21264DP platform with a 667 MHz processor and an applicable memory allocation of 4 GB of which 20% is used. The ILU factorization takes 90% of the computation time and, in practice, must be performed after two time steps on average, since the changing position of the structure in the fluid domain involves a different mapping of the matrix entries associated with the Lagrange multipliers. For the valve model, having approximately 26,500 degrees of freedom, this resulted in a computation time of 35 minutes per time step to obtain a converged solution.

The fictitious domain method is applied to simulate the response of a stented aortic valve to externally applied ventricular and aortic pressures. Results show that during systole the valve leaflets are moving with the fluid in an essentially kinematical process governed by the fluid motion. The maximum pressure difference is taken such that the Reynolds and Strouhal number approximate 900 and 0.3, respectively. An analysis with the physiological Reynolds number ($Re = 4500$) and Strouhal number ($Sr = 0.06$) would lead to commonly expected numerical instabilities for a mesh coarseness as used in this model. Moreover, in this chapter we focus on the three-dimensional application of the numerical method to investigate the importance of fluid-structure interaction rather than on the approximation of the physiological situation.

Contact between two adjacent leaflets has not been implemented in the applied computer code. Instead, it is expected that penetration of the leaflets is circumvented implicitly by using the fictitious domain method, since at the contact surface fluid velocities in the direction normal to this surface are suppressed. From Figures 3.9(d) and (e) this is observed at the free edges of the leaflets. However, in Figure 3.9(a) some penetration is seen, which is caused by the relative large displacement of the free edge within one time step. A decrease in time step size or an increase in the density $\mathcal{T}_\gamma$ near this area, i.e. adding more coupling constraints, would prevent penetration.

Although the model parameters are not such that a physiological correct behaviour is attained, the adopted methods appear to be applicable in the three-dimensional fluid-structure interaction analysis of the aortic valve. Valve models that more closely resemble the physiological situation in terms of anisotropic material behaviour, compliant aortic root and high Reynolds number flow, are elaborated in Chapter 4 and 5.

References

Baaijens, F.P.T., 2001. A fictitious domain/mortar element method for fluid-structure interaction. *International Journal for Numerical Methods in Fluids*, **35**(7): 743-761.

Bathe, K.J, 1982. *Finite Element Procedures in Engineering Analysis*. Prentice-Hall, Inc., New Jersey, USA.

Bertrand, F., Tanguy, P.A., Thibault, F., 1997. A three-dimensional fictitious domain method for incompressible fluid flow problems. *International Journal for Numerical Methods in Fluids*, **25**(6): 719-736.

Black, M.M., Howard, I.C., Huang, X., Patterson, E.A., 1991. A three-dimensional analysis of a bioprosthetic heart valve. *Journal of Biomechanics*. **24**(9): 793-801.

Brezzi, F., 1974. On the existence, uniqueness and approximation of saddle-point problems arising from Lagrange multipliers. *RAIRO - Operations Research*, **R2**: 129-151.

Cacciola, G., 1998. *Design, Simulation and Manufacturing of Fiber-Reinforced Polymer Heart Valves*. Ph.D. thesis, Eindhoven University of Technology, Eindhoven. *http://www.mate.tue.nl/mate/publications*.

Cacciola, G., Peters, G.W.M., Schreurs, P.J.G., 2000. A three-dimensional mechanical analysis of a stentless fibre-reinforced aortic valve prosthesis. *Journal of Biomechanics*, **33**(5): 521-530.

Caro, C.G., Pedley, J.G., Schroter, R.C., Seed, W.A., 1978. *The Mechanics of the Circulation*. Oxford University Press, Oxford.

Chandran, K.B., Kim, H.H., Han, G., 1991. Stress distribution on the cusps of a polyurethane trileaflet heart valve prosthesis in the closed position. *Journal of Biomechanics*, **24**(6): 385-395.

Cuvelier, C., Segal, A., Van Steenhoven, A.A., 1986. *Finite Element Methods and Navier-Stokes Equations*. D. Reidel Publishing Company, Dordrecht.

De Hart, J., Cacciola, G., Schreurs, P.J.G., Peters, G.W.M., 1998. A three-dimensional analysis of a fibre-reinforced aortic valve prosthesis. *Journal of Biomechanics*, **31**(7): 629-638.

De Hart, J., Peters, G.W.M., Schreurs, P.J.G., Baaijens, F.P.T., 2000. A two-dimensional fluid-structure interaction model of the aortic valve. *Journal of Biomechanics*, **33**(9): 1079-1088.

Donea, J., Giuliani, S., Halleux, J.P., 1982. An arbitrary Lagrangian-Eulerian finite element method for transient dynamic fluid-structure interactions. *Computer Methods in Applied Mechanics and Engineering*, **33**: 689-723.

Farhat, C., Lesoinne, M., LeTallec, P., 1998. Load and motion transfer algorithms for fluid/structure interaction problems with non-matching discrete interfaces: momentum and energy conservation, optimal discretization and application to aeroelastics. *Computer Methods in Applied Mechanics and Engineering*, **157**: 95-114.

Felippa, C.A., Park, K.C., Farhat, C., 1998. Partitioned analysis of coupled mechanical systems. *Computer Methods in Applied Mechanics and Engineering*, **190**: 3247-3270.

Fortin, M., Glowinski, R., 1983. *The Augmented Lagrangian method*. North-Holland, Amsterdam.

Gao, Z.B., Pandya, S., Hosein, N., Sacks, M.S., Hwang, N.H.C., 2000. Bioprosthetic heart valve leaflet motion monitored by dual camera stereo photogrammetry. *Journal of Biomechanics*, **33**(2): 199-207.

Glowinski, R., Pan, T.-W., Periaux, J., 1994. A fictitious domain method for Dirichlet problem and applications. *Computer Methods in Applied Mechanics and Engineering*, **111**: 283-303.

Glowinski, R., T.-W., Pan, Periaux, J., 1998. Distributed Lagrange multiplier methods for incompressible viscous flow around moving rigid bodies. *Computer Methods in Applied Mechanics and Engineering*, **151**: 181-194.

Horsten, J.B.A.M., 1990. *On the Analysis of Moving Heart Valves: a numerical fluid-structure interaction model.* Ph.D. thesis, Eindhoven University of Technology, Eindhoven.

Hughes, T.J.R., 1987. *The Finite Element Method: Linear Static and Dynamic Finite Element Analysis*. Prentice-Hall, Inc., New Jersey.

Hyman, M.A., 1952. Non-iterative numerical solution of boundary-value problems. *Applied Scientific Research*, Section B **2**: 325-351.

Krucinski, S., Vesely, I., Dokainish, M.A., Campbell, G., 1993. Numerical simulation of leaflet flexure in bioprosthetic valves mounted on rigid and expansile stents. *Journal of Biomechanics*, **26**(8): 929-943.

Lesoinne, M, Farhat, C., 1998. Improved staggered algorithms for the serial and parallel solution of three-dimensional nonlinear transient aeroelastic problems. *In Proceedings of the WCCM IV Conference on Computational Mechanics*, edited by E. Oñate and S. Idelsohn, CIMNE, Barcelona.

LeVeque, R.J., Li, Z., 1997. Immersed interface methods for Stokes flow with elastic boundaries or surface tension. *SIAM Journal on Scientific Computing*, **18**(3): 709-735.

Makhijani, V.B., Yang, H.Q., Dionne, P.J., Thubrikar, M.J., 1997. Three-dimensional coupled fluid-structure simulation of pericardial bioprosthetic aortic valve functioning. *ASAIO Journal*, **43**(5): M387-M392.

Perng, C.Y., Murthy, J., 1993. Sliding mesh technique for simulation of flow in mixing tanks. *American Society of Mechanical Engineers*, 1-9.

Peskin, C.S., 1977. Numerical analysis of blood flow in the heart. *Journal of Computational Physics*, **25**(3): 220-252.

Peskin, C.S., McQueen, D.M., 1995. A general method for the computer simulation of biological systems interacting with fluids. *Symposia of The Society for Experimental Biology*, **49**: 265-276.

Rai, M.M., 1985. Navier-Stokes simulation of rotor-stator interaction using patched and overlaid grids. *AIAA Paper*, 282-298.

Rutten, M.C.M., 1998. *Fluid-Solid Interaction in Large Arteries*. Ph.D. thesis, Eindhoven University of Technology, Eindhoven. *http://www.mate.tue.nl/mate/publications*.

Saad, Y., 1996. *Iterative Methods for Sparse Linear Systems*. PWS Publishing Company, Boston.

Saul'ev, V.K., 1963. On solving boundary-value problems on high-performance computers by fictitious-domain methods. *Siberian Mathematical Journal*, **4**: 912-925.

Segal, G., 2000. *SEPRAN Introduction, User's Manual, Programmer's Guide and Standard Problems*. Ingenieursbureau SEPRA, Leidschendam.

Sheehy, P., Tanguy, P.A., Blouin, D., 1994. Finite element model for complex profile calibration. *Polymer Engineering and Science*, **34**(8): 650-656.

Van Steenhoven, A.A., Veenstra, P.C., 1982. The effect of some hemodynamic factors on the behaviour of the aortic valve. *Journal of Biomechanics*, **15**(12): 941-950.

Wall, W.A., Ekkehard, R., 1998. Fluid-structure interaction based upon a stabilized (ALE) finite element method. *In Proceedings of the WCCM IV Conference on Computational Mechanics*, edited by E. Oñate and S. Idelsohn, CIMNE, Barcelona.

Chapter 4

Computational Analysis of a Fiber-Reinforced Stented Aortic Valve[1]

Calcification and/or tissue degeneration are failure mechanisms that are often observed in aortic valve bioprostheses, synthetic prostheses and diseased natural valves. The physical effect on cardiac performance can be expressed in clinical terms of e.g. cardiac output, cardiac work and pressure drop over the valve. Leaflet fiber-reinforcement is a natural stress reducing mechanism that contributes to a life-long functioning of the valve. However, the actual effect on the mechanical and hemodynamical performance is difficult to study both 'in vivo' and 'in vitro'. To this end a numerical model of a fiber-reinforced stented valve is developed, which is based on a fictitious domain formulation using Lagrange multipliers to describe the interaction between the blood and the leaflets. This numerical technique is integrated within the finite element framework and demonstrated for high Reynolds number flows and physiologically realistic material characteristics. Both structural mechanical and fluid dynamical aspect are analyzed during the systolic phase of the cardiac cycle. Results show that fiber-reinforcement significantly improves the mechanical behaviour of the valve, while the fluid dynamical performance is preserved.

[1]The contents of this chapter are submitted to the *Journal of Biomechanics*, under the title:

A computational fluid-structure interaction analysis of a fiber-reinforced stented aortic valve
De Hart, J., Peters, G.W.M., Schreurs, P.J.G., Baaijens, F.P.T.

4.1 Introduction

Disfunctional heart valves are increasingly replaced by prosthetic devices. Commercially available prostheses are, up to now, either mechanical or biological. However, thromboembolic complications and tissue degeneration are still injurious for these substitutes. Attempts to make fully synthetic prostheses have not been very successful either, i.e. they are not reliable for long-term applications. The failure mechanisms observed in bioprosthetic devices are similar to those reported in synthetic prostheses (Bernacca *et al.*, 1995; Wheatly *et al.*, 1987). Regions of high bending and shear stresses in the leaflets during opening and closing have been suggested to cause tissue degeneration leading to calcification and ultimately failure of the valve. Fiber-reinforcement of the leaflets efficiently reduces critical stresses in the delicate components of the leaflet tissue (De Hart *et al.*, 1998; Cacciola, 1998). This mechanism is essential for the long-term performance of natural valves. Since stresses are difficult to measure experimentally, computational modeling can enhance the development of improved prosthetic devices.

In the computational analysis of the aortic valve system most frequently structural models have been considered, see Black *et al.* (1991); Cacciola (1998); Chandran *et al.* (1991); Krucinski *et al.* (1993) and many others. However, the clinical performance of a valve is measured by both its mechanical and hemodynamical characteristics. Hence, the interaction of the valve with the blood is essential in evaluating its functioning. To carry out such fluid-structure interaction analyses we adopt a fictitious domain technique which is elaborated in De Hart *et al.* (2001a) and Chapter 3.

In the fictitious domain formulation the different mathematical representations of the fluid and structure balance equations can be maintained, allowing convenient classical descriptions for each of these subsystems. Fictitious domain methods provide a way to circumvent fluid mesh update strategies to accommodate for the large leaflet motion within the computational fluid domain. Instead, dissimilar and independent fluid and structural discretizations are allowed, such that the fluid mesh is not altered or interrupted by the presence of valve leaflets. Here, fluid-structure coupling is realized by a set of kinematical constraints (the no-slip conditions along the fluid-structure interface), which are enforced through Lagrange multipliers (Bertrand *et al.*, 1997; Glowinski *et al.*, 1998; LeVeque and Li, 1997; Patankar *et al.*, 2000; Singh *et al.*, 2000). Although fictitious domain methods are generally used to describe the motion (usually known *a priori*) of rigid structures immersed in fluid, the method presented by Baaijens (2001), De Hart *et al.* (2001a) and in Chapter 3 is applicable to problems with deformable structures of which the motion is not known *a priori* but depends on the surrounding fluid flow. Experimental validation of this method, applied to a two-dimensional aortic valve, is demonstrated in Chapter 2 and by De Hart *et al.* (2000).

In this chapter the application of leaflet fiber-reinforcement to a stented aortic valve is analyzed. The physiological condition under which the valve operates is, within the numerical applicability, adopted to obtain clinical relevance from the computational results. First, the problem definition and governing equations for the fluid and structural phase are summarized. Next, the coupling between these two phases is briefly described and a fictitious domain formulation is given. The results are presented in terms of structural displacements, stresses, and fluid velocities, fluid wash-out and pressures.

Moreover, the findings for the fiber-reinforced model will be compared to a similar isotropic variant.

4.2 Problem definition and governing equations

Computational analysis of a stented aortic valve requires mathematical descriptions of the valve leaflets and the blood. Blood is a concentrated suspension of blood cells in plasma. Its rheological behaviour is dominated by the red blood cells. Assuming homogeneity of the concentration a macroscopic continuum model can be used to describe the blood flow. In our models the blood flow is considered to be isothermal and incompressible. It appears that in the case of properly working heart valves, the fluid flow is laminar (Nerem *et al.*, 1972). Hence, in absence of body forces, the equation of motion and the continuity equation, with respect to an Eulerian reference frame, read

$$\rho_f\left(\frac{\partial \vec{v}_f}{\partial t} + \vec{v}_f \cdot \vec{\nabla}\vec{v}_f\right) = \vec{\nabla} \cdot (-p_f \boldsymbol{I} + \boldsymbol{\tau}_f), \tag{4.1}$$

$$\vec{\nabla} \cdot \vec{v}_f = 0, \tag{4.2}$$

where ρ_f denotes the density, t the time, $\vec{v}_f$ is the velocity, p_f the pressure, $\boldsymbol{\tau}_f$ the extra fluid stress tensor and $\vec{\nabla}$ the gradient operator. Assuming a Newtonian behaviour of the blood (Caro *et al.*, 1978) the extra stress tensor can be written in terms of the rate-of-deformation tensor $\boldsymbol{D}_f$:

$$\boldsymbol{\tau}_f = 2\eta \boldsymbol{D}_f \quad ; \qquad \boldsymbol{D}_f = \frac{1}{2}\left(\vec{\nabla}\vec{v}_f + (\vec{\nabla}\vec{v}_f)^T\right), \tag{4.3}$$

with η the (constant) dynamic viscosity.

Scaling spatial coordinates with a characteristic length, e.g. the aortic valve radius r_a, velocities with a characteristic velocity, e.g. the peak (inflow) velocity V and time with a characteristic time, e.g. the flow deceleration time τ (measured from maximum flow to the onset of flow reversal), the dimensionless (*) representation of the well-known Navier-Stokes equation is given by

$$Sr\frac{\partial \vec{v}_f^*}{\partial t^*} + \vec{v}_f^* \cdot \vec{\nabla}^* \vec{v}_f^* = -\vec{\nabla}^* p^* + \frac{1}{Re} 2\vec{\nabla}^* \cdot \boldsymbol{D}_f^*, \tag{4.4}$$

where the Strouhal number Sr and the Reynolds number Re are defined as

$$Sr = \frac{r_a}{\tau V} \quad ; \qquad Re = \frac{\rho V r_a}{\eta}. \tag{4.5}$$

As fluid and structure density are nearly identical (buoyancy forces can be neglected), the contribution of the small leaflet mass to the inertia of the system is assumed to be insignificant. In absence of any body forces the momentum equation for the incompressible structure yields

$$\vec{\nabla} \cdot \boldsymbol{\sigma}_s = \vec{0}, \tag{4.6}$$

$$\det(\boldsymbol{F}) = 1, \tag{4.7}$$

where $\boldsymbol{\sigma}_s$ is the structural Cauchy stress tensor and **F** the deformation tensor defined as $\boldsymbol{F} = (\vec{\nabla}_0 \vec{x}_s)^T$, with $\vec{\nabla}_0$ the gradient operator with respect to the initial configuration and $\vec{x}_s$ the field of structural material points. The sets (4.1), (4.2) and (4.6), (4.7) must be supplemented with appropriate Dirichlet and Neumann conditions which are described further on.

As mentioned in the introduction the valve leaflets constitute a fiber-reinforced texture. The fiber/matrix structure renders an orthotropic incompressible composite (Sauren, 1981), of which the matrix is assumed to obey a Neo-Hookean material law according to

$$\boldsymbol{\sigma}_m = -p_m \boldsymbol{I} + \boldsymbol{\tau}_m \quad ; \qquad \boldsymbol{\tau}_m = G(\boldsymbol{B} - \boldsymbol{I}), \tag{4.8}$$

where p_m denotes the hydrostatic pressure, $\boldsymbol{I}$ the second-order unit tensor and $\boldsymbol{\tau}_m$ the extra stress tensor. The definition of $\boldsymbol{\tau}_m$ represents an isotropic hyperelastic behaviour with G the shear modulus and $\boldsymbol{B} = \boldsymbol{F} \cdot \boldsymbol{F}^T$ the Finger or left Cauchy-Green strain tensor. The fibers are modeled as a one-dimensional material exerting only tensile stress (σ_{fb}) in the fiber direction according to

$$\sigma_{fb} = c_1 \mu^2 \left(e^{c_2(\mu^2 - 1)} - 1 \right), \tag{4.9}$$

with c_1 and c_2 material constants and μ the fiber stretch (Van Oijen *et al.*, 2002). In terms of the deformation tensor $\boldsymbol{F}$ the fiber stretch can be defined as

$$\mu = \| \boldsymbol{F} \cdot \vec{e}_0 \|, \tag{4.10}$$

where the unit vector $\vec{e}_0$ represents the initial local fiber direction. Since $\boldsymbol{F}$ describes the deformation of the composite, matrix and fiber undergo the same deformation restricting fiber motion with respect to the matrix material.

The constitutive law for the leaflet composite consisting of N fiber layers can now be written as

$$\boldsymbol{\sigma}_s = -p_s \boldsymbol{I} + \boldsymbol{\tau}_s \;\; ; \quad \begin{cases} \boldsymbol{\tau}_s = \boldsymbol{\tau}_m + \displaystyle\sum_{k=1}^{N} \left[\theta_{fb_k} \left(\sigma_{fb_k} - \vec{e}_k \cdot \boldsymbol{\tau}_m \cdot \vec{e}_k \right) \vec{e}_k \vec{e}_k \right], & \mu \geq 1, \\ \boldsymbol{\tau}_s = \boldsymbol{\tau}_m, & \mu < 1 \end{cases} \tag{4.11}$$

with $p_s = p_m$, $\vec{e}_k$ the unit vector of the current local fiber direction and θ_{fb_k} the volume fraction of fiber k in the composite (Van Oijen *et al.*, 2002). Relation (4.11) is a continuum approximation, which states that in the fiber direction $\vec{e}_k$ the fiber stress and extra matrix stress contribute to $\boldsymbol{\tau}_s$ with fractions θ_{fb} and $1 - \theta_{fb}$, respectively (rule of mixtures).

The structural equilibrium equations (4.6) and (4.7) are described in an updated Lagrange formulation. In this formulation it is customary to take the displacement field $\vec{u}_s$ as the unknown. During a time interval $t^n \rightarrow t^{n+1}$, this field is defined as the difference in the position fields at t^n and t^{n+1}. However, for the interaction with the fluid, the structural velocity field is considered rather than the displacement field. To this end a first-order approximation for the structural velocity field is used:

$$\vec{v}_s = \frac{\vec{u}_s}{\Delta t} \tag{4.12}$$

with time step $\Delta t = t^{n+1} - t^n$.

4.3 Fluid-structure interaction

Fluid-structure interaction in a stented aortic valve involves a coupling of the fluid domain Ω_f (i.e. the blood) with immersed structures Ω_s (i.e. the valve leaflets). This coupling is straightforward if equal-order discretization of the fluid and structural domain is used and nodes and element boundaries coincide along the fluid-structure interface. However, in (4.1) and (4.2) the fluid domain is fixed in space, while in (4.6) and (4.7) the position of the structural domain changes and is not known *a priori*. Consequently, continuously updating the fluid mesh to accommodate for the motion of the structural domain requires remeshing or alternatively, an arbitrary Lagrange-Euler (ALE) formulation for the fluid domain. The change in mesh topology during remeshing introduces artificial diffusivity as history variables must be interpolated to the newly generated mesh. Moreover, this technique is difficult and/or time-consuming to perform with sufficient robustness and accuracy for three-dimensional problems. The ALE formulation is restricted to applications where the motion of the structural domain is such that, with preserved topology, the updated fluid mesh maintains a proper quality. To resolve the limitations of these mesh update strategies a fictitious domain method is used, which can deal with the large motion of the valve leaflets within the computational fluid domain. The mathematical formulation describing the interaction of the leaflets with the fluid is elaborated in De Hart *et al.* (2001a) and summarized here.

The basic idea of fictitious domain methods is to mathematically rewrite the problem defined on the fluid domain as a problem defined on an extended domain containing both the fluid and the immersed structure. To describe the presence of the immersed structure for this new problem we introduce kinematical (no-slip) constraints:

$$\vec{v}_f - \vec{v}_s = \vec{0}, \tag{4.13}$$

along the fluid-structure boundary γ. For the aortic valve leaflets these coupling constraints can be enforced along one side of the leaflet only, since their thickness is negligible as far the interaction with the fluid is considered. The Lagrange multiplier method (Fortin *et al.*, 1983; Bathe, 1982) is applied to weakly enforce the constraints using Lagrange multipliers $\vec{\lambda}$ (see Appendix B).

Without going into detail we present the fictitious domain formulation describing the fluid-structure interaction problem (De Hart *et al.*, 2001a):

$$\begin{aligned}
&\int_{\Omega_f} \vec{w}_f \cdot \left(\rho_f \frac{\partial \vec{v}_f}{\partial t} + \rho_f \vec{v}_f \cdot \vec{\nabla} \vec{v}_f \right) d\Omega_f + \int_{\Omega_f} (\vec{\nabla} \vec{w}_f)^T : 2\eta \boldsymbol{D}_f \, d\Omega_f - \\
&\qquad \int_{\Omega_f} (\vec{\nabla} \cdot \vec{w}_f) p_f \, d\Omega_f + \int_{\gamma} \vec{w}_f \cdot \vec{\lambda} \, d\gamma = \int_{\Gamma_f} \vec{w}_f \cdot \vec{t}_f \, d\Gamma_f, \\
&\int_{\Omega_f} q_f (\vec{\nabla} \cdot \vec{v}_f) \, d\Omega_f = 0,
\end{aligned} \tag{4.14}$$

$$\begin{aligned}
&\int_{\Omega_s} (\vec{\nabla} \vec{w}_s)^T : \boldsymbol{\tau}_s \, d\Omega_s - \int_{\Omega_s} (\vec{\nabla} \cdot \vec{w}_s) p_s \, d\Omega_s - \int_{\gamma} \vec{w}_s \cdot \vec{\lambda} \, d\gamma = 0, \\
&\int_{\Omega_s} q_s \left(\det(\boldsymbol{F}) - 1 \right) d\Omega_s = 0,
\end{aligned} \tag{4.15}$$

$$\int_\gamma \vec{\ell} \cdot (\vec{v}_f - \vec{v}_s)\, d\gamma = 0, \tag{4.16}$$

which must hold for all admissible weighting functions $\vec{w}_f, q_f, \vec{w}_s, q_s$ and $\vec{\ell}$. The variable $\vec{t}_f = (-p_f \boldsymbol{I} + 2\eta \boldsymbol{D}_f) \cdot \vec{n}$ in Equation (4.14) denotes the externally applied surface tractions on Γ_f. In the structural equation (4.15) these tractions are neglected. The Lagrange multipliers $\vec{\lambda}$ in Equation (4.14) and (4.15) may be interpreted as the surfaces force exerted on the fluid and structure respectively to ensure coupling as defined by Equation (4.16).

The formulation presented above allows dissimilar and independent discretizations for the fluid and structural domain, which makes the fictitious domain method very appealing for fluid-structure interaction problems involving large structural motions. For the spatial discretization of these equations we adopt the Galerkin finite element method (FEM), which is discussed in De Hart *et al.* (2001a) and Chapter 3 and briefly described in the next section (see Appendix A for more details on the implementation).

4.4 Model properties

The aortic valve consists of three highly flexible leaflets, which are attached to the aortic root from one commissural point along a doubly curved line (aortic ring) towards a second commissural point, as illustrated in Figure 4.1(a) to (c). Behind each leaflet the aortic root bulbs into a sinus cavity to form the beginning of the ascending aorta. Figure 4.2 shows some relevant dimensions that have frequently been used to describe the geometry of the valve. The values of these dimensions (and typical anatomical values measured in human specimens (Thubrikar, 1990; Clark *et al.*, 1974; Sauren, 1981)) are: $r_v = 12.0$ (12.0) [mm], $r_a = 12.0$ (11.4) [mm], $d_s = 5.75$ (5.52) [mm], $h_s = 21.0$ (20.9) [mm], $h_c = 10.5$ (17.5) [mm] and $t_l = 0.20$ (0.20) [mm]. The commissural height h_c used in the model is based on the geometry of synthetic stented prostheses developed by Cacciola (1998).

The valve leaflets constitute a fiber-reinforced composite texture. More precisely,

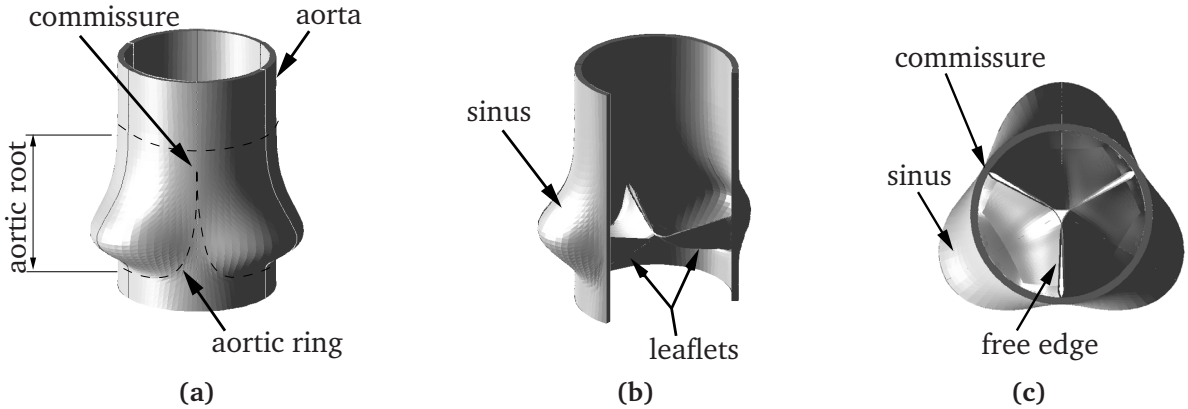

Figure 4.1: *Sketches of the aortic valve: side view of the complete valve (a), after dissection of one leaflet with corresponding sinus wall (b), and top view.*

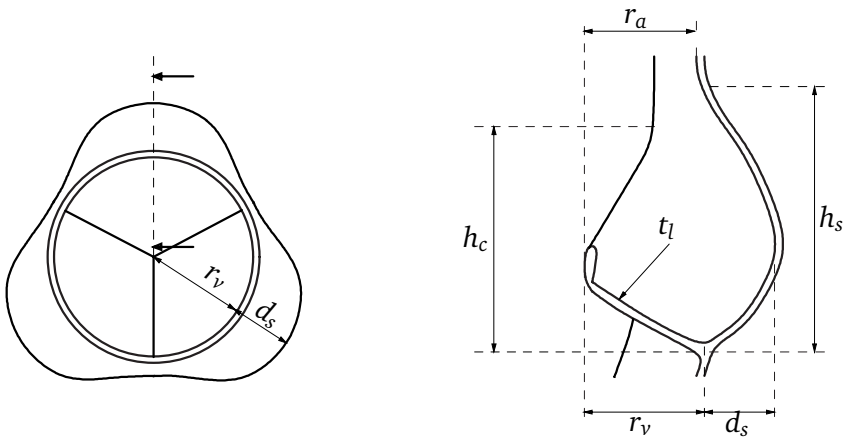

Figure 4.2: *Definition of dimensions, which are used to describe the geometry of the stented aortic valve: r_v denotes the ventricular valve radius, r_a the aortic valve radius, d_s the sinus depth, h_s the sinus height, h_c the commissural height and t_l the leaflet thickness.*

this texture consists of elastin and collagen fibers (mainly concentrated at the aortic leaflet side) embedded in a matrix of endothelial cells. Originating at the commissures collagen fibers run circumferential and spread out over the whole leaflet, see Figure 4.3(a). In addition to these commissural fibers, discrete macroscopically visible bundles, perpendicular to the attachment line, anchor the middle portion of the leaflet to the aortic wall (Sauren, 1981). This collagen leaflet reinforcement is implemented into the model as two distinct layers (Figure 4.3(b)).

The stress-strain relation of the leaflet composite texture has been measured by Sauren (1981) for different human specimens. For the circumferential direction, this relation is given in Figure 4.4 and shows for each leaflet two main phases, which are frequently denoted as the elastin or low strain phase and the collagen or high strain phase. The low strain phase is encountered during initial opening and closing of the valve and is dominated by the characteristics of the elastin fibers in the leaflets. At higher strains, e.g. when the leaflets are pushed towards the sinus cavities during midsystole or the valve has to withstand the diastolic pressure gradient, the collagen fibers dominate the material behaviour of the texture. To simulate this behaviour the matrix shear modu-

Figure 4.3: *Typical fiber structure in the aortic valve leaflets: (a) natural leaflet (from Sauren (1981), with permission), (b) numerical model.*

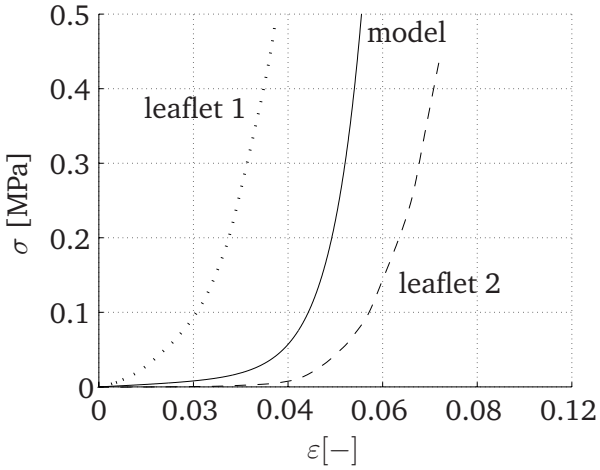

Figure 4.4: *Cauchy stress (σ) versus Green-Lagrange strain (ε) of two different circumferential aortic leaflet specimens reported by Sauren (1981) (dashed and dotted lines). The stress-strain relation in a single fiber direction of the composite used in the numerical model is shown as a solid line.*

lus and fiber parameters in the model composite are chosen such that the low strain phase is determined by the matrix and the high strain phase by the fiber. The resulting stress-strain behaviour is also shown in Figure 4.4 and corresponding parameter values are given in Table 4.1. In this table the low strain modulus in circumferential direction of the human leaflet (Sauren, 1981) and physiological viscosity and density values for human blood (Caro *et al.*, 1978) are presented as well. For the non-reinforced stented model the constitutive behaviour of the complete structural phase is described by (4.8).

Although the three leaflets are not completely identical, it is assumed that they are similar enough to permit a general description of a valve with trileaflet symmetry. Hence, only $\frac{1}{6}$ of the valve will be considered as shown in Figure 4.5. The configuration given in this figure is taken as the initial, stress free condition. The model is bounded in circumferential direction by the symmetry surface, which intersects through half of one leaflet, and by the contact surface, at which two adjacent leaflets come into contact during the closing phase (Figure 4.5(a)). In axial direction the model is bounded by the ventricular (inflow) and aortic (outflow) plane (Figure 4.5(c)), and obviously, in radial direction by the aortic wall, at which homogeneous Dirichlet conditions are applied to

	η_f	ρ_f	G^*	c_1	c_2	θ	N
Dimension	[Pa·s]	[kg/m^3]	[MPa]		[−]		
Model	$3.8{\cdot}10^{-3}$	$1.0{\cdot}10^{3}$	$3.0{\cdot}10^{-2}$	$1.0{\cdot}10^{-3}$	50.0	0.1	2
Human	$3.8{\cdot}10^{-3}$	$1.0{\cdot}10^{3}$	$2.0{\cdot}10^{-2}$	−	−	−	−

Table 4.1: *Material model properties and corresponding physiological values. *The value for G of the human leaflet is measured at low strains and represents the shear modulus in the elastin phase of the leaflet material.*

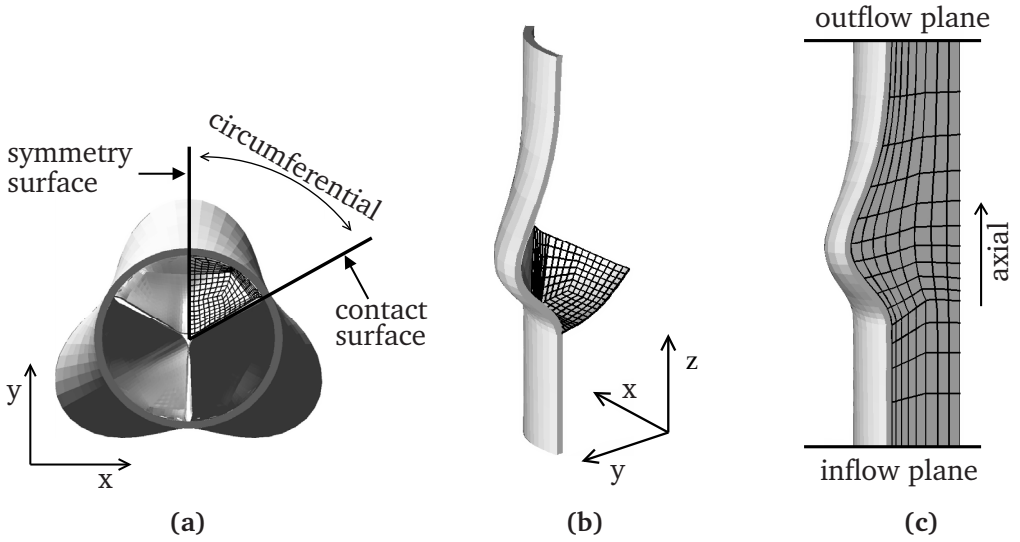

Figure 4.5: *Three-dimensional FEM model of the stented aortic valve: (a) part of the valve used for the computation, (b) structure mesh and (c) fluid mesh.*

fix the leaflet. Moreover, homogeneous Dirichlet conditions are imposed to suppress out of plane motion for the fluid and leaflet at the symmetry surface and for the fluid only at the contact surface. The fluid-structure coupling at the contact surface prevents the leaflet from penetrating this surface for sufficiently small time steps. No-slip conditions are enforced at the fluid-wall surface. Although in reality the valve is positioned right after the left ventricle, the fluid inflow conduct is used here for numerical stability reasons. The model is at the inflow plane fed with a time dependent uniform axial velocity distribution (plug flow) as shown in Figure 4.6. The corresponding maximum flow reaches 230 [ml/s], which is approximately half of the maximum physiological flow. A higher flow would instigate numerical instabilities for the applied mesh resolution described below. However, the shape of the velocity curve is typical for the aortic valve system. The associated Reynolds (*Re*) and Strouhal (*Sr*) number respectively read 1500 and 0.12. At the outflow plane the system is loaded by a physiological aortic pressure curve taken from Van Renterghem (1983) (Figure 4.6). Although for the stented case the leaflet motion is essentially determined by the transvalvular pressure gradient, the absolute pressure is computed here to obtain realistic internal pressures. A cycle independent solution is reached by performing the analysis for two successive cardiac cycles.

The fluid domain is discretized using 650 hexahedral (Crouzeix-Raviart) elements based on the so-called mixed (velocity/pressure) formulation with a quadratic interpolation of the velocity field and a linear interpolation of the pressure field, which is discontinuous throughout the mesh. The discontinuous interpolation for the pressure appears to be mandatory as demonstrated in Baaijens (2001). For the discretization of the structure identical finite elements are used, based here on a displacement/pressure formulation. The Dirichlet conditions applied to the structure are, with this choice of finite elements, imposed over the full leaflet thickness. Given the quadratic interpolation field for the displacement, the bending behaviour of the structure can be modeled using only 1 element across the thickness. However, the element aspect ratio must be

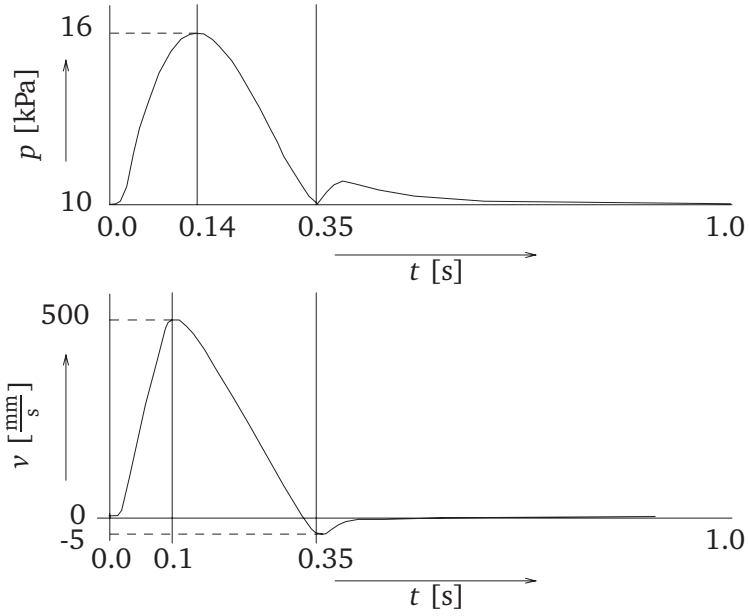

Figure 4.6: *Velocity curve (bottom frame) and aortic pressure curve (top frame) applied to the in- and outflow plane, respectively.*

restricted to achieve a correct bending behaviour. These findings led to a discretization consisting of 210 structural elements.

The Lagrange multipliers are approximated with piecewise constants. Each constant is positioned in the center of a structural element side that coincides with the fluid-structure boundary γ. At these so-called control points Equation (4.13) is enforced locally. This choice requires the leaflet mesh density to be higher than the local fluid mesh density to obtain a satisfying coupling (De Hart *et al.*, 2001a). Many other discretization strategies are possible, however, the above choice is founded on experiences from numerical experiments.

Finally, temporal discretization is achieved using an implicit, backward-Euler scheme which is first-order accurate in time. A time step size of 0.0025 [s] appeared to be sufficiently small for this analysis.

The total system renders a set of non-linear equations, which are linearized using Newton's method (Appendix A). A fully coupled solution strategy is adopted to simultaneously solve the fluid and structure unknowns. Within each time step the Newton-Raphson iterative procedure is applied to ensure convergence for the velocity fields, pressure fields and Lagrange multipliers. At each Newton iteration the set defined by (4.14) to (4.16) is solved with a BiCGStab iterative solver using an ILU preconditioner, which shows satisfying convergence properties due to the applied extra fill-in for the computed lower and upper triangular matrices (Saad, 1996). For more details on the solution strategy the reader is referred to De Hart *et al.* (2001a) and Appendix D.

4.5 Results

The fluid dynamical and structural mechanical performance of the stented valve model is presented in terms of the fluid velocity field, structural displacement field and struc-

tural stresses. With respect to the clinical performance, the transvalvular pressure gradient and blood wash-out during the course of two successive cardiac cycles will be shown.

The velocity vector field is given for the reinforced model only, since the non-reinforced model shows a nearly identical fluid dynamical performance. In Figure 4.7 this vector field is given for 6 successive points in time of the cardiac cycle. For these time points the axial velocity distribution is given at transversal cross-sections taken just upstream of the valve, at the maximum sinus depth, and downstream of the valve. Frame (a) represents the end diastolic situation, i.e. just prior to forward flow. Very little vortical flow is observed in the sinus cavities. Frame (b) represents the configuration just

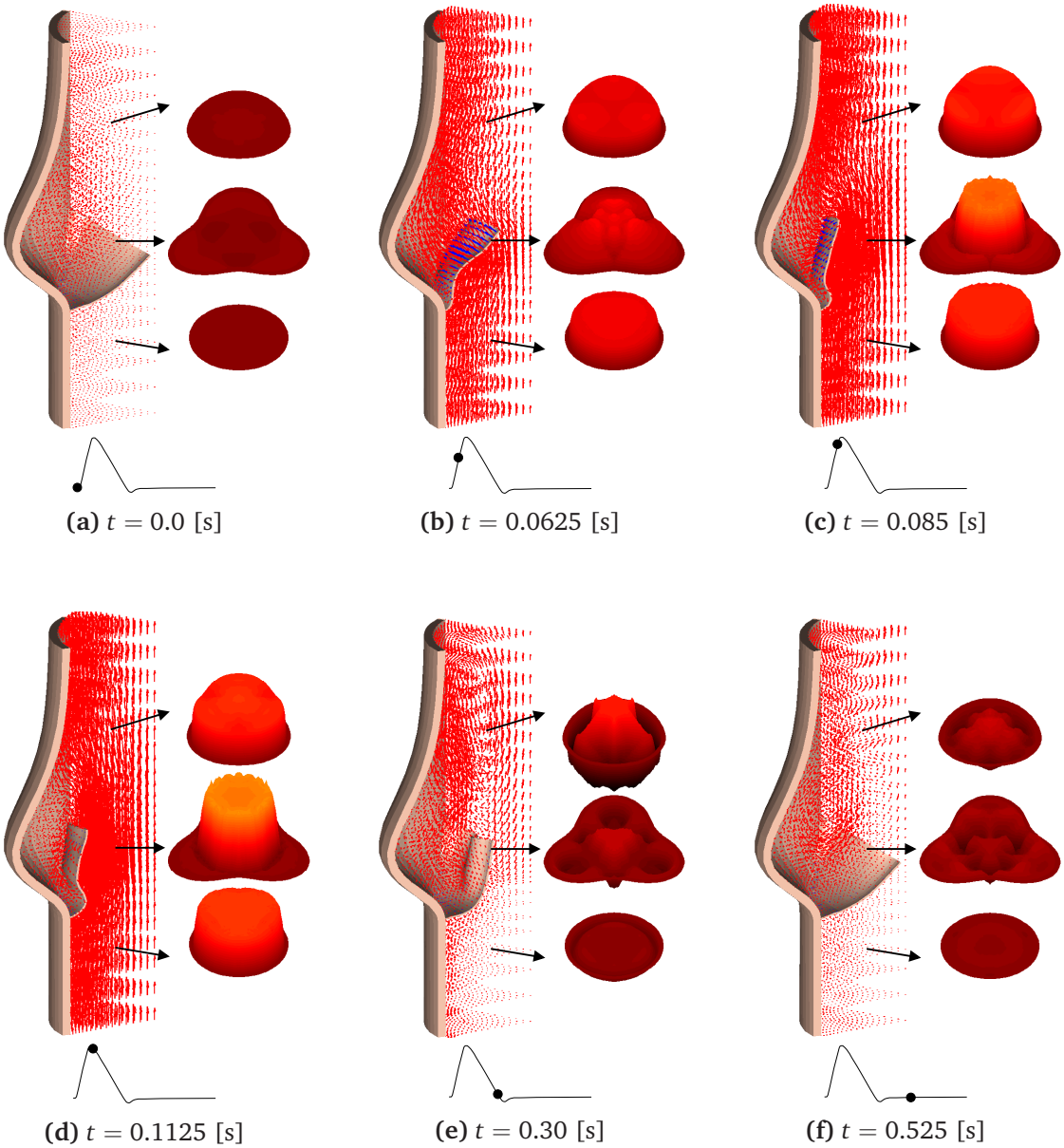

(a) $t = 0.0$ [s] **(b)** $t = 0.0625$ [s] **(c)** $t = 0.085$ [s]

(d) $t = 0.1125$ [s] **(e)** $t = 0.30$ [s] **(f)** $t = 0.525$ [s]

Figure 4.7: *Velocity vector field for 6 successive points in time. The axial velocity distributions are shown at different transversal cross-sections.*

before complete valve opening, which is shown in frame (c). In view of the maximum flow reached with the applied velocity curve (i.e. 230 [ml/s] at the maximum inlet velocity of 500 [mm/s]), the moment of complete opening (85 [ms]) is attained at a later stage in the cardiac cycle when compared with the physiological situation (30-40 [ms], Thubrikar (1990)). This fully open configuration precedes the moment of maximum forward flow (see Figure 4.6), which is also observed for physiological flows (Van Steenhoven *et al.*, 1981) but is different for low flow conditions, as has been demonstrated experimentally by Van Steenhoven *et al.* (1982) and numerically by De Hart *et al.* (2001a) and in Chapter 3. Frame (d) shows the onset of valve closure, at which the maximum velocity is still increasing. At this point vortical flow starts to develop in the ascending aorta, descending towards the sinus cavity as valve closing evolves (frames (e) and (f)).

The mechanical performance of the fiber-reinforced model differs significantly from the non-reinforced model. In Figure 4.8 the different configurations during the systolic phase are shown for the reinforced model (left and top leaflets) and for the non-reinforced model (right leaflet). The maximum principle Cauchy stresses in the matrix material of the fiber-reinforced leaflets are compared with those in the non-reinforced leaflet. Higher stresses and a much more inhomogeneous stress distribution are immediately discernible for the non-reinforced leaflet throughout the systolic phase. The stresses in the fiber-reinforced leaflets are reduced up to 83% (frame (c)) when compared with the non-reinforced leaflet. However, comparison of the stress states per time point is rather awkward for dissimilar reinforced and non-reinforced leaflet configurations. If the maximum stresses attained during the complete systolic phase are compared, a reduction of 63% is obtained.

The reinforced leaflet shows a smooth opening and closing behaviour, whereas the non-reinforced leaflet flutters in the main stream during midsystolic phase (frames (e) to (g)). Leaflet fluttering is accompanied by a cyclic loading pattern, which is believed to stimulate tissue fatigue and ultimately calcification and/or tearing. This phenomenon is much less significantly present in the reinforced leaflets. Another remarkable observation is the difference in closing configurations between the reinforced and non-reinforced valve (frame (g) to (j)). As closing configurations similar to the opening configurations (e.g. frame (b)) are observed for the reinforced valve, the non-reinforced valve shows an opposite deformation pattern near the free edge, which enforces stress reversal during systole.

The contribution of leaflet fiber-reinforcement to stress reduction in the delicate tissue components has been demonstrated numerically by De Hart *et al.* (1998) and Cacciola (1998) in a quasi-static structural analysis of the valve. However, the effect on stresses and valve kinematics during systole has never been investigated before in a fluid-structural dynamical analysis.

The performance of the aortic valve is in clinical practice often evaluated by the transvalvular pressure gradient during opening, which is a measure for the resistance to forward flow. In Figure 4.9 this pressure gradient is given for both the reinforced (solid line) and non-reinforced (dashed line) model and is computed as the difference between the ventricular and aortic pressures taken at 10 [mm] upstream and 35 [mm] downstream the valve (measured from the lowest point of the aortic ring). The mean systolic pressure gradient, i.e. the averaged positive pressure gradient (from A to B in

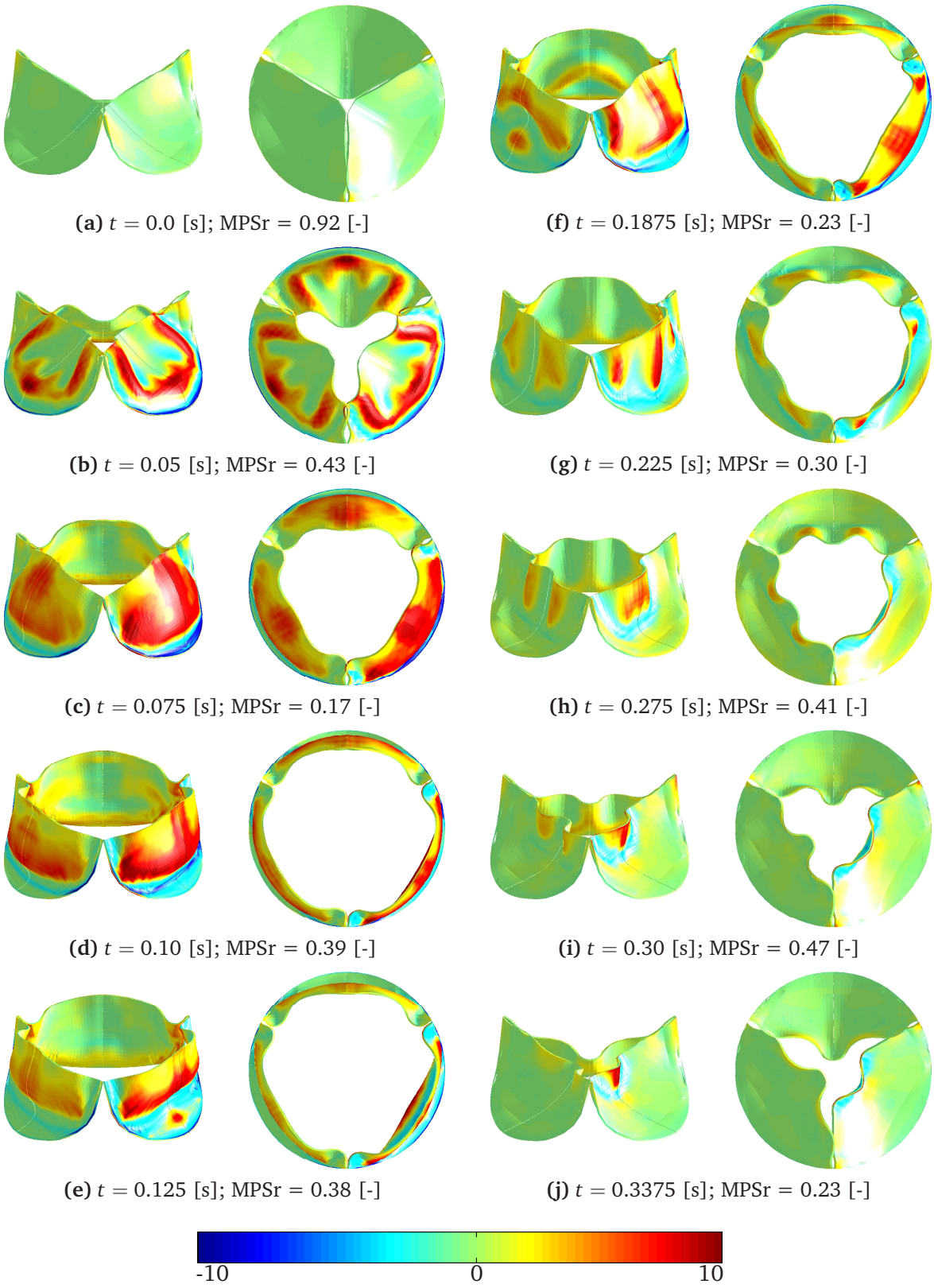

(a) $t = 0.0$ [s]; MPSr = 0.92 [-]
(f) $t = 0.1875$ [s]; MPSr = 0.23 [-]
(b) $t = 0.05$ [s]; MPSr = 0.43 [-]
(g) $t = 0.225$ [s]; MPSr = 0.30 [-]
(c) $t = 0.075$ [s]; MPSr = 0.17 [-]
(h) $t = 0.275$ [s]; MPSr = 0.41 [-]
(d) $t = 0.10$ [s]; MPSr = 0.39 [-]
(i) $t = 0.30$ [s]; MPSr = 0.47 [-]
(e) $t = 0.125$ [s]; MPSr = 0.38 [-]
(j) $t = 0.3375$ [s]; MPSr = 0.23 [-]

Figure 4.8: *Maximum principle Cauchy stresses in the leaflet matrix material during systole. In all frames the right leaflet is taken from the non-reinforced model for comparison. MPSr denotes the maximum principle stress ratio of the reinforced and non-reinforced leaflets. The stress scale on the bottom is given in [kPa].*

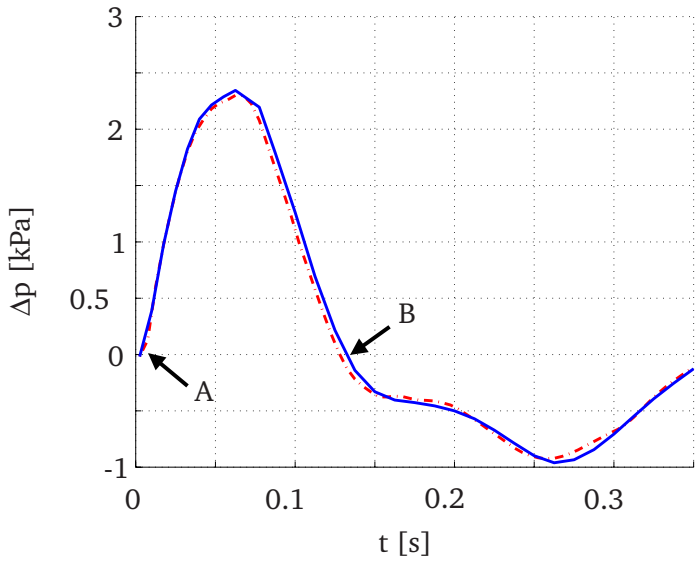

Figure 4.9: *Systolic transvalvular pressure gradient Δp of the fiber-reinforced (solid line) and isotropic (dashed line) stented valve.*

Figure 4.9), reaches a value of 1.46 [kPa] with the obtained maximum flow. In the natural valve, values of 2.0-3.0 [kPa] are most commonly found for maximum flows of 400-500 [ml/s] (Driscol *et al.*, 1965). As the fiber-reinforcement has no significant effect on the fluid dynamics, the pressure drop over the valve is approximately identical to the non-reinforced model. This emphasizes the important role of leaflet fiber-reinforcement during the systolic phase of the cardiac cycle. Fluid dynamical aspects are preserved, whereas the structural mechanical aspects are significantly improved.

Calcification and/or stenosis of the valve leaflets is often accompanied by stagnant flow regions persisting throughout the whole cardiac cycle, which stimulate thrombogenecity. In Figure 4.10 blood wash-out is illustrated during two successive cycles. Frame (a) represents the initial (end diastolic) situation, where fluid particles are positioned upstream the valve and in the sinus cavity. Following these frames from (a) to (f) each particle descends into the aorta within two successive cardiac cycles. Although this is demonstrated for these particular positions, we were unable to find any region for this stented valve design, in which a stagnant flow is present.

4.6 Discussion

The presented stented aortic valve model is based on the Galerkin finite element method and implemented in the SEPRAN software package (Segal, 2000). The key features of this model are: 1. three-dimensionality, 2. fully coupled fluid-structure interaction, 3. avoidance of mesh update strategies, 4. physiological realistic material behaviour and 5. high Reynolds number flow. The systolic phase of the cardiac cycle is analyzed by applying a time-dependent plug flow at the inflow plane and aortic pressure curve at the outflow plane. This choice, however, does not allow for analyses during the dias-

tolic phase, in which the leaflets have to bear the diastolic aortic-ventricular pressure gradient. Imposition of Dirichlet conditions at the inflow plane gives rise to internal diastolic ventricular pressures, which are of the same order as the aortic pressures.

The results presented in this chapter show that the implemented fiber-reinforcement has significant impact on the stress state and kinematics of the leaflets, while the fluid dynamical behaviour is preserved when compared with non-reinforced (isotropic) leaflets. The maximum principle peak stresses in the leaflet matrix material during the systolic phase are reduced with 63%. Similar values have been reported for diastolic loading of the valve by De Hart *et al.* (1998); Cacciola (1998). Moreover, the reinforcement appears to have a stabilizing function for the leaflet kinematics during midsystole. It should be emphasized that the fiber implementation is based on a continuum approximation, yielding that on the element level the fiber contribution is present throughout the complete thickness of the leaflet. In the natural case, the collagen fiber contribution is mainly found at the aortic leaflet surface and, consequently, its impact on kinematical stabilization might therefore be less significant.

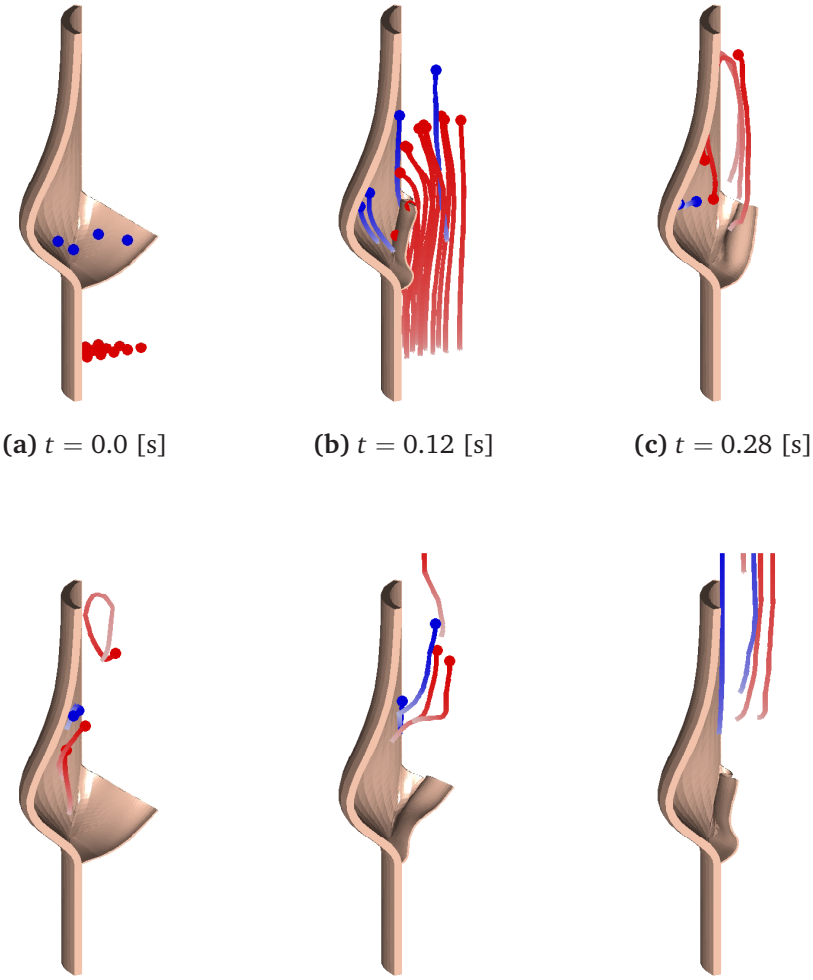

(a) $t = 0.0$ [s] **(b)** $t = 0.12$ [s] **(c)** $t = 0.28$ [s]

(d) $t = 0.55$ [s] **(e)** $t = 1.062$ [s] **(f)** $t = 1.13$ [s]

Figure 4.10: *Particle tracking during two successive cardiac cycles.*

There have been many discussions on the valve closing mechanism in the past (Bellhouse *et al.*, 1969; Van Steenhoven, 1979; Thubrikar, 1990). Our simulation predicts vortical flow in the ascending aorta during flow deceleration, which precedes vortex development in the sinus cavities at end systolic phase. This suggests that vortical flow in the sinus cavity is of less importance for systolic valve closure and that the gradual valve closure is instigated by the (small) pressure difference over the leaflets. Van Steenhoven *et al.* reported on this hypothesis already in 1981 based on *in vivo* cinematographic studies. Although our model predicts a similar closing behaviour, we like to stress that our fluid finite element discretization is chosen from a time efficient point of view. A decrease in mesh size might reveal some deviant fluid dynamical behaviour.

Evaluation of the aortic valve performance is in clinical practice frequently based on pressure drops over the valve. We have shown that the applied fiber-reinforcement has no effect on the value of this measure and that for our model this value is within the physiological range observed in healthy natural valves. Within the context of clinical application, stenotic and/or incompetent valve performance can be studied with respect to the associated medical complications using computational models as presented in this chapter. We intend to report on these findings in terms of e.g. (wall) shear stresses and tissue fatigue behaviour in the near future using patient related data as model parameters.

References

Baaijens, F.P.T., 2001. A fictitious domain/mortar element method for fluid-structure interaction. *International Journal for Numerical Methods in Fluids*, **35**(7): 743-761.

Bathe, K.J, 1982. *Finite Element Procedures in Engineering Analysis*. Prentice-Hall, Inc., New Jersey, USA.

Bellhouse, B.J., Talbot, L., 1969. The fluid mechanics of the aortic valve. *Journal of Fluid Mechanics*, **35**(4): 721-735.

Bernacca, G.M., Mackay, T.G., Wilkinson, R., Wheatly, D.J., 1995. Calcification and fatigue failure in a polyurethane heart valve. *Biomaterials* **16**(4): 279-284.

Bertrand, F., Tanguy, P.A., Thibault, F., 1997. A three-dimensional fictitious domain method for incompressible fluid flow problems. *International Journal for Numerical Methods in Fluids*, **25**(6): 719-736.

Black, M.M., Howard, I.C., Huang, X., Patterson, E.A., 1991. A three-dimensional analysis of a bioprosthetic heart valve. *Journal of Biomechanics*. **24**(9): 793-801.

Cacciola, G., 1998. *Design, Simulation and Manufacturing of Fiber-Reinforced Polymer Heart Valves*. Ph.D. thesis, Eindhoven University of Technology, Eindhoven. *http://www.mate.tue.nl/mate/publications*.

Cacciola, G., De Hart, J., Peters, G.W.M., Schreurs, P.J.G., Baaijens, F.P.T., 1998. A synthetic fibre-reinforced heart valve. *In Proceedings 716 of European Conference on Composite Materials.* Woodhead Publishing Limited, Cambridge, UK.

Caro, C.G., Pedley, J.G., Schroter, R.C., Seed, W.A., 1978. *The Mechanics of the Circulation*. Oxford University Press, Oxford.

Chandran, K.B., Kim, H.H., Han, G., 1991. Stress distribution on the cusps of a polyurethane trileaflet heart valve prosthesis in the closed position. *Journal of Biomechanics*, **24**(6): 385-395.

Clark, R.E., Finke, E.H., 1974. Scanning and light microscopy of human aortic leaflets in stressed and relaxed states. *Journal of Thoracic and Cardiovascular Surgery*, **67**(5): 792-804.

De Hart, J., Cacciola, G., Schreurs, P.J.G., Peters, G.W.M., 1998. A three-dimensional analysis of a fibre-reinforced aortic valve prosthesis. *Journal of Biomechanics*, **31**(7): 629-638.

De Hart, J., Peters, G.W.M., Schreurs, P.J.G., Baaijens, F.P.T., 2000. A two-dimensional fluid-structure interaction model of the aortic valve. *Journal of Biomechanics*, **33**(9): 1079-1088.

De Hart, J., Peters, G.W.M., Schreurs, P.J.G., Baaijens, F.P.T., 2001. A three-dimensional computational analysis of fluid-structure interaction in the aortic heart valve. Submitted to *Journal of Biomechanics*.

Donea, J., Giuliani, S., Halleux, J.P., 1982. An arbitrary Lagrangian-Eulerian finite element method for transient dynamic fluid-structure interactions. *Computer Methods in Applied Mechanics and Engineering*, **33**: 689-723.

Driscol, T.E., Eckstein, R.W., 1965. Systolic pressure gradients across the aortic valve and in the ascending aorta. *American Journal of Physiology*, **209**(3): 557-563.

Fortin, M., Glowinski, R., 1983. *The Augmented Lagrangian method*. North-Holland, Amsterdam.

Glowinski, R., T.-W., Pan, Periaux, J., 1998. Distributed Lagrange multiplier methods for incompressible viscous flow around moving rigid bodies. *Computer Methods in Applied Mechanics and Engineering*, **151**: 181-194.

Johnson, A.A., Tezduyar, T.E., 1994. Mesh update strategies in parallel finite element computations of flow problems with moving boundaries and interfaces. *Computer Methods in Applied Mechanics and Engineering*, **119**: 73-94.

Krucinski, S., Vesely, I., Dokainish, M.A., Campbell, G., 1993. Numerical simulation of leaflet flexure in bioprosthetic valves mounted on rigid and expansile stents. *Journal of Biomechanics*, **26**(8): 929-943.

LeVeque, R.J., Li, Z., 1997. Immersed interface methods for Stokes flow with elastic boundaries or surface tension. *SIAM Journal on Scientific Computing*, **18**(3): 709-735.

Nerem, R.M., Seed, W.A., 1972. An *in vivo* study of aortic flow disturbances. *Cardiovascular Research*, **6**(1): 1-14.

Nomura, T., Hughes, T.J.R., 1991. An arbitrary Lagrangian-Eulerian finite element method for interaction of fluid and a rigid body. *Computer Methods in Applied Mechanics and Engineering*, **95**(1): 115-138.

Patankar, N.A., Singh, P., Joseph, D.D., Glowinski, R., Pan, T.-W., 2000. A new formulation of the distributed Lagrange multiplier/fictitious domain method for particulate flows. *International Journal of Multiphase Flows*, **26**(9): 1509-1524.

Saad, Y., 1996. *Iterative Methods for Sparse Linear Systems*. PWS Publishing Company, Boston.

Sauren, A.A.H.J., 1981. *The Mechanical Behaviour of the Aortic Valve*. Ph.D. thesis, Eindhoven University of Technology, Eindhoven.

Segal, G., 2000. *SEPRAN Introduction, User's Manual, Programmer's Guide and Standard Problems*. Ingenieursbureau SEPRA, Leidschendam.

Singh, P., Joseph, D.D., Helsa, T.I., Glowinski, R., Pan, T.-W., 2000. A distributed Lagrange multiplier/fictitious domain method for viscoelastic particulate flows. *Journal of Non-Newtonian Fluid Mechanics*, **91**: 165-188.

Thubrikar, M., 1990. *The Aortic Valve*. CRC Press, Boca Raton, Florida.

Van Oijen, C.H.G.A., Van de Vosse, F.N., Baaijens, F.P.T., 2002. An updated Lagrange formulation of a constitutive model for incompressible fiber-reinforced materials at finite strains. Submitted to *Computer Methods in Applied Mechanics and Engineering*.

Van Renterghem, R.J., 1983. *Aortic Valve Geometry During the Cardiac Cycle*. Ph.D. thesis, Eindhoven University of Technology, Eindhoven.

Van Steenhoven, A.A., van Dongen, M.E.H., 1979. Model studies of the closing behaviour of the aortic valve. *Journal of Fluid Mechanics*, **90**(1): 21-32.

Van Steenhoven, A.A., Verlaan, C.W.J., Veenstra, P.C., Reneman, R.S., 1981. In-vivo cinematographic analysis of the behaviour of the aortic valve. *American Journal of Physiology*, **240**(2): H286-H292.

Van Steenhoven, A.A., Veenstra, P.C., 1982. The effect of some hemodynamic factors on the behaviour of the aortic valve. *Journal of Biomechanics*, **15**(12): 941-950.

Wheatly, D.J., Fisher, J., Reece, I.J., Spyt, T., Breeze, P., 1987. Primary tissue failure in pericardial heart valves. *Journal of Thoracic and Cardiovascular Surgery* **94**: 367-374.

Chapter 5

Computational Analysis of a Fiber-Reinforced Stentless Aortic Valve[1]

The importance of the aortic root compliance in the aortic valve performance has most frequently been ignored in computational valve modeling, although it has a significant contribution to the functionality of the valve. Aortic root aneurysm or (calcific) stiffening severely affects the aortic valve behaviour and, consequently, the cardiovascular regulation. The compromised valve functioning is difficult to study both 'in vivo' and 'in vitro'. The effect of aortic root compliance on the valve kinematics, mechanics and fluid dynamics during the systolic phase is investigated numerically. To this end a finite element model of a fiber-reinforced stentless aortic valve is developed. In the computational evaluation of its clinical functioning the interaction of the valve with the blood is essential. Hence, the blood-tissue interaction is incorporated in the model using a combined fictitious domain/arbitrary Lagrange-Euler formulation. Results show that aortic root compliance largely influences the valve opening and closing configurations. Stresses in the delicate parts of the leaflets are substantially reduced if fiber-reinforcement is applied and the aortic root is able to expand.

[1]The contents of this chapter are submitted to the *Journal of Biomechanics*, under the title:

A computational fluid-structure interaction analysis of a fiber-reinforced stentless aortic valve
De Hart, J., Baaijens, F.P.T., Peters, G.W.M., Schreurs, P.J.G.

5.1 Introduction

The opening and closing behaviour of the aortic valve is governed by the complex interaction between the valve leaflets, aortic root, blood flow and blood pressures (Thubrikar, 1990). Disfunctioning heart valves compromise cardiovascular regulation and may severely affect quality of life. Stresses in the leaflets and aortic root are believed to be an important measure for the long-term physiological condition of the valve tissue. Fiber-reinforcement of the leaflets and dilation of the aortic root are natural stress reducing mechanisms that enable long-term performance. Pathological changes of the structure may result in abnormal motion and function of the valve. Moreover, blood flow and pressures may significantly become disturbed, resulting in decreasing cardiac output and increasing cardiac work. Thromboembolic complications are known to arise for low blood shear stresses (Nerem *et al.*, 1972), which result from changes in the hemodynamics of the blood. Since stresses are difficult to measure experimentally for transient systems with complex three-dimensional geometries, computational modeling can enhance the understanding of aortic valve behaviour under different physiological conditions.

The clinical performance of a valve is evaluated by both mechanical and hemodynamical characteristics. Hence, the interaction of the valve with the blood is essential when analyzing its functioning. To incorporate fluid-structure interaction we use a combined fictitious domain/arbitrary Lagrange-Euler method, integrated within the classical Galerkin finite element method (FEM). A Lagrange multiplier based fictitious domain method (Baaijens, 2001; De Hart *et al.*, 2001a, and Chapter 3) is used to describe the interaction of the blood flow with the moving leaflets. Fictitious domain methods make fluid mesh update strategies redundant. Instead, dissimilar and independent fluid and structural discretizations are allowed, and thus the fluid mesh is not altered or interrupted by the presence of the valve leaflets. Hence, the different mathematical representations of the fluid and structure balance equations can be maintained, allowing convenient common descriptions for each of these subsystems. In our model, blood-leaflet coupling is realized by a set of kinematical constraints (the no-slip conditions along the leaflet surface), which are enforced through Lagrange multipliers (Bertrand *et al.*, 1997; Glowinski *et al.*, 1998; Patankar *et al.*, 2000).

The dimensions of the aortic root change with the varying internal blood pressures. Consequently, the shape of the fluid domain changes accordingly. Here, the arbitrary Lagrange-Euler (ALE) method (Donea *et al.*, 1982; Johnson *et al.*, 1994; Schreurs, 1983) is adopted to accommodate the fluid domain for aortic root deformation. ALE methods have frequently been used for fluid-structure interaction analyses in vascular systems, see e.g. Perktold *et al.* (1995); Reuderink (1991); Rutten (1998).

In this chapter the mechanical and hemodynamical behaviour of a fiber-reinforced stentless aortic valve model is analyzed. The results are compared to similar non-reinforced models and stented models, which have been presented by De Hart *et al.* (2001b) and in Chapter 4. The physiological condition under which the valve operates, is, within the numerical applicability, adopted to obtain clinical relevance. First, the problem definition and governing equations for the fluid and structure computations are summarized. Next, the coupling between these two phases is briefly described for the combined fictitious domain/arbitrary Lagrange-Euler formulation. The results of

the valve models are presented in terms of structural displacements, stresses, and fluid velocities and wash-out.

5.2 Problem definition and governing equations

Blood is a concentrated suspension of blood cells in plasma. Its rheological behaviour is dominated by the red blood cells. Assuming homogeneity of the concentration a macroscopic continuum model can be used to describe the blood flow. In our model the blood flow is considered to be laminar, isothermal and incompressible. Hence, in absence of body forces and adopting a Newtonian behaviour, the Navier-Stokes equation and the continuity equation, with respect to an Eulerian reference frame, read

$$\rho_f(\frac{\partial \vec{v}_f}{\partial t} + \vec{v}_f \cdot \vec{\nabla}\vec{v}_f) + \vec{\nabla} p_f - 2\eta\vec{\nabla} \cdot \boldsymbol{D}_f = \vec{0}, \tag{5.1}$$

$$\vec{\nabla} \cdot \vec{v}_f = 0, \tag{5.2}$$

where ρ_f denotes the density, t the time, $\vec{v}_f$ is the velocity, p_f the pressure, $\boldsymbol{D}_f$ the rate-of-deformation tensor, η the (constant) dynamic viscosity and $\vec{\nabla}$ the gradient operator. Scaling spatial coordinates with a characteristic length, e.g. the aortic valve radius r_a, velocities with a characteristic velocity, e.g. the peak (inflow) velocity V and time with a characteristic time, e.g. the flow deceleration time τ (measured from maximum flow to the onset of flow reversal), the dimensionless (*) representation of Equation (5.1) is given by

$$Sr\frac{\partial \vec{v}_f^*}{\partial t^*} + \vec{v}_f^* \cdot \vec{\nabla}^*\vec{v}_f^* + \vec{\nabla}^* p^* - \frac{1}{Re}2\vec{\nabla}^* \cdot \boldsymbol{D}_f^* = \vec{0}, \tag{5.3}$$

where the Strouhal number Sr and the Reynolds number Re are defined as

$$Sr = \frac{r_a}{\tau V} \quad ; \qquad Re = \frac{\rho V r_a}{\eta}. \tag{5.4}$$

As fluid and structure density are nearly identical, buoyancy forces can be neglected, and the contribution of the small leaflet mass to the system inertia is assumed to be insignificant. Moreover, the inertia effects resulting from the aortic root and wall are not considered in our model.

The valve leaflets constitute a fiber-reinforced texture. The fiber/matrix structure renders an orthotropic incompressible composite (Sauren, 1981), of which the matrix is assumed to obey a Neo-Hookean material law according to

$$\boldsymbol{\sigma}_m = -p_m\boldsymbol{I} + \boldsymbol{\tau}_m \quad ; \qquad \boldsymbol{\tau}_m = G_m(\boldsymbol{B} - \boldsymbol{I}), \tag{5.5}$$

where $\boldsymbol{\sigma}_m$ is the Cauchy stress tensor, p_m the hydrostatic pressure, $\boldsymbol{I}$ the second-order unit tensor and $\boldsymbol{\tau}_m$ the extra stress tensor of the matrix. The definition of $\boldsymbol{\tau}_m$ represents an isotropic hyperelastic behaviour with G_m the shear modulus and $\boldsymbol{B}$ the Finger or left Cauchy-Green strain tensor. In our model the fibers are described as a one-dimensional material exerting only tensile stress (σ_{fb}) in the fiber direction according to (Van Oijen *et al.*, 2002)

$$\sigma_{fb} = c_1\mu^2\left(e^{c_2(\mu^2-1)} - 1\right) \quad ; \qquad \mu = \|\boldsymbol{F} \cdot \vec{e}_0\|, \tag{5.6}$$

with c_1 and c_2 material constants and μ the fiber stretch, defined in terms of the deformation tensor $\boldsymbol{F}$. The unit vector $\vec{e}_0$ represents the initial local fiber direction. Since $\boldsymbol{F}$ describes the deformation of the composite, matrix and fiber undergo the same deformation. Relation (5.6) is chosen such to represent collagen behaviour for specific choices of the material constants, as will be shown further on for the matrix-fiber composite texture. The constitutive law for the leaflet composite consisting of N fiber layers can now be written as (Van Oijen *et al.*, 2002)

$$\boldsymbol{\sigma}_l = -p_m \boldsymbol{I} + \boldsymbol{\tau}_l \;\; ; \;\; \begin{cases} \boldsymbol{\tau}_l = \boldsymbol{\tau}_m + \sum_{k=1}^{N} \left[\theta_{fb_k} \left(\sigma_{fb_k} - \vec{e}_k \cdot \boldsymbol{\tau}_m \cdot \vec{e}_k\right) \vec{e}_k \vec{e}_k\right], & \mu \geq 1, \\ \boldsymbol{\tau}_l = \boldsymbol{\tau}_m, & \mu < 1 \end{cases} \tag{5.7}$$

with $\vec{e}_k$ the unit vector of the current local fiber direction and θ_{fb_k} the volume fraction of fiber k in the composite. Relation (5.7) is a continuum approximation which states that in the fiber direction $\vec{e}_k$ the fiber stress and extra matrix stress contribute to $\boldsymbol{\tau}_l$ with fractions θ_{fb} and $1 - \theta_{fb}$, respectively.

The aortic root and wall texture contain mainly circumferential arranged smooth muscular tissue embedded in a network of arbitrarily oriented elastin fibers with scattered small collagen fibers (Sauren, 1981). However, an isotropic constitutive behaviour which is approximately linear elastic for the physiological strain range may be expected (Thubrikar, 1990). Therefore, a Neo-Hookean material law similar to Equation (5.5) is adopted, using wall shear modulus G_w and hydrostatic pressure p_w.

In absence of body forces, the structure balance equations can now be written as:

$$\vec{\nabla} \cdot \boldsymbol{\sigma}_s = \vec{0}, \tag{5.8}$$

$$\det(\boldsymbol{F}) = 1 \tag{5.9}$$

where the subscript 's' has been introduced to represent the general structure, i.e. leaflet or wall. Equations (5.8) and (5.9) are described using an updated Lagrange formulation. In this formulation it is customary to take the displacement field $\vec{u}_s$ during a time step $t^n \rightarrow t^{n+1}$ as the unknown. For the interaction with the fluid, the structural velocity field is considered rather than the displacement field. To this end a first-order approximation for the velocity field is used:

$$\vec{v}_s = \frac{\vec{u}_s}{\Delta t} \tag{5.10}$$

where time step $\Delta t = t^{n+1} - t^n$.

5.3 Fluid-structure interaction

Fluid-structure interaction in the aortic valve involves a coupling of the fluid domain (blood) with immersed structures, i.e. the valve leaflets, and bounding structures, i.e. the aortic root and wall, as sketched in Figure 5.1. This coupling is straightforward if equal-order discretization of the fluid and structural domain is used and nodes and element boundaries coincide along the fluid-structure interface. However, in (5.1) and

(5.2) the fluid domain is fixed in space, while in (5.8) and (5.9) the position of the structural domain is moving and not known *a priori*. Consequently, continuously updating the fluid mesh to accommodate for the motion of the structural domain requires remeshing or alternatively, an arbitrary Lagrange-Euler (ALE) formulation for the fluid domain. The change in mesh topology during remeshing introduces artificial diffusivity as state variables must be interpolated to the newly generated mesh. Moreover, this technique is difficult and/or time-consuming to perform with sufficient robustness and accuracy for three-dimensional problems. The ALE formulation is restricted to applications where the motion of the structural domain is such that the accommodated fluid mesh preserves a proper quality, as is the case for interaction with the aortic root and wall. This approach is, however, not applicable for interaction with the valve leaflet, which shows large deformations (Baaijens, 2001). Instead, a fictitious domain formulation is used to circumvent fluid mesh updating according to the leaflet motion. The mathematical formulation describing the interaction of the leaflets with the fluid is elaborated in De Hart *et al.* (2001a) and summarized here.

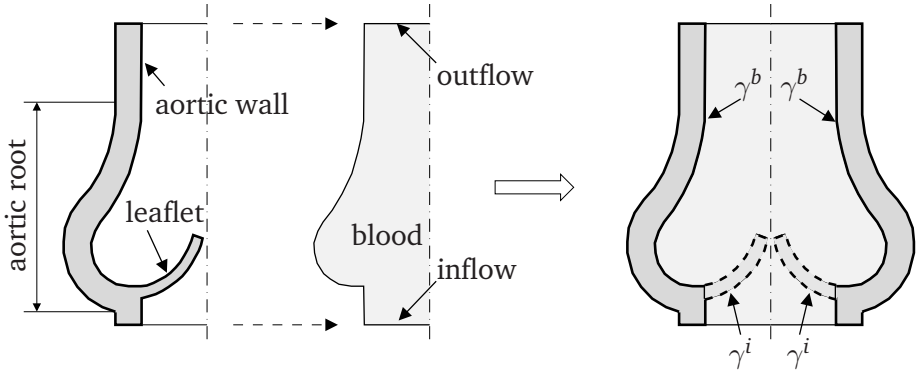

Figure 5.1: *Composition sketch of the aortic valve. The boundaries γ^b and γ^i denote the fluid-structure interface at the bounding aortic wall and immersed leaflets, respectively.*

To distinct between the immersed and bounding interface we define the fluid-structure boundary $\gamma = \gamma^i \cup \gamma^b$ (Figure 5.1). Physically, the immersed leaflets and fluid cannot occupy the same domain in space. The basic idea of fictitious domain formulations is to mathematically rewrite the problem defined on the fluid domain as a problem defined on an extended fluid domain containing the immersed structure. To describe the presence of the immersed structure for this new problem we introduce kinematical (no-slip) constraints defined by

$$\vec{v}_f - \vec{v}_s = \vec{0}, \tag{5.11}$$

along the fluid-structure boundary γ^i. For the aortic valve leaflets these coupling constraints can be enforced along one side of the leaflet only, since their thickness is negligible as far as the interaction with the fluid is considered. The key feature of the fictitious domain approach is that these constraints may be enforced weakly and hence allow dissimilar and independent discretizations for the fluid and leaflet mesh, which makes the method very appealing for fluid-structure interaction problems involving large structural motions. In our model, the coupling constraints are weakly enforced using Lagrange multipliers $\vec{\lambda}$ (Fortin *et al.*, 1983; Bathe, 1982)(Appendix B).

In the interaction of the fluid with bounding structures the fluid mesh is neither fixed to the fluid domain nor fixed in space (ALE description). To this end we introduce a moving computational fluid grid, which completely covers the fluid domain. At the fluid-structure interface γ_b the grid displacement field is taken to be identical to the structural displacement field. As fluid elements along γ_b may become distorted by this deformation the complete fluid grid is aligned to the change in boundary shape in order to preserve a proper mesh quality. This results in a grid displacement field $\vec{u}_g$ which is arbitrary (except at the boundaries) and defined for numerical purposes only. Within the class of ALE procedures, the methods differ in their way of controlling this grid displacement field. Here, the moving grid is considered to be a (pseudo-)structure defined by an isotropic, linear elastic material law to which the structural displacements at γ_b are applied as Dirichlet conditions (Johnson *et al.*, 1994; Nomura *et al.*, 1991). Having no physical relevance the actual pseudo-structural material parameters can be chosen arbitrarily. The associated grid velocity vector $\vec{v}_g$ is defined by the first-order approximation

$$\vec{v}_g = \frac{(\vec{u}_g^{\,n+1} - \vec{u}_g^{\,n})}{\Delta t}. \tag{5.12}$$

Then, elaboration of the spatial derivative in the Navier-Stokes equation defined on a moving grid (Donea *et al.*, 1982) yields

$$\rho_f \left(\frac{\partial \vec{v}_f}{\partial t} + (\vec{v}_f - \vec{v}_g) \cdot \vec{\nabla} \vec{v}_f \right) + \vec{\nabla} p_f - \vec{\nabla} \cdot 2\eta \boldsymbol{D}_f = \vec{0}, \tag{5.13}$$

which is derived in Appendix C.

Depending on the fluid and structure discretizations along γ^b, the coupling constraint similar to (5.11) can be enforced weakly (unequal discretizations at γ^b) using Lagrange multipliers $\vec{\lambda}$ or strongly (equal discretizations at γ^b) avoiding the introduction of $\vec{\lambda}$. The latter is adopted in this work to describe the interaction at the aortic root and wall.

Using Ω_g and Ω_s to define the (moving) fluid and structural computational domains, and Γ_g and Γ_s the associated boundaries, the weak formulation describing the total system reads

$$\begin{aligned}
&\int_{\Omega_g} \vec{w}_f \cdot \left(\rho_f \frac{\partial \vec{v}_f}{\partial t} + \rho_f (\vec{v}_f - \vec{v}_g) \cdot \vec{\nabla} \vec{v}_f \right) d\Omega_g + \int_{\Omega_g} (\vec{\nabla} \vec{w}_f)^T : 2\eta \boldsymbol{D}_f \, d\Omega_g - \\
&\qquad \int_{\Omega_g} (\vec{\nabla} \cdot \vec{w}_f) p_f \, d\Omega_g + \int_{\gamma^i} \vec{w}_f \cdot \vec{\lambda} \, d\gamma^i = \int_{\Gamma_g} \vec{w}_f \cdot \vec{t}_f \, d\Gamma_g, \qquad (5.14) \\
&\int_{\Omega_g} q_f (\vec{\nabla} \cdot \vec{v}_f) \, d\Omega_g = 0, \\
&\int_{\Omega_s} (\vec{\nabla} \vec{w}_s)^T : \boldsymbol{\tau}_s \, d\Omega_s - \int_{\Omega_s} (\vec{\nabla} \cdot \vec{w}_s) p_s \, d\Omega_s - \int_{\gamma^i} \vec{w}_s \cdot \vec{\lambda} \, d\gamma^i = 0, \\
&\int_{\Omega_s} q_s \left(\det(\boldsymbol{F}) - 1 \right) d\Omega_s = 0, \qquad (5.15) \\
&\int_{\gamma^i} \vec{\ell} \cdot (\vec{v}_f - \vec{v}_s) \, d\gamma^i = 0, \qquad (5.16)
\end{aligned}$$

which must hold for all admissible weighting functions $\vec{w}_f, q_f, \vec{w}_s, q_s$ and $\vec{\ell}$. The surface tractions $\vec{t}_f = (-p_f \boldsymbol{I} + 2\eta \boldsymbol{D}_f)\cdot\vec{n}$ in Equation (5.14) are prescribed at the outflow boundary and represent the aortic pressure applied to the models. The Lagrange multipliers $\vec{\lambda}$ in Equation (5.14) and (5.15) may be interpreted as the surfaces force exerted on the fluid and structure respectively to ensure coupling as defined by Equation (5.16). For the spatial discretization of these equations we adopt the Galerkin finite element method (FEM), which is discussed in De Hart *et al.* (2001a) and briefly described in the next section (see Appendix A for more details on the implementation).

5.4 Model properties

The aortic valve consists of three highly flexible leaflets, which are attached to the aortic root from one commissural point along a doubly curved line (aortic ring) towards a second commissural point, as illustrated in Figure 5.2(a) to (c). Behind each leaflet the aortic root bulbs into a sinus cavity to form the beginning of the ascending aorta. Figure 5.3 shows some relevant dimensions that have frequently been used to describe the geometry of the valve. The values of these dimensions used in the model and typical anatomical values measured in human specimens (Thubrikar, 1990; Clark *et al.*, 1974; Sauren, 1981) are summarized in Table 5.1.

The valve leaflets constitute a fiber-reinforced composite texture. More precisely, this texture consists of elastin and collagen fibers (mainly concentrated at the aortic leaflet side) embedded in a matrix of endothelial cells. Originating at the commissures, collagen fibers run circumferential and spread out over the whole leaflet, see Figure 5.4(a). In addition, discrete macroscopically visible bundles, perpendicular to the attachment line, anchor the middle portion of the leaflet to the aortic root (Sauren, 1981). This fiber-reinforcement is implemented into the model as two distinct layers (Figure 5.4(b)).

The stress-strain relation of the leaflet composite texture in humans has been measured by Sauren (1981). For two different specimens this relation in circumferential

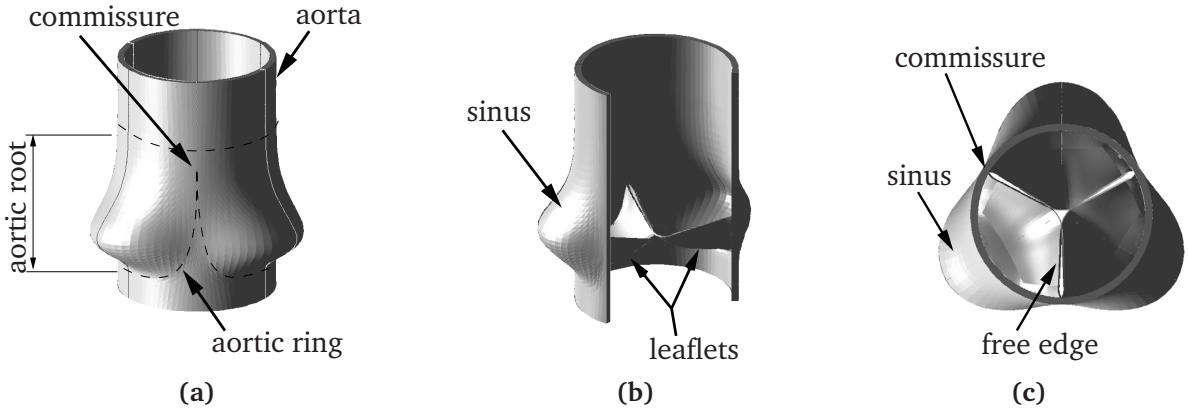

Figure 5.2: *Sketches of the aortic valve: side view of the complete valve (a), after dissection of one leaflet with corresponding sinus wall (b), and top view.*

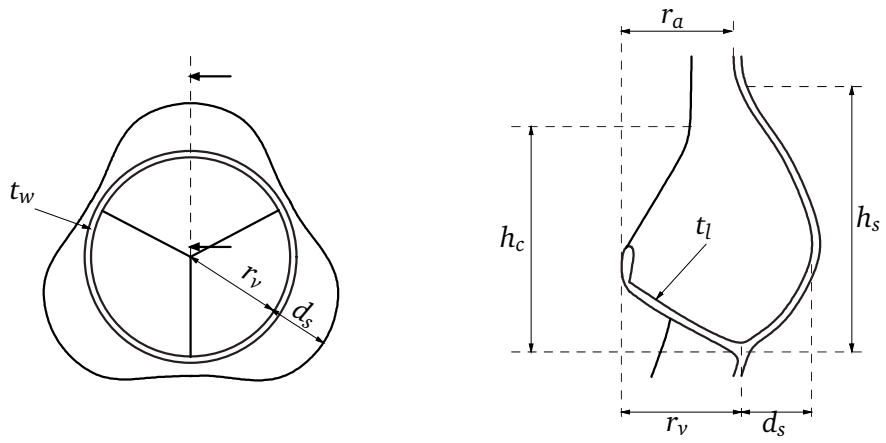

Figure 5.3: *Definition of dimensions, which are used to describe the geometry of the stentless aortic valve: r_v denotes the ventricular valve radius, r_a the aortic valve radius, d_s the sinus depth, h_s the sinus height, h_c the commissural height, t_l the leaflet thickness and t_w the aortic root/wall thickness.*

direction is given in Figure 5.5 and shows for each leaflet two main phases, which are frequently denoted as the elastin or low strain phase and the collagen or high strain phase. The low strain phase is encountered during the opening and closing of the valve and is dominated by the characteristics of the elastin fibers in the leaflets. At higher strains, e.g. when the leaflets are pushed towards the sinus cavities during midsystole or the valve has to withstand the diastolic pressure gradient, the collagen fibers dominate the material behaviour of the texture. To simulate this matrix-fiber behaviour the matrix shear modulus and fiber parameters in the model composite are chosen such that the low strain phase is determined by the matrix and the high strain phase by the fiber. The resulting stress-strain behaviour is also shown in Figure 5.5. This behaviour is in our models generalized to hold for both implemented fiber layers. Corresponding parameter values as well as the parameter values describing the wall and blood are given in Table 5.2. In this table the leaflet low strain modulus in circumferential direction (Sauren, 1981), the aortic root/wall shear modulus (Sauren, 1981) and physiological blood viscosity and density (Caro *et al.*, 1978), measured in humans, are also presented.

Although the three leaflets are not completely identical, it is assumed that they are similar enough to permit a general description of a valve with trileaflet symmetry. Hence, only $\frac{1}{6}$ of the valve will be considered as shown in Figure 5.6. The configuration given in this figure is taken as the initial, stress free condition. The model is bounded

	r_v	r_a	d_s	h_s	h_c^*	t_l	t_w
Model [mm]	12.0	12.0	5.75	21.0	10.5	0.20	1.00
Human [mm]	12.0	11.4	5.52	20.9	17.5	0.20	1.03

Table 5.1: *Geometrical model properties and corresponding anatomical values. *The commissural height h_c used in the model is based on the geometry of the synthetic fiber-reinforced prostheses presented in Cacciola (1998) and De Hart et al. (1998).*

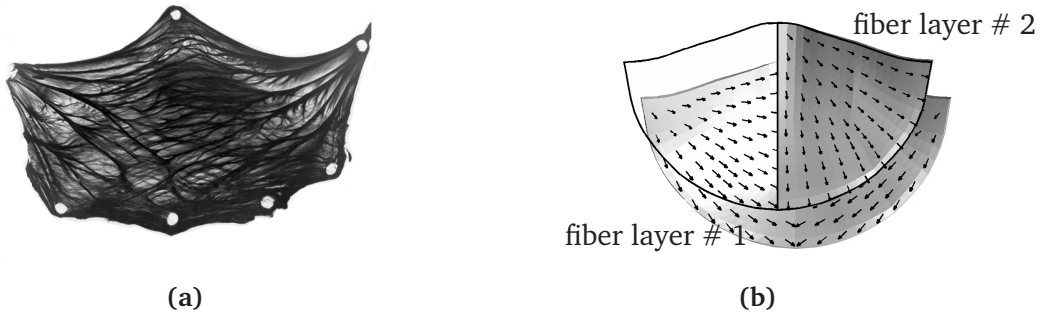

Figure 5.4: *Typical fiber structure in the aortic valve leaflets: (a) natural leaflet (from Sauren (1981), with permission), (b) numerical model.*

in circumferential direction by the symmetry surface, which intersects through half of one leaflet, and by the contact surface, at which two adjacent leaflets come into contact during the closing phase (Figure 5.6(a)). In axial direction the model is bounded by the ventricular (inflow) and aortic (outflow) plane (Figure 5.6(c)), and obviously, in radial direction by the aortic root/wall.

Homogeneous Dirichlet conditions are imposed to suppress out of plane motion for the fluid, wall and leaflet at the symmetry surface and for the fluid and wall only at the contact surface. Fluid-structure coupling at the contact surface prevents the leaflet from penetrating this surface for sufficiently small time steps. The leaflet is fixed to the aortic wall at the ventricular surface using a discretization, which is taken identical to the local wall discretization. The aortic wall is fixed at the outflow plane (25 [mm] downstream the valve, measured from the commissural point) and at the inflow plane (15 [mm] upstream the valve, measured from the lowest point of the aortic ring). Although in reality the valve is positioned right after the left ventricle, the fluid inflow conduct is used here for numerical stability reasons.

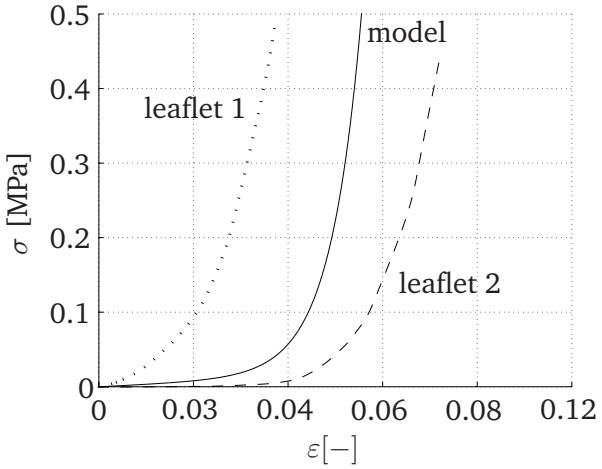

Figure 5.5: *Cauchy stress (σ) versus Green-Lagrange strain (ε) of two different circumferential aortic leaflet specimens reported by Sauren (1981) (dashed and dotted lines). The stress-strain relation in a single fiber direction of the composite used in the numerical model is shown as a solid line.*

Dimension	η_f [Pa·s]	ρ_f [kg/m^3]	G_w	G_l^*	c_1	c_2	θ	N
			[MPa]			[−]		
Model	$3.8{\cdot}10^{-3}$	$1.0{\cdot}10^{3}$	0.5	$3.0{\cdot}10^{-2}$	$1.0{\cdot}10^{-3}$	50.0	0.1	2
Human	$3.8{\cdot}10^{-3}$	$1.0{\cdot}10^{3}$	0.3	$2.0{\cdot}10^{-2}$	–	–	–	–

Table 5.2: *Material model properties and corresponding physiological values. *The value for G_l of the human leaflet is measured at low strains and represents the shear modulus in the elastin phase of the leaflet material.*

The model is fed with a plug flow at the inflow plane (Figure 5.7). The corresponding maximum flow reaches 230 [ml/s], which is approximately half of the maximum physiological flow. A higher flow would instigate numerical instabilities for the applied mesh resolution described below. However, the shape of the velocity curve is typical for the aortic valve system (Thubrikar, 1990). The associated Reynolds (*Re*) and Strouhal (*Sr*) number respectively read 1500 and 0.12. At the outflow plane the aortic pressure is applied, which is taken from Van Renterghem (1983).

The aortic root and wall configuration as shown in Figure 5.6 is taken to be the initial, stress free configuration. It is assumed that this configuration corresponds to the physiological end diastolic situation at which the root and wall have to withstand internal blood pressures of 10 [kPa]. Hence, only 6 [kPa] is applied at the outflow plane to simulate an aortic root and wall motion, which corresponds to a maximum physiological systolic loading of 16 [kPa]. The analysis is performed for two successive cardiac cycles to obtain a cycle independent solution.

The fluid domain is discretized using 650 hexahedral (Crouzeix-Raviart) elements based on the so-called mixed (velocity/pressure) formulation with a quadratic inter-

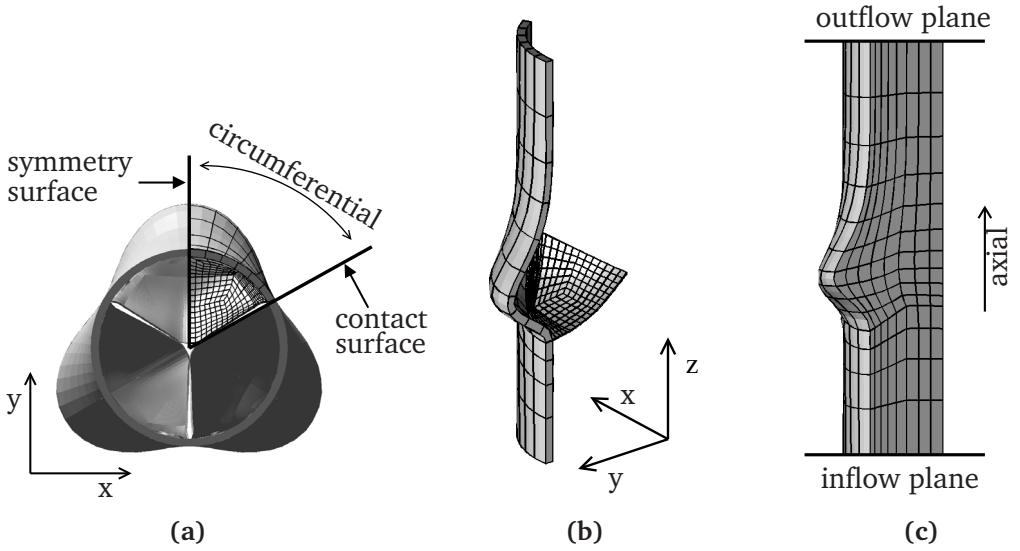

Figure 5.6: *Three-dimensional FEM model of the stentless aortic valve: (a) part of the valve used for the computation, (b) structure mesh and (c) fluid mesh.*

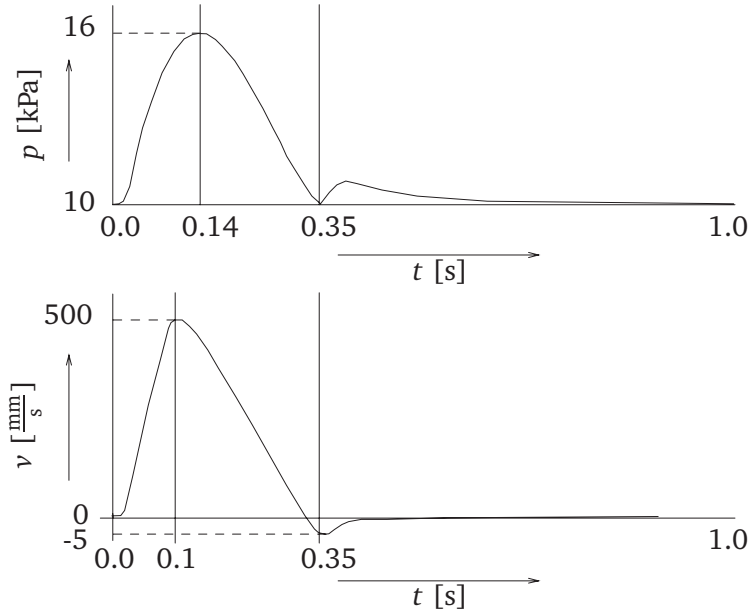

Figure 5.7: *Velocity curve (bottom frame) and aortic pressure curve (top frame) applied to the in- and outflow plane, respectively.*

polation of the velocity field and a linear interpolation of the pressure field which is discontinuous throughout the mesh. The discontinuous interpolation for the pressures appears to be mandatory as demonstrated by Baaijens (2001). Identical finite elements are used to discretize the structural domain, however, based on a displacement/pressure formulation. The Dirichlet conditions applied to the structure at the symmetry surface are, with this choice of finite elements, imposed over the full leaflet thickness. Given the quadratic interpolation field for the displacement the bending behaviour of the structure can be modeled using only 1 element across the thickness. However, the element aspect ratio must be restricted to achieve a correct bending behaviour. These findings led to a discretization of the wall and leaflet consisting of 105 and 210 elements, respectively.

The Lagrange multipliers are approximated with piecewise constants. Each constant is positioned in the center of a structural element side that coincides with the fluid-structure boundary γ^i. At these so-called control points Equation (5.11) is enforced locally. This choice requires the leaflet mesh density to be higher than the local fluid mesh density to obtain a satisfying coupling. Many other discretization strategies are possible, however, the above choice is founded on experiences from numerical experiments.

Finally, temporal discretization is achieved using an implicit backward-Euler scheme which is first-order accurate in time. An adaptive time step algorithm is used for the first part of the systolic phase, which led to a minimum time step size of 0.00125 [s] required for only a few discreet time points. A time step size of 0.0025 [s] appeared to be sufficiently small for the remaining part of the systolic phase.

The total system renders a set of non-linear equations, which are linearized using Newton's method (Appendix A). The adopted solution strategy combines a fully coupled approach to solve the fluid and structure unknowns and a weakly coupled approach to incorporate the fluid mesh deformation associated with the moving aortic root and wall (Appendix D). Within each time step the Newton-Raphson iterative procedure is

applied to ensure equilibrium for the velocity fields, pressure fields and Lagrange multipliers. At each iteration the equations defined by (5.14), (5.15) and (5.16) are solved simultaneously with the BiCGStab iterative solver using an ILU preconditioning, which shows satisfying convergence properties due to the extra fill-in of the computed lower and upper triangular matrices (Saad, 1996). If convergence is achieved for this set of equations the structural displacements at the aortic root/wall are applied to the pseudo-structural problem defined on the moving fluid grid. A grid displacement and velocity field for the fluid domain is computed and the fluid mesh is updated accordingly. From this point the computational analysis proceeds to the next time step.

5.5 Results

We want to make a comparison between the results of the fiber-reinforced and non-reinforced stentless valves as well as between these results and the results of the stented valves reported by De Hart *et al.* (2001b) and in Chapter 4. A selection of representative mechanical and fluid dynamical aspects will be given.

To visualize the delicate interaction between the pliable leaflets, compliant aortic root and the blood, a general assessment of the model is shown in Figure 5.8. In this figure, 6 successive configurations of the reinforced valve with corresponding fluid velocity vector field are given. The opening (frames (a) to (c)) is typical for stentless valves (Cacciola, 1998) and is approximately identical for reinforced and non-reinforced leaflets as will be shown further on. The commissural points move outward in response to rising internal blood pressures pulling the leaflets towards the sinus cavities. This mechanism is essential for stentless valve opening, while the contribution of blood-leaflet interaction is of minor importance during the first part of the opening phase. In fact, numerical tests have shown that if fluid-structure interaction of the leaflets is completely ignored this commissural motion would result in approximately 80% opening of this valve design. In the last part of the opening phase the leaflets are pushed further into the sinus cavities driven by the blood flow. The opening configurations differ significantly from the stented types (De Hart *et al.*, 2001b, and Chapter 4) in that the free edges are much less subjected to bending. Frame (d) shows a valve configuration associated with the first part of the closing phase. At this stage the maximum velocity is reached, while the net forward flow is already decreasing. During this stage the commissural points move inwards following the decreasing aortic pressure curve (Figure 5.7). Frames (e) and (f) cover the last part of the closing phase.

The fluid dynamical phenomena are visualized better in Figure 5.9. In this figure the non-reinforced model is considered, since the reinforced model shows vortex orientations, which are difficult to capture in a three-dimensional representation. Frames (a) to (c) represent the acceleration phase of the flow. Just prior to forward flow very little vorticity is observed in the sinus cavity (frame (a)). In frame (b) the aortic root dilates as it has to carry the increasing internal blood pressure. Consequently the volume, captured by the aortic root, increases and is filled by the inflowing blood. Hence, the blood flow through the valve exceeds the blood flow into the ascending aorta. A completely opened configuration is attained in frame (c) and precedes the moment of maximum forward flow reached at $t = 0.1$ [s]. This is also observed in stented models (De Hart *et al.*, 2001b, and Chapter 4) and has been reported for physiological flows

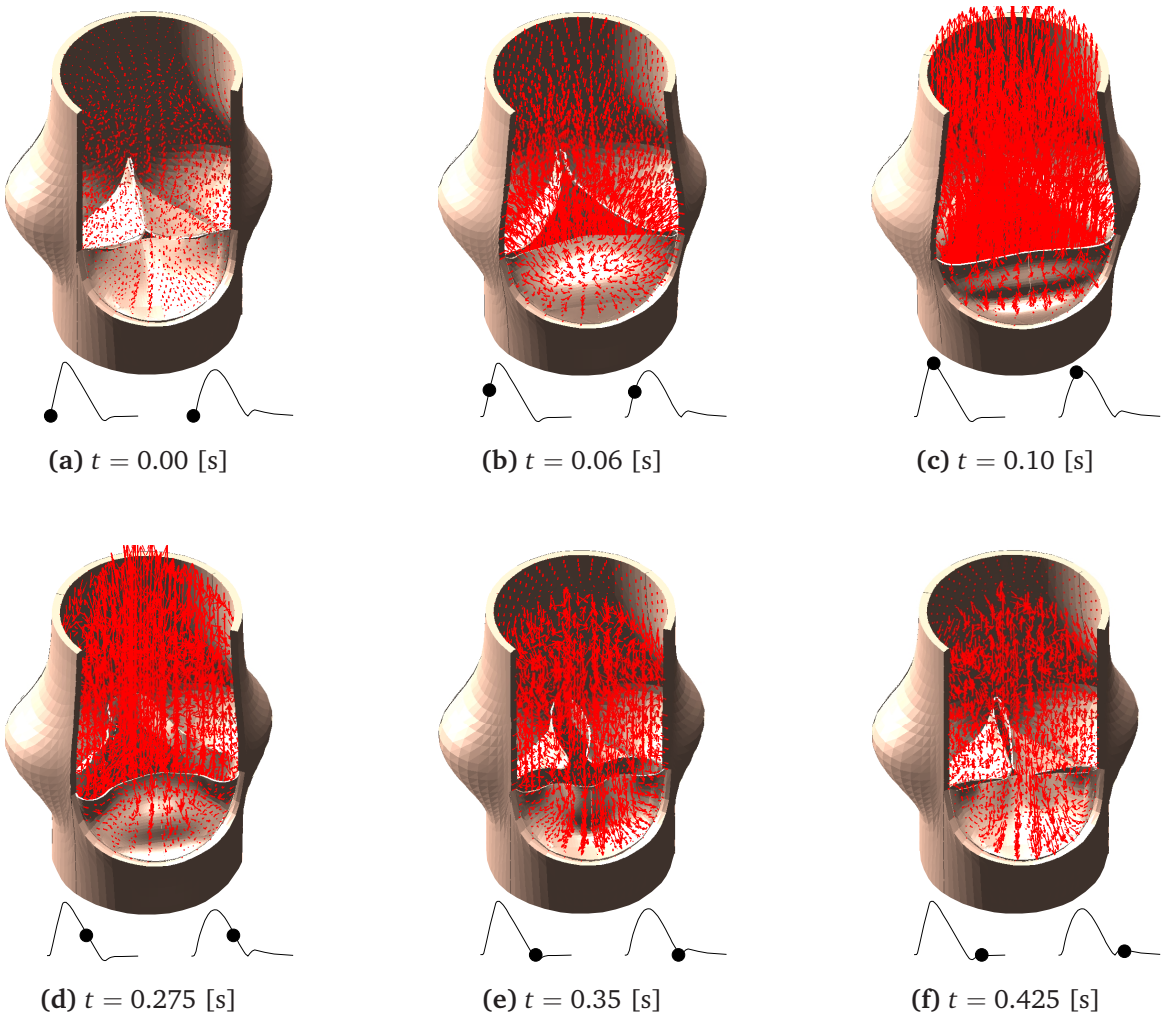

(a) $t = 0.00$ [s] **(b)** $t = 0.06$ [s] **(c)** $t = 0.10$ [s]

(d) $t = 0.275$ [s] **(e)** $t = 0.35$ [s] **(f)** $t = 0.425$ [s]

Figure 5.8: *Configurations of the fiber-reinforced stentless valve and corresponding velocity vector fields taken at 6 successive points in time. The left and right diagram at the bottom of each frame denote the applied velocity and pressure curves, respectively.*

by Van Steenhoven *et al.* (1981) in an *in vivo* cinematographic study of the aortic valve. As the flow starts to decelerate a vortex develops behind the leaflet free edge (frame (d)) descending into the aorta (frame (e)). This vortex is basically oriented in the symmetry plane. In the fiber-reinforced model the vortex tends to align with the leaflet free edge and, therefore, is difficult to visualize in a three-dimensional representation. Subsequently, an increasing back flow along the wall initiates flow into the sinus cavity (frame (f)) developing a large vortex in the sinus and pushing the leaflet towards a closed configuration (frame (g) and (h)). Similar results have been reported by Yang *et al.* (1998) in natural valves using MR imaging techniques. The strong back flow at the aortic wall also initiates a small secondary vortex in the area of maximum sinus depth.

The impact of fiber-reinforcement on the mechanical performance is illustrated in Figure 5.10. The stress state associated with 8 successive valve configurations are given. In the right figure of each frame (top view) the aortic root is dissected from the transversal cross-sectional plane at maximum sinus depth to the outflow plane, so that the stress state of the inner sinus wall becomes visible. The maximum principle Cauchy stresses

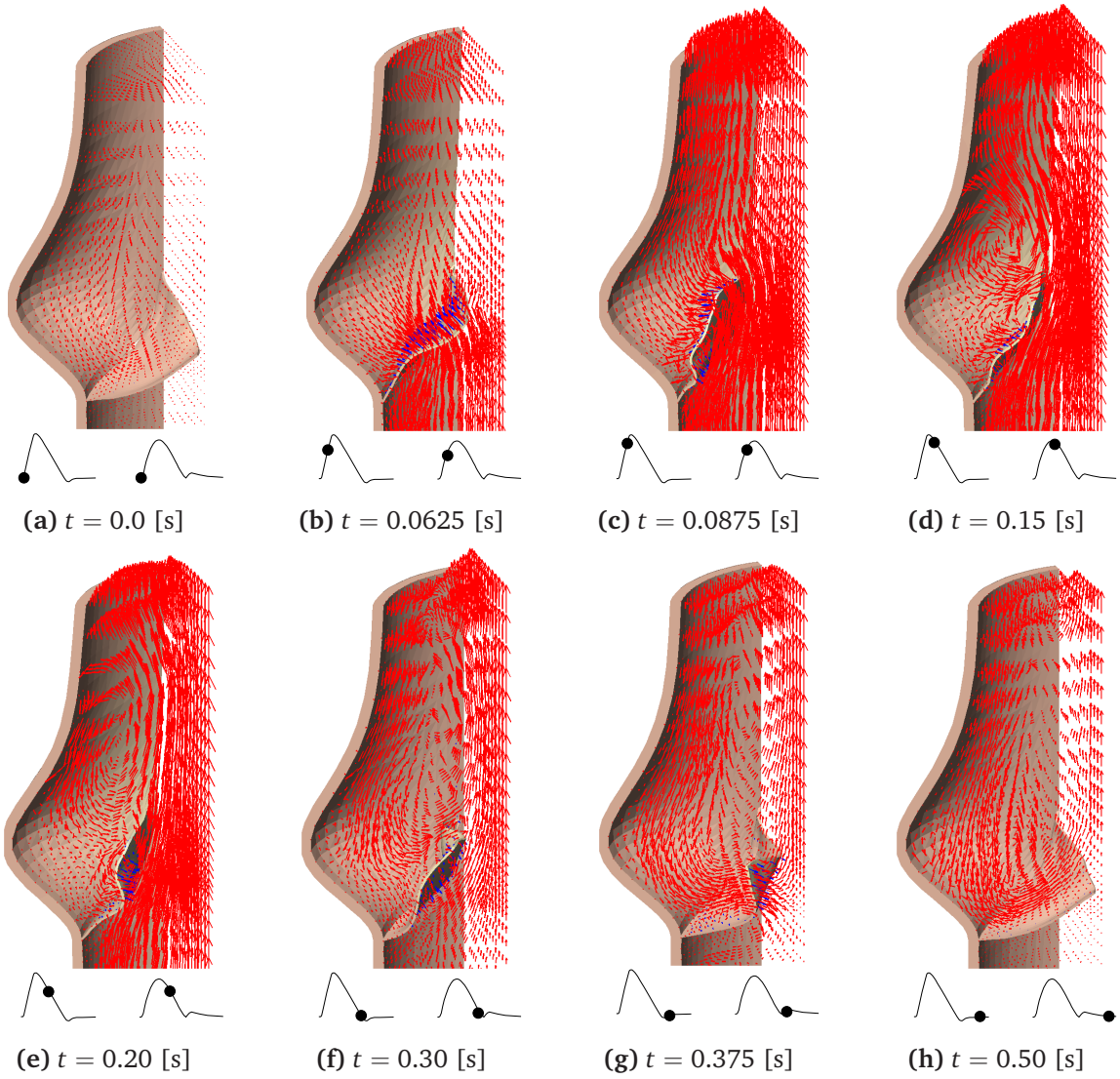

(a) $t = 0.0$ [s] **(b)** $t = 0.0625$ [s] **(c)** $t = 0.0875$ [s] **(d)** $t = 0.15$ [s]

(e) $t = 0.20$ [s] **(f)** $t = 0.30$ [s] **(g)** $t = 0.375$ [s] **(h)** $t = 0.50$ [s]

Figure 5.9: *Fluid dynamics during systole of the non-reinforced model. The left and right diagram at the bottom of each frame denote the applied velocity and pressure curves, respectively.*

are given for the matrix material of the reinforced (left and bottom) leaflets and for the non-reinforced, isotropic (right) leaflet. The maximum principle Cauchy stresses in the aortic root are scaled with the ratio of the aortic root and leaflet shear modulus for a comprehensible interpretation of the colored stress distributions in the complete valve.

The opening behaviour (frames (a) to (c)) of the reinforced and non-reinforced model is approximately identical. Hence, the fluid dynamical behaviour during this phase is not affected by the presence of fiber-reinforcement. At maximum flow (frame (d)) the non-reinforced leaflet is slightly pushed further into the sinus cavity to show a subsequent fluttering behaviour, whereas the fibers in the other leaflets keep the free edge in a stabilized position. As the aortic pressure decreases and the flow decelerates the valve closes again (frame (e) to (h)). During this phase the non-reinforced leaflet shows high bending deformations, which are thought to stimulate tissue fatigue and

ultimately calcification and/or tearing. The fiber-reinforced leaflets show approximately the same closing configurations when compared to the opening configurations, yielding that no excessive bending deformations are present.

However, for both stentless cases valve closing is not synchronic with the applied flow and pressure curves. The delay in valve closing is believed to result from the combination of Dirichlet conditions at the inflow plane and Neumann conditions at the outflow plane. The natural valve is in late systolic phase subjected to a considerable adverse aortic-ventricular pressure gradient, which is important for final valve closure (Van Steenhoven, 1979; Thubrikar, 1990). By imposing Dirichlet conditions at the inflow plane the desired pressure gradient will not be reached during this phase and certainly not maintained during the diastolic phase. This emphasizes that the flow pulse must be regarded as a response of a valve subjected to ventricular and aortic pressures rather than as a generalized input parameter, which is used in combination with a physiological, but arbitrary aortic pressure curve.

The leaflet stresses during the opening and early closing phase are mainly concentrated near the fixation edge and for the non-reinforced leaflet during the last part of the phase near the free edge. The matrix stresses in the reinforced leaflets are reduced up to 62% (frame (g)) with respect to the non-reinforced leaflet. However, comparison of the stress states per time point is rather awkward for dissimilar reinforced and non-reinforced leaflet configurations. If the maximum tensile stresses attained during the complete systolic phase are compared (91 versus 131 [kPa]), a reduction of approximately 31% is obtained. For the maximum compressive stresses (8 versus 12 [kPa]) this reduction reaches 33%. Since the valve leaflets are designed to bear tensile stresses, they show a high risk of degeneration under compression. Compared with the results of stented models (De Hart *et al.*, 2001b, and Chapter 4), the compressive stresses in the reinforced leaflets (8 versus 25 [kPa]) are reduced with 68%. This is an important feature of aortic root compliance leading to a significant reduction of the cyclic loading pattern in the delicate leaflets.

The stresses in the aortic root are mainly concentrated near the commissures at the outer wall, above the sinus cavities at the inner wall and near the leaflet fixation edge at the inner sinus wall. The stresses at the inner wall near the commissures are very low. The aortic root stress distribution is identical for reinforced and non-reinforced leaflets, however, the maximum value in the non-reinforced case (i.e. 249 [kPa]) is approximately 38% higher. These higher stresses correspond to a (slightly) different configuration of the aortic root, which is not clearly discernible in Figure 5.10. The fibers in the reinforced model that span the free edge between the commissures cause a restriction in commissural outward motion. Although these fibers reduce aortic root stresses, they unintentionally have to bear higher stresses themselves to balance the internal blood pressure. High stresses in these fibers may affect the long-term condition of the leaflets. They can, however, easily be circumvented by increasing the commissural height to lengthen the free edges, such that intercommissural stretch is reduced or prevented.

Calcification and/or stenosis of the valve leaflets is often accompanied by stagnant flow regions persisting throughout the whole cardiac cycle, which stimulate thrombogenecity. In clinical practice the valve performance is therefore evaluated by its wash-out of blood. In Figure 5.11 this wash-out is illustrated for the non-reinforced stentless

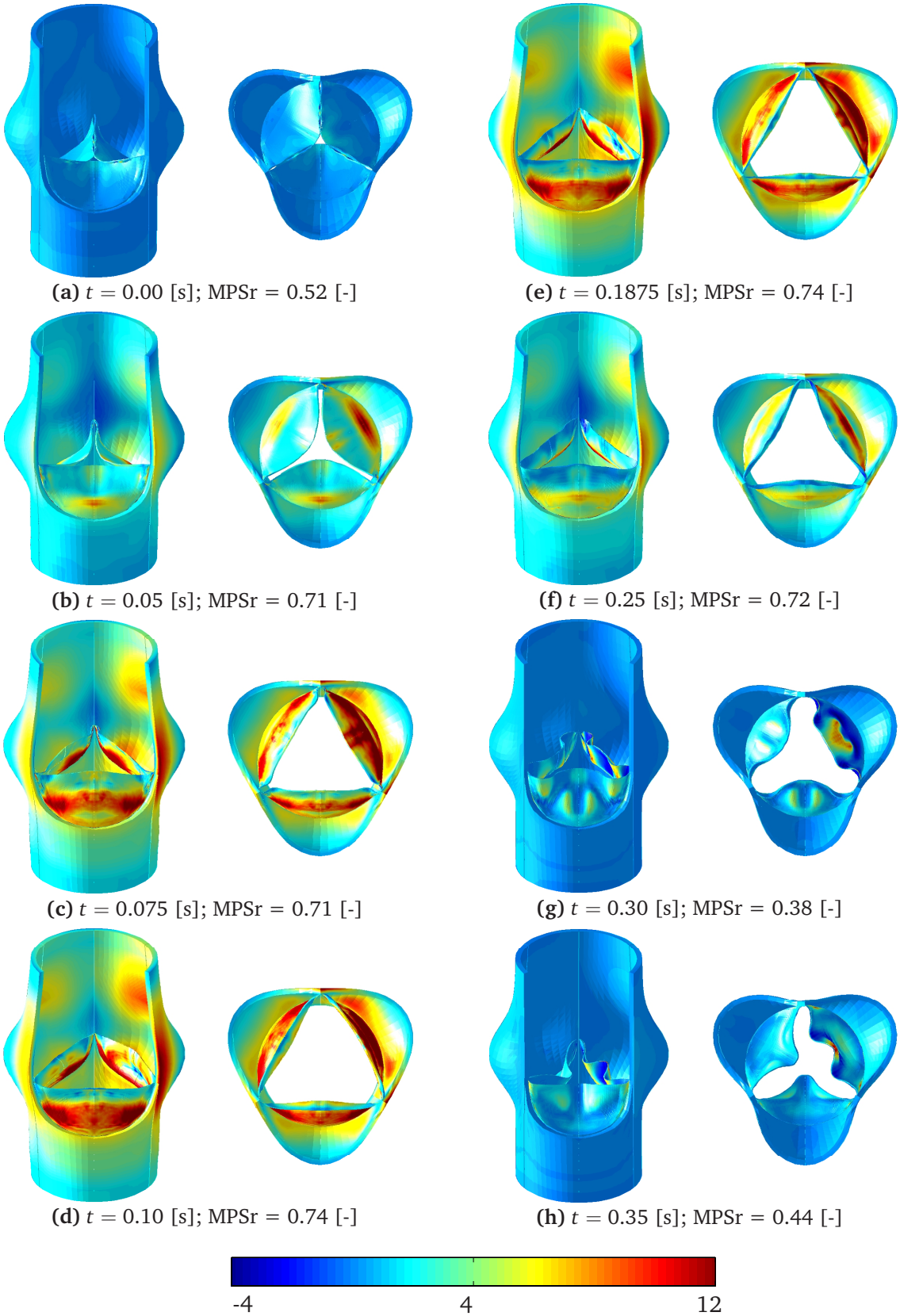

(a) $t = 0.00$ [s]; MPSr = 0.52 [-]
(e) $t = 0.1875$ [s]; MPSr = 0.74 [-]
(b) $t = 0.05$ [s]; MPSr = 0.71 [-]
(f) $t = 0.25$ [s]; MPSr = 0.72 [-]
(c) $t = 0.075$ [s]; MPSr = 0.71 [-]
(g) $t = 0.30$ [s]; MPSr = 0.38 [-]
(d) $t = 0.10$ [s]; MPSr = 0.74 [-]
(h) $t = 0.35$ [s]; MPSr = 0.44 [-]

Figure 5.10: *Maximum principle Cauchy stresses in the leaflet matrix material during systole. In all frames the right leaflet is taken from the non-reinforced model for comparison. MPSr denotes the maximum principle stress ratio of the reinforced and non-reinforced leaflets. The stress scale on the bottom is given in [kPa].*

model during two successive cycles. Frame (a) represents the initial (end diastolic) situation, where fluid particles are positioned upstream the valve and in the sinus cavity, which is frequently considered as a potential stagnant flow region. After the first cycle (frames (a) to (i)) some of the initially upstream positioned particles are mixed with left particles from the sinus cavity. In a subsequent cycle (frames (j) to (l)) all particles have descended into the aorta. Although the blood wash-out is demonstrated for a maximum flow, which is approximately half of the flow reached in the physiological situation, it is assumed that application of the physiological conditions does not introduce stagnant flow regions.

5.6 Discussion

The presented stentless aortic valve model is based on the Galerkin finite element method and implemented in the SEPRAN software package (Segal, 2000). The key features of this model are: 1. three-dimensionality, 2. fully coupled fluid-structure interaction, 3. combined fictitious domain/arbitrary Lagrange-Euler method, 4. fiber-reinforced leaflets, and 5. compliant aortic root. The systolic phase of the cardiac cycle is analyzed by applying a time-dependent plug flow at the inflow plane and aortic pressure curve at the outflow plane. This choice, however, does not allow for analyses during the diastolic phase, in which the leaflets have to bear the diastolic aortic-ventricular pressure gradient. Imposition of Dirichlet conditions at the inflow plane gives rise to internal diastolic ventricular pressures, which are of the same order as the aortic pressures. Free in- and outflow conditions appear to be mandatory for a correct simulation of the valve behaviour during end systolic and diastolic phase.

Fluid dynamical performance is investigated on flow phenomena which are important for aortic valve functioning. Forward flow is observed for all regions in the valve during the opening phase, so the sinus vortex does not persist throughout the whole cardiac cycle. Vortical flow develops at the leaflet free edges when the valve reaches its completely opened configuration. This vortex is stretched into the ascending aorta as the flow starts to decelerate and subsequently initiates a strong back flow at the aortic wall, which pushes the leaflets towards a closed position. This mechanism seems to be the driving force to close this valve design and is possibly enforced if the physiological aortic-ventricular pressure gradient can be attained at end systolic phase. At valve closure a large sinus vortex remains and its intensity decreases as the diastolic phase proceeds. These findings are in contrast with frequently accepted theories reported by Bellhouse *et al.* (1969), who assume that vortical flow in the sinus cavity is important for the closing behaviour and thus precedes aortic valve closure. We like to stress, however, that the mesh resolution of the models is chosen from a time efficient point of view. An increase of resolution might reveal some deviant fluid dynamical behaviour.

The importance of leaflet fiber-reinforcement and aortic root compliance on the long-term performance of the valve is demonstrated by means of the valve stress analysis. The opening configurations are mainly determined by commissural outward motion and are similar for reinforced and non-reinforced leaflets. Different from the opening of stented models reported by De Hart *et al.* (2001b) and in Chapter 4, the leaflets are in the stentless models much less subjected to bending. The contribution of leaflet fiber-reinforcement to aortic valve functioning, during complete valve opening, is to

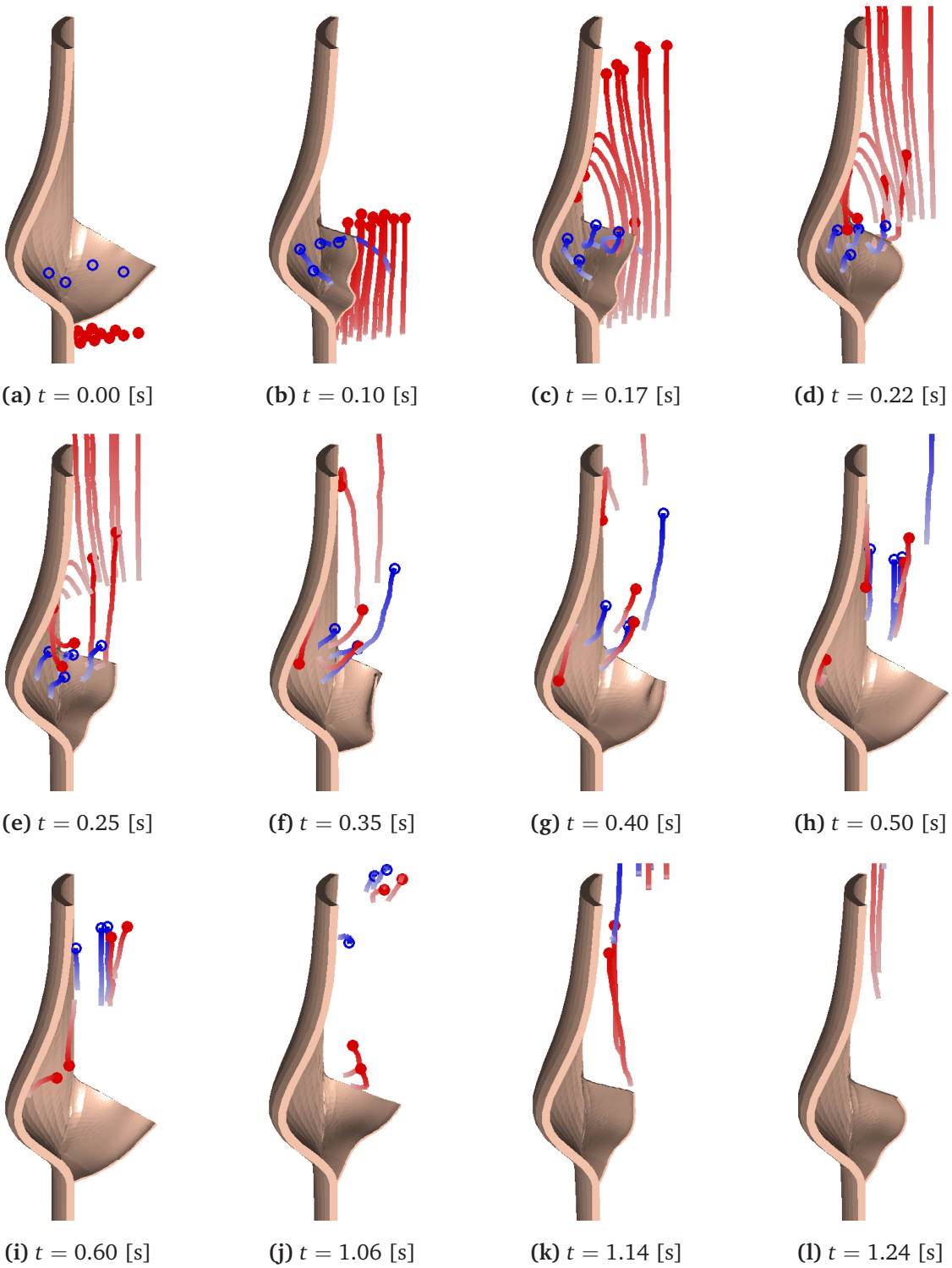

(a) $t = 0.00$ [s] **(b)** $t = 0.10$ [s] **(c)** $t = 0.17$ [s] **(d)** $t = 0.22$ [s]

(e) $t = 0.25$ [s] **(f)** $t = 0.35$ [s] **(g)** $t = 0.40$ [s] **(h)** $t = 0.50$ [s]

(i) $t = 0.60$ [s] **(j)** $t = 1.06$ [s] **(k)** $t = 1.14$ [s] **(l)** $t = 1.24$ [s]

Figure 5.11: *Particle tracking during two successive cardiac cycles.*

stabilize its position and, during valve closing, to prevent high bending deformation of the leaflet free edge. The maximum principle Cauchy stresses in the leaflet matrix material are significantly reduced with 31% and 33% for tensile and compressive stresses, respectively. The effect of aortic root compliance is most significantly present in the compressive stresses. Compared to the reinforced stented model (De Hart *et al.*, 2001b, and Chapter 4) these stresses are reduced with 68%.

Within the context of clinical application, stenotic and/or incompetent valve performance can be studied with respect to associated medical complications using computational models as presented here. Fiber-reinforcement, leaflet geometry, shape and size of the sinus cavities or compliance of the aortic root are design parameters, which can easily be investigated and/or optimized to improved both hemodynamical and mechanical valve performance of existing or new concepts. Guidelines for prosthetic valve design, which are obtained from advanced computational analyses, may prevent expensive and time consuming experimental research.

References

Baaijens, F.P.T., 2001. A fictitious domain/mortar element method for fluid-structure interaction. *International Journal for Numerical Methods in Fluids*, **35**(7): 743-761.

Bathe, K.J, 1982. *Finite Element Procedures in Engineering Analysis*. Prentice-Hall, Inc., New Jersey, USA.

Bellhouse, B.J., Talbot, L., 1969. The fluid mechanics of the aortic valve. *Journal of Fluid Mechanics*, **35**(4): 721-735.

Bertrand, F., Tanguy, P.A., Thibault, F., 1997. A three-dimensional fictitious domain method for incompressible fluid flow problems. *International Journal for Numerical Methods in Fluids*, **25**(6): 719-736.

Cacciola, G., 1998. *Design, Simulation and Manufacturing of Fiber-Reinforced Polymer Heart Valves.* Ph.D. thesis, Eindhoven University of Technology, Eindhoven. *http://www.mate.tue.nl/mate/publications*.

Cacciola, G., De Hart, J., Peters, G.W.M., Schreurs, P.J.G., Baaijens, F.P.T., 1998. A synthetic fibre-reinforced heart valve. *In Proceedings 716 of European Conference on Composite Materials.* Woodhead Publishing Limited, Cambridge, UK.

Caro, C.G., Pedley, J.G., Schroter, R.C., Seed, W.A., 1978. *The Mechanics of the Circulation*. Oxford University Press, Oxford.

Clark, R.E., Finke, E.H., 1974. Scanning and light microscopy of human aortic leaflets in stressed and relaxed states. *Journal of Thoracic and Cardiovascular Surgery*, **67**(5): 792-804.

De Hart, J., Cacciola, G., Schreurs, P.J.G., Peters, G.W.M., 1998. A three-dimensional analysis of a fibre-reinforced aortic valve prosthesis. *Journal of Biomechanics,* **31**(7): 629-638.

De Hart, J., Peters, G.W.M., Schreurs, P.J.G., Baaijens, F.P.T., 2001a. A three-dimensional computational analysis of fluid-structure interaction in the aortic heart valve. Submitted to *Journal of Biomechanics*.

De Hart, J., Peters, G.W.M., Schreurs, P.J.G., Baaijens, F.P.T., 2001b. A computational fluid-structure interaction analysis of a fiber-reinforced stented aortic valve. Submitted to *Journal of Biomechanics*.

Donea, J., Giuliani, S., Halleux, J.P., 1982. An arbitrary Lagrangian-Eulerian finite element method for transient dynamic fluid-structure interactions. *Computer Methods in Applied Mechanics and Engineering*, **33**: 689-723.

Fortin, M., Glowinski, R., 1983. *The Augmented Lagrangian method*. North-Holland Amsterdam.

Glowinski, R., T.-W., Pan, Periaux, J., 1998. Distributed Lagrange multiplier methods for incompressible viscous flow around moving rigid bodies. *Computer Methods in Applied Mechanics and Engineering*, **151**: 181-194.

Johnson, A.A., Tezduyar, T.E., 1994. Mesh update strategies in parallel finite element computations of flow problems with moving boundaries and interfaces. *Computer Methods in Applied Mechanics and Engineering*, **119**: 73-94.

Nerem, R.M., Seed, W.A., 1972. An *in vivo* study of aortic flow disturbances. *Cardiovascular Research*, **6**(1): 1-14.

Nomura, T., Hughes, T.J.R., 1991. An arbitrary Lagrangian-Eulerian finite element method for interaction of fluid and a rigid body. *Computer Methods in Applied Mechanics and Engineering*, **95**(1): 115-138.

Patankar, N.A., Singh, P., Joseph, D.D., Glowinski, R., Pan, T.-W., 2000. A new formulation of the distributed Lagrange multiplier/fictitious domain method for particulate flows. *International Journal of Multiphase Flows*, **26**(9): 1509-1524.

Perktold, K., Rappitsch, G., 1995. Computer simulation of local blood flow and vessel mechanics in a compliant carotid artery bifurcation model. *Journal of Biomechanics*, **28**(7): 845-856.

Reuderink, P.J.R., 1991. *Analysis of the Flow in a 3D Distensible Model of the Carotid Artery Bifurcation*. Ph.D. thesis, Eindhoven University of Technology.

Rutten, M.C.M., 1998. *Fluid-Solid Interaction in Large Arteries*. Ph.D. thesis, Eindhoven University of Technology. *http://www.mate.tue.nl/mate/publications*

Saad, Y., 1996. *Iterative Methods for Sparse Linear Systems*. PWS Publishing Company, Boston.

Sauren, A.A.H.J., 1981. *The Mechanical Behaviour of the Aortic Valve*. Ph.D. thesis, Eindhoven University of Technology, Eindhoven.

Schreurs, P.J.G., 1983. *Numerical Simulation of Forming Processes: the use of the Arbitrary-Eulerian-Lagrangian (AEL) formulation and the finite element method*. Ph.D. thesis, Eindhoven University of Technology, Eindhoven.

Segal, G., 2000. *SEPRAN Introduction, User's Manual, Programmer's Guide and Standard Problems*. Ingenieursbureau SEPRA, Leidschendam.

Thubrikar, M., 1990. *The Aortic Valve*. CRC Press, Boca Raton, Florida.

Van Oijen, C.H.G.A., Van de Vosse, F.N., Baaijens, F.P.T., 2002. An updated Lagrange formulation of a constitutive model for incompressible fiber-reinforced materials at finite strains. Submitted to *Computer Methods in Applied Mechanics and Engineering*.

Van Renterghem, R.J., 1983. *Aortic Valve Geometry During the Cardiac Cycle*. Ph.D. thesis, Eindhoven University of Technology, Eindhoven.

Van Steenhoven, A.A., van Dongen, M.E.H., 1979. Model studies of the closing behaviour of the aortic valve. *Journal of Fluid Mechanics*, **90**(1): 21-32.

Van Steenhoven, A.A., Verlaan, C.W.J., Veenstra, P.C., Reneman, R.S., 1981. In-vivo cinematographic analysis of the behaviour of the aortic valve. *American Journal of Physiology*, **240**(2): H286-H292.

Yang, G.-Z., Mohiaddin, R.H., Kilner, P.J., Firmin, D.N., 1998. Vortical flow feature recognition: a topological study of in vivo flow patterns using MR velocity mapping. *Journal of Computer Assisted Tomography* **22**(4): 577-586.

Chapter 6

Discussion and Conclusions

A three-dimensional computational fluid-structure interaction model of the aortic valve is presented. The merits and demerits of the applied numerical techniques are given in this chapter. Fluid and structure modeling, fluid-structure interaction modeling, boundary conditions and solution strategies are briefly discussed. Based on the findings presented in this thesis the conclusions are given pointwise and, finally, the implication for clinical research is summarized.

6.1 Discussion

6.1.1 Fluid and structure modeling

Blood can be modeled by a range of constitutive models, the simplest being Newtonian, the more complex being microscopic describing the behaviour of the blood cells. Since a homogeneous concentration distribution of blood cells may be assumed in large arteries (Gijsen, 1998), a macroscopic model is adopted for flow in the aorta. In this thesis blood is described as an incompressible continuous liquid medium, of which the rheological behaviour is dominated by red blood cells. This continuum approach is allowed if macroscopical phenomena are investigated as is done in this study. Moreover, a convenient mathematical formulation based on the Navier-Stokes equation and continuity equation can be used to describe the fluid.

In reality, blood shows a viscoelastic and shear thinning behaviour. It has been demonstrated by Gijsen (1998) that this behaviour cannot be neglected for flow in large arteries. However, since this study mainly focuses on fluid-structure interaction, a Newtonian (constant viscosity) model has been chosen for simplicity. The effect of shear thinning and viscoelasticity on the fluid-structure interaction in the aortic valve system requires further investigation.

Many studies have been done on the morphology of the aortic valve leaflets, see e.g. Thubrikar (1990) and references therein. Like all biological tissues, they consist of more than one type of substance and show a viscoelastic, anisotropic and non-linear mechanical behaviour. However, little is known about the interaction between the different components. Hence, constitutive modeling remains complex for such a texture.

The mechanical properties of collagen and elastin together with their structural layout determine the global properties of the leaflets. In the fiber-reinforced models presented in this thesis the natural orthotropic behaviour of the three-layered composite texture is simulated by a continuum approximation. On the finite element level this is implemented using two representative fiber layers of which the properties are defined for each integration point associated with the structural elements. These fiber layers are embedded in a matrix with a low elasticity modulus. The (collagen) fiber-reinforcement of the leaflets gives the investigated valve designs a more stable behaviour throughout the systolic phase. This approach is directly applicable to reinforced synthetic prostheses such as developed by Cacciola (1998). For the natural valve, where collagen fibers are mainly concentrated at the aortic leaflet side, the impact of this approach on the valve behaviour has not been studied yet.

In contrast with the valve leaflets much less is known about the morphology of the aortic root and wall. The behaviour involves not only interaction with the blood, but also an essential interaction with extraneous tissue, which may show muscular activity. Sauren (1981) reported a viscoelastic material behaviour, which was assumed to be isotropic. For simplicity reasons and the lack of available data a linear elastic model is chosen. Moreover, the stress free configuration is important for a correct prediction of the aortic root and wall behaviour. The initial, stress free configuration used in the models is, with the applied aortic pressures, assumed to give a representative systolic behaviour. However, the effect of stress free state and viscoelasticity on aortic root and wall performance requires further investigation.

The geometry of the aortic valve as used in the three-dimensional models is based

on data taken from the literature (Clark *et al.*, 1974; Sauren, 1981) and from synthetic prototype prostheses developed by Cacciola (1998). Moreover, a trileaflet symmetry is assumed, which significantly reduces both memory and computing time. To obtain a realistic model with valve asymmetry and/or imperfections, a full three-dimensional valve system needs to be considered with geometrical input taken from e.g. MR imaging data. The application of realistic input data will be studied in the near future.

6.1.2 Fluid-structure interaction modeling

The interaction of the blood with the leaflets is described using a fictitious domain method. This method allows independent and dissimilar discretizations for the fluid and structural domains, which makes it very appealing in problems that involve large structural deformations and/or motions. Kinematical constraints are enforced weakly using Lagrange multipliers to achieve coupling between the spatially independent domains. However, the resolution of the Lagrange multiplier distribution is, for a correct coupling, strongly dependent on the chosen fluid and structural mesh densities.

Spurious modes of the finite elements are easily attained if too few coupling constraints are applied, whereas locking in the degrees of freedom results from too many additional Lagrange multipliers, leading to an overconstraint set of equations. Although hexahedral elements with triquadratic interpolation fields are not very susceptible to become overconstraint, the elements, which are subjected to Dirichlet conditions, show an increased chance to lock. This numerical phenomenon can be controlled for the structure by taking the number of additional constraints to be constant per element, as is done in this study. However, since the number of structural elements within a fluid element may change during the analysis, the number of additional constraints per fluid element changes accordingly. Hence, it is more complex to control locking in the fluid elements. As to the spurious modes, the resolution of the Lagrange multipliers becomes specifically important if a fluid pressure gradient develops over the structural phase, which may instigate flow through the structure.

Consequently, it is in general difficult to choose a satisfying Lagrange multiplier distribution. The choice adopted in this thesis appears to be sufficient to couple fluid and structural phases without the introduction of spurious modes or locking. Analysis of the diastolic phase, where the leaflets have to bear a considerable aortic-ventricular pressure gradient, possibly fails with this distribution of Lagrange multipliers, since too few constraints are describing the interaction in this high potential flow situation.

The interaction between the blood and the compliant aortic root and wall is described using an arbitrary Lagrange-Euler method. This method is most commonly applied in fluid-structure interaction analyses, involving structural deformations, where a proper fluid mesh quality is preserved. The combination with the fictitious domain method appears to be satisfying in systems such as the aortic valve.

6.1.3 Boundary conditions

The application of a physiological correct flow pulse has most frequently been used in fluid dynamical analyses of cardiovascular systems which are assumed to be rigid. The addition of an associated aortic pressure curve is usually adopted if a compliant sys-

tem is considered. However, when analyzing heart valve functioning, the flow through the valve, and consequently the downstream pressure, are dependent of the valve being considered. Moreover, when a closed valve has to withstand an adverse pressure gradient, it is rather inappropriate to prescribe the inflow conditions. The correct flow follows from the structural deformations caused by this gradient. A more natural choice would be to apply ventricular pressures and model the terminal impedance. However, when applying inhomogeneous Dirichlet and Neumann conditions at the inflow and outflow plane, respectively, the flow through the valve can easily be controlled, which is convenient for testing the numerical tools. With this approach the Lagrange multiplier related problems arising for fluid-structure coupling during diastolic phase (previous section), where the valve has to withstand a considerable adverse pressure gradient, are circumvented, although unintentionally.

At the contact surface, out of plane fluid flow is suppressed by imposing appropriate Dirichlet conditions. It is assumed that the fluid-structure coupling prevents the leaflets from penetrating this surface. Hence, the application of a contact algorithm becomes redundant. As the coupling constraints are weakly enforced at this surface, some penetration may be expected if within a time step the displacement of a structural nodal point towards the contact surface exceeds the distance of this point to the surface. Moreover, the fluid-structure coupling is fully determined by the number of coupling constraints, which thus controls penetration. In the presented models the time step size and number of additional coupling constraints are chosen such to get a balance between correctness of coupling and computational efficiency.

At the leaflet symmetry surface the structural nodal points of the triquadratic hexahedral elements are suppressed for out of plane motion. For a correct simulation of leaflet symmetry, rotation of these nodal points in the plane perpendicular to the symmetry surface needs also to be suppressed. As nodal rotations are no degrees of freedom for these elements, some rotation in the perpendicular plane may be expected. However, in the presented models the associated leaflet elements appear to remain mainly perpendicular to the symmetry edge. A similar situation is observed for the leaflet elements at the fixation surface in the stented models. For modeling thin structures, such as the valve leaflets, finite elements, which are based on the shell theory described by e.g. Hughes (1987); Zienkiewicz and Taylor (1989), would be more appropriate, as rotational degrees of freedom are explicitly defined for such elements. For practical reasons, however, we use triquadratic hexahedral elements to model the complete structural phase. This choice is allowed for the leaflets if the element aspect ratio is restricted to achieve a correct bending behaviour, as is done in this study.

Since a plug flow is prescribed at the inlet, an extra inflow conduct is used to stabilize the fluid flow before entering the valve section. The length of the ascending aorta is taken 25 [mm] measured from the commissural points. The implications for outflow boundary effects when outflow tracts of different lengths are used, needs further investigation.

6.1.4 Solution strategy

A fully coupled solution strategy is used to solve the blood-leaflet interaction problem. This choice is based on the numerical instabilities that arise in weakly coupled methods.

The main advantage of a fully coupled approach is that fluid and structural unknowns are solved simultaneously and, consequently, are completely in equilibrium each time the set of equations is solved. Hence, this strategy makes iterative algorithms to couple the fluid and structure phases redundant. Since the size of the finite element matrix is such that a direct solver requires both a large amount of memory and CPU time, the BiCGstab iterative solver is adopted. The matrix condition of the total system is severely affected by the additional Lagrange multipliers. Consequently, preconditioning of this matrix appears to be necessary. The quality of the preconditioning matrix is chosen such to obtain a balance between solvability and computational efficiency. A 64-bit Alpha 21264DP platform with a 667 MHz processor and a maximum applied memory allocation of 1.6 GB is sufficient to solve all presented models.

Suggestions have been made in Appendix D for alternative solution strategies, which may reduce the computation time. The class of weakly coupled strategies seems to be inappropriate, since during valve opening and closing the leaflets are very sensitive to pressure gradients and are unable to withstand compressive stresses existing in the tangential plane over the full leaflet thickness. Moreover, this situation reverses when the diastolic phase of the cardiac cycle is considered in which the leaflets have to bare considerable pressure gradients. As a consequence it is difficult to adopt a weakly coupled solution strategy, which suffices throughout the complete cardiac cycle. However, in view of the rather coarse finite element meshes and the assumption of trileaflet symmetry, a solution strategy, which significantly reduces the computation time and required memory, would be beneficial. Development of such strategies requires further investigation.

6.2 Conclusions

The conclusions, based on the findings presented in this thesis, read:

- The combined fictitious domain/arbitrary Lagrange-Euler method is a useful numerical tool for systolic fluid-structure interaction analyses in the aortic valve. This tool can be used to evaluate valves on their mechanical and hemodynamical performance for conditions, which are close to the physiological situation.

- The combination of inhomogeneous Dirichlet and Neumann conditions at the in- and outflow surface to load the aortic valve system is inappropriate for analyses of the diastolic phase. Free flow conditions at these surfaces are mandatory for the system to generate the diastolic aortic-ventricular pressure gradient.

- Leaflet fiber-reinforcement has great impact on the mechanical behaviour of the aortic valve. This behaviour is substantially improved, while the hemodynamical performance of the valve is preserved.

- Aortic root compliance significantly affects the aortic valve kinematics by dominating the opening and closing configurations. The valve orifice, which is circular in stented valves, changes from a stellate to a triangular configuration and vice versa, thereby reducing severe leaflet bending deformations, which are typical in stented valves.

- The fluid dynamical phenomena observed in the quasi two-dimensional experiments are reproduced numerically. Although experimental validation of the three-dimensional model has not been performed (yet), the fluid dynamical characteristics such as vortical flow development, vortex orientation and back flow, are qualitatively in agreement with results from most of the experimental studies previously done. However, the numerical model can provide a detailed description of the flow phenomena, which is more difficult to obtain experimentally.

6.3 Clinical application

Computational models such as presented in this thesis can be useful in the cardiovascular research for choosing the time and type of surgical intervention. However, these models can not be regarded as substitutes for the conventional clinical apparatus, which has proven to be reliable over the last few decades. They may specifically be helpful in giving insight in system responses, which are difficult to capture experimentally. Moreover, their application towards development of clinical hardware, such as (new types of) prosthetic valves is of great interest. A significant reduction in the number of animal testings may be achieved if computational techniques are integrated into the clinical research. The computational techniques presented here are, as a matter of course, not confined to the aortic valve system. They can readily be generalized to be applicable to other fluid-structure interaction systems within the cardiovascular regulation.

With respect to diseased aortic valves, a setup of guidelines for designing prosthetic devices can be defined, in which both the mechanical and hemodynamical performance are considered. Design parameters, such as commissural height, free edge length, leaflet/root fixation, leaflet fiber-reinforcement, sinus depth and height, and aortic root compliance, can computationally be optimized depending on the patient's characteristics. The technique is time and cost efficient when compared to currently available experimental methods. This makes computational modeling very appealing in the near future and is believed to reserve a distinct position within the cardiovascular research, however, closely related to and, in some cases, combined with existing clinical techniques.

References

Cacciola, G., 1998. *Design, Simulation and Manufacturing of Fiber-Reinforced Polymer Heart Valves.* Ph.D. thesis, Eindhoven University of Technology, Eindhoven. *http://www.mate.tue.nl/mate/publications*.

Clark, R.E., Finke, E.H., 1974. Scanning and light microscopy of human aortic leaflets in stressed and relaxed states. *Journal of Thoracic and Cardiovascular Surgery*, **67**(5): 792-804.

Gijsen, F.J.H., 1998. *Modeling of Wall Shear Stress in Large Arteries.* Ph.D. thesis, Eindhoven University of Technology. *http://www.mate.tue.nl/mate/publications*.

Hughes, T.J.R., 1987. *The Finite Element Method: Linear Static and Dynamic Finite Element Analysis*. Prentice-Hall, Inc., New Jersey.

Sauren, A.A.H.J., 1981. *The Mechanical Behaviour of the Aortic Valve*. Ph.D.thesis, Eindhoven University of Technology, Eindhoven.

Thubrikar, M., 1990. *The Aortic Valve*. CRC Press, Boca Raton, Florida.

Zienkiewicz, O.C., Taylor, R.L., 1989. *The Finite Element Method*, Volume 2, Fourth Edition. McGraw-Hill, London.

Appendix A

Finite element implementation

This appendix describes some details on the finite element implementation of the fluid-structure interaction problem[1]*. A synopsis will be given without paying attention to the incorporation of the regular boundary conditions. The weighted residuals method is discussed followed by the linearization of the weak form of the problem. To arrive at the finite element equations the Galerkin discretization method is applied. The constitutive relations are not considered in these derivations to preserve generality. For a more precise description the reader is referred to the literature on finite element methods.*

[1]Although Chapters 3 and 4 refer to this appendix, the implementation is given for the combined fictitious domain/arbitrary Lagrange-Euler formulation described in Chapter 5. Hence, the reader is referred to this chapter for additional information on the applied definitions.

A.1 Weighted residuals method

In absence of body forces, the so-called strong form of the equation of motion and the continuity equation for the isothermal and incompressible fluid problem defined on an arbitrary computational grid reads (see Appendix C):

$$\rho_f(\frac{\partial \vec{v}_f}{\partial t} + (\vec{v}_f - \vec{v}_g) \cdot \vec{\nabla}\vec{v}_f) = \vec{\nabla} \cdot \boldsymbol{\sigma}_f, \tag{A.1}$$

$$\vec{\nabla} \cdot \vec{v}_f = 0, \tag{A.2}$$

using the previously defined symbols (see Chapter 5). Equation (A.1) represents the arbitrary Lagrange-Euler (ALE) formulation of the equation of motion with $\vec{v}_g$ the velocity field of the moving fluid grid. For the incompressible structural problem these equations, neglecting inertia terms and body forces, are written as

$$\vec{\nabla} \cdot \boldsymbol{\sigma}_s = \vec{0} \tag{A.3}$$

$$\det(\boldsymbol{F}) = 1 \tag{A.4}$$

The above sets of equations, (A.1), (A.2) and (A.3), (A.4), should hold in any point of the moving fluid domain Ω_g (i.e. Ω_f for the fixed fluid domain in an Eulerian formulation) and the structural domain Ω_s, respectively. Concerning the interaction with the fluid, the structural velocity field is considered rather than the displacement field. Then, coupling of fluid and structural velocity along the fluid-structure interface γ is realized through

$$\vec{v}_f = \vec{v}_s, \tag{A.5}$$

which is enforced using Lagrange multiplier $\vec{\lambda}$ (Fortin *et al.*, 1983). To obtain an approximation of the velocity and pressure fields in the (moving) fluid and structural domain, the weighted residuals method is used (Bathe, 1982; Cuvelier *et al.*, 1986; Hughes, 1987). In this method the residuals of Equation (A.1) and (A.2) are required to be orthogonal to all vector functions $\vec{w}_f$ and scalar functions q_f, respectively, in the proper functional spaces $\mathcal{W}_f$ and $\mathcal{Q}_f$. With respect to Equation (A.3) and (A.4) this set of so-called weighting functions is defined by $\vec{w}_s$ in $\mathcal{W}_s$ and q_s in $\mathcal{Q}_s$. Equivalently, the weighting function associated with Equation A.5 is defined by $\vec{\ell}$ in $\mathcal{L}$. Integration of the weighted residuals equations over the domains Ω_g, Ω_s, and boundary γ yields:

$$\begin{aligned}
&\int_{\Omega_g} \vec{w}_f \cdot \left(\rho_f(\frac{\partial \vec{v}_f}{\partial t} + (\vec{v}_f - \vec{v}_g) \cdot \vec{\nabla}\vec{v}_f) - \vec{\nabla} \cdot \boldsymbol{\sigma}_f \right) d\Omega_g + \int_\gamma \vec{w}_f \cdot \vec{\lambda}\, d\gamma = 0, \\
&\int_{\Omega_g} q_f \, (\vec{\nabla} \cdot \vec{v}_f) \, d\Omega_g = 0,
\end{aligned} \tag{A.6}$$

$$\begin{aligned}
&\int_{\Omega_s} \vec{w}_s \cdot (\vec{\nabla} \cdot \boldsymbol{\sigma}_s) \, d\Omega_s - \int_\gamma \vec{w}_s \cdot \vec{\lambda}\, d\gamma = 0, \\
&\int_{\Omega_s} q_s \, (\det(\boldsymbol{F}) - 1) \, d\Omega_s = 0,
\end{aligned} \tag{A.7}$$

$$\int_\gamma \vec{\ell} \cdot (\vec{v}_f - \vec{v}_s) \, d\gamma = 0, \tag{A.8}$$

which must hold for all admissible weighting functions $\vec{w}_f$, q_f, $\vec{w}_s$, q_s and $\vec{\ell}$. The appearance of $\vec{\lambda}$ in Equations (A.6) and (A.7) is demonstrated in Appendix B. Applying integration by parts on the term $\vec{w}_f \cdot (\vec{\nabla} \cdot \boldsymbol{\sigma}_f)$ yields

$$\int_{\Omega_g} \vec{w}_f \cdot (\vec{\nabla} \cdot \boldsymbol{\sigma}_f)\, d\Omega_g = \int_{\Omega_g} \vec{\nabla} \cdot (\vec{w}_f \cdot \boldsymbol{\sigma_f})\, d\Omega_g - \int_{\Omega_g} (\vec{\nabla}\vec{w}_f)^T : \boldsymbol{\sigma}_f\, d\Omega_g. \tag{A.9}$$

Next, the divergence theorem is used to convert the first term on the right hand side of Equation (A.9) into the boundary integral

$$\int_{\Omega_g} \vec{\nabla} \cdot (\vec{w}_f \cdot \boldsymbol{\sigma}_f)\, d\Omega_g = \int_{\Gamma_g} \vec{w}_f \cdot \vec{t}_f\, d\Gamma_g, \tag{A.10}$$

where $\vec{t}_f = \boldsymbol{\sigma}_f \cdot \vec{n}$ with $\vec{n}$ the outward normal of Γ_g. Following the same procedure for the structural term $\vec{w}_s \cdot (\vec{\nabla} \cdot \boldsymbol{\sigma}_s)$, the strong formulations (A.6) to (A.8) are weakened to the first-order differential equations

$$\begin{aligned}
&\int_{\Omega_g} \vec{w}_f \cdot \rho_f \left(\frac{\partial \vec{v}_f}{\partial t} + (\vec{v}_f - \vec{v}_g) \cdot \vec{\nabla}\vec{v}_f \right) d\Omega_g + \int_{\Omega_g} (\vec{\nabla}\vec{w}_f)^T : \boldsymbol{\sigma}_f\, d\Omega_g + \\
&\qquad + \int_{\gamma} \vec{w}_f \cdot \vec{\lambda}\, d\gamma = \int_{\Gamma_g} \vec{w}_f \cdot \vec{t}_f\, d\Gamma_g, \qquad \text{(A.11)} \\
&\int_{\Omega_g} q_f (\vec{\nabla} \cdot \vec{v}_f)\, d\Omega_g = 0, \\
&\int_{\Omega_s} (\vec{\nabla}\vec{w}_s)^T : \boldsymbol{\sigma}_s\, d\Omega_s - \int_{\gamma} \vec{w}_s \cdot \vec{\lambda}\, d\gamma = 0, \qquad \text{(A.12)} \\
&\int_{\Omega_s} q_s \left(\det(\boldsymbol{F}) - 1 \right) d\Omega_s = 0, \\
&\int_{\gamma} \vec{\ell} \cdot (\vec{v}_f - \vec{v}_s)\, d\gamma = 0, \qquad \text{(A.13)}
\end{aligned}$$

The surface tractions $\vec{t}_s$ that would appear in Equation (A.12) as a result from Equation (A.10) are neglected. Clearly, the above formulations should be supplemented with appropriate boundary conditions.

A.2 Linearization

The problem defined by (A.11) to (A.13) renders a system of non-linear equations, which requires a linearization and an iterative procedure to obtain an approximation of the solution. The fluid problem (A.11) is non-linear with respect to the convection part in terms of the velocity field, whereas the structural problem (A.12) is non-linear with respect to the unknown position field $\vec{x}_s$. This affects the quantities that depend on the current position $\vec{x}_s$, i.e. the changing domain Ω_s, the gradient operator $\vec{\nabla}$ which is taken with respect to the current configuration Ω_s and the stress tensor $\boldsymbol{\sigma}_s$, which is a non-linear function of $(\vec{\nabla}_0 \vec{x}_s)^T$. Although boundary γ moves with the structural domain, the effect on the linearization is usually neglected. However, a linearization of the velocity fields in Equation (A.13) is required for compatibility reasons.

Fluid problem

First, time discretization is performed for the time-dependent terms in Equation (A.11), using an implicit, backward-Euler scheme. Consider the time interval $t^n \rightarrow t^{n+1}$, with time step $\Delta t = t^{n+1} - t^n$, then

$$\frac{\partial \vec{v}_f}{\partial t} \approx \frac{\vec{v}_f - \vec{v}_f^n}{\Delta t}, \tag{A.14}$$

where use is made of the notation $\vec{v}_f = \vec{v}_f^{n+1}$. Next, the Newton linearization procedure is applied to the convection term. Let $\hat{\vec{v}}_f$ be the solution of (A.11), $\vec{v}_f$ the estimate of $\hat{\vec{v}}_f$ and $\delta\vec{v}_f$ the error in the estimate. Taking the fluid grid velocity at time $t = t^n$, i.e. $\vec{v}_g^n$, hence choosing it to be constant during the time interval $t^n \rightarrow t^{n+1}$, then the convection in (A.11) may be elaborated to hold

$$(\vec{v}_f + \delta\vec{v}_f - \vec{v}_g^n)\cdot\vec{\nabla}(\vec{v}_f + \delta\vec{v}_f) = (\vec{v}_f - \vec{v}_g^n)\cdot\vec{\nabla}\vec{v}_f + (\vec{v}_f - \vec{v}_g^n)\cdot\vec{\nabla}\delta\vec{v}_f + \delta\vec{v}_f\cdot\vec{\nabla}\vec{v}_f, \tag{A.15}$$

where the products $\delta(\cdot)\cdot\delta(\cdot)$ are neglected. Applying (A.14) and (A.15) and writing also the Cauchy stress tensor and Lagrange multipliers in terms of their estimates $\boldsymbol{\sigma}_f$ and $\vec{\lambda}$ and their errors $\delta\boldsymbol{\sigma}_f$ and $\delta\vec{\lambda}$, Equation (A.11) may be written as

$$\begin{aligned}\int_{\Omega_g} \vec{w}_f \cdot \rho_f \left(\frac{\delta\vec{v}_f}{\Delta t} + \vec{V}\cdot\vec{\nabla}\delta\vec{v}_f + \delta\vec{v}_f\cdot\vec{\nabla}\vec{v}_f \right) d\Omega_g + \int_{\Omega_g} (\vec{\nabla}\vec{w}_f)^T : \delta\boldsymbol{\sigma}_f \, d\Omega_g + \\ + \int_\gamma \vec{w}_f \cdot \delta\vec{\lambda}\, d\gamma = \int_{\Omega_g/\gamma} \vec{w}_f \cdot \vec{r}_f \, d\Omega_g/\gamma + \int_{\Gamma_g} \vec{w}_f \cdot \vec{t}_f \, d\Gamma_g,\end{aligned} \tag{A.16}$$

with $\vec{V} = (\vec{v}_f - \vec{v}_g^n)$ and $\vec{r}_f$ defined according to

$$\begin{aligned}\int_{\Omega_g/\gamma} \vec{w}_f \cdot \vec{r}_f \, d\Omega_g/\gamma = -\int_{\Omega_g} \vec{w}_f \cdot \rho_f \left(\frac{\vec{v}_f - \vec{v}_f^n}{\Delta t} + \vec{V}\cdot\vec{\nabla}\vec{v}_f \right) d\Omega_g \\ - \int_{\Omega_g} (\vec{\nabla}\vec{w}_f)^T : \boldsymbol{\sigma}_f \, d\Omega_g - \int_\gamma \vec{w}_f \cdot \vec{\lambda}\, d\gamma.\end{aligned} \tag{A.17}$$

Substituting $\delta\boldsymbol{\sigma}_f = -\delta p_f \boldsymbol{I} + \delta\boldsymbol{\tau}_f$, the linearized weak form of (A.11) yields:

$$\begin{aligned}&\int_{\Omega_g} \vec{w}_f \cdot \rho_f \left(\frac{\delta\vec{v}_f}{\Delta t} + \vec{V}\cdot\vec{\nabla}\delta\vec{v}_f + \delta\vec{v}_f\cdot\vec{\nabla}\vec{v}_f \right) d\Omega_g - \int_{\Omega_g} \left(\vec{\nabla}\cdot\vec{w}_f \right) \delta p_f \, d\Omega_g \\ &+ \int_{\Omega_g} (\vec{\nabla}\vec{w}_f)^T : \delta\boldsymbol{\tau}_f \, d\Omega_g + \int_\gamma \vec{w}_f \cdot \delta\vec{\lambda}\, d\gamma = \int_{\Omega_g/\gamma} \vec{w}_f \cdot \vec{r}_f \, d\Omega_g/\gamma + \int_{\Gamma_g} \vec{w}_f \cdot \vec{t}_f \, d\Gamma_g, \\ &\int_{\Omega_g} q_f \left(\vec{\nabla}\cdot\delta\vec{v}_f \right) d\Omega_g = -\int_{\Omega_g} q_f \left(\vec{\nabla}\cdot\vec{v}_f \right) d\Omega_g.\end{aligned} \tag{A.18}$$

The quantities in this linearized weak form are taken with respect to the estimated velocity field $\vec{v}_f$. This is in contrast with (A.11) where quantities are taken with respect to the exact velocity field. Since the structure will be described in an updated Lagrange formulation and Ω_g is explicitly updated ($\vec{v}_g^n$ is constant throughout Δt), the integrals in (A.18) over Ω_g and the gradient operator are defined with respect to the configuration at $t = t^n$.

Structural problem

The structure equations are based upon an updated Lagrange formulation by taking Ω_s^n at $t = t^n$ as the reference configuration (Bathe, 1982). Consequently, the deformation tensor is split as $\boldsymbol{F} = \boldsymbol{F}^{\Delta} \cdot \boldsymbol{F}^n$, where the deformation from the initial configuration Ω_s^0 to Ω_s^n is described by $\boldsymbol{F}^n$ and from Ω_s^n to the current configuration Ω_s by $\boldsymbol{F}^{\Delta}$. The integrations in (A.12) over the current domain Ω_s are transformed to integrations over Ω_s^n by means of the relation: $d\Omega_s = J^{\Delta} d\Omega_s^n$, with $J^{\Delta} = \det(\boldsymbol{F}^{\Delta})$. Since the structure is incompressible[2], J^{Δ} is assumed to be 1. The gradient operator $\vec{\nabla}$ is related to the gradient operator with respect to the reference configuration $\vec{\nabla}^n$ through

$$\vec{\nabla} = (\boldsymbol{F}^{\Delta})^{-T} \cdot \vec{\nabla}^n = \vec{\nabla}^n \cdot (\boldsymbol{F}^{\Delta})^{-1}. \tag{A.19}$$

Using this expression for the first term of the momentum equation in (A.12) yields

$$\int_{\Omega_s} (\vec{\nabla}\vec{w}_s)^T : \boldsymbol{\sigma}_s \, d\Omega_s = \int_{\Omega_s^n} (\vec{\nabla}^n \vec{w}_s)^T : (\boldsymbol{F}^{\Delta})^{-1} \cdot \boldsymbol{\sigma}_s \, d\Omega_s^n. \tag{A.20}$$

Notice that the above transformations are meaningless in the fluid formulation, since Ω_f is assumed to be fixed throughout time step Δt, i.e. $\boldsymbol{F}^{\Delta} = \boldsymbol{I}$.

If $\hat{\vec{x}}_s$ denotes the current position field resulting from the solution of Equation (A.12) and $\vec{x}_s$ is an estimate of $\hat{\vec{x}}_s$, then the error $\delta\vec{x}_s$ in this estimate is given by: $\delta\vec{x}_s = \hat{\vec{x}}_s - \vec{x}_s$. Taking all quantities in (A.12) with respect to the estimate $\vec{x}_s$ and using the definitions $\hat{\boldsymbol{F}}^{\Delta} = \boldsymbol{F}^{\Delta} + \delta\boldsymbol{F}^{\Delta}$, $\hat{\boldsymbol{\sigma}}_s = \boldsymbol{\sigma}_s + \delta\boldsymbol{\sigma}_s$ and $\hat{\vec{\lambda}} = \vec{\lambda} + \delta\vec{\lambda}$, Equation (A.12) may be written as

$$\int_{\Omega_s^n} (\vec{\nabla}^n \vec{w}_s)^T : (\boldsymbol{F}^{\Delta} + \delta\boldsymbol{F}^{\Delta})^{-1} \cdot (\boldsymbol{\sigma}_s + \delta\boldsymbol{\sigma}_s) \, d\Omega_s^n - \int_{\gamma} \vec{w}_s \cdot \delta\vec{\lambda} \, d\gamma = \int_{\gamma} \vec{w}_s \cdot \vec{\lambda} \, d\gamma. \tag{A.21}$$

As stated before, it is common practice to neglect the change of γ in the linearization procedure. This equation is now defined on the reference domain and all quantities are taken with respect to the estimated position field $\vec{x}_s$. Elaboration of the first term on the left hand side in (A.21) yields:

$$\begin{aligned} &\int_{\Omega_s^n} (\vec{\nabla}^n \vec{w}_s)^T : (\boldsymbol{F}^{\Delta} + \delta\boldsymbol{F}^{\Delta})^{-1} \cdot (\boldsymbol{\sigma}_s + \delta\boldsymbol{\sigma}_s) \, d\Omega_s^n = \\ &\qquad \int_{\Omega_s^n} (\vec{\nabla}^n \vec{w}_s)^T : \left((\boldsymbol{F}^{\Delta})^{-1} \cdot \boldsymbol{\sigma}_s + (\boldsymbol{F}^{\Delta})^{-1} \cdot \delta\boldsymbol{\sigma}_s + (\delta\boldsymbol{F}^{\Delta})^{-1} \cdot \boldsymbol{\sigma}_s \right) d\Omega_s^n \end{aligned} \tag{A.22}$$

where the products $\delta(\cdot) \cdot \delta(\cdot)$ are neglected. Using $\hat{\boldsymbol{F}}^{\Delta} \cdot (\hat{\boldsymbol{F}}^{\Delta})^{-1} = \boldsymbol{I}$ the term $(\delta\boldsymbol{F}^{\Delta})^{-1}$ may be written as: $(\delta\boldsymbol{F}^{\Delta})^{-1} = -(\boldsymbol{F}^{\Delta})^{-1} \cdot (\vec{\nabla}\delta\vec{x}_s)^T$. With this expression and using (A.20) Equation (A.21) can be rewritten with respect to the most recent estimate of the domain, i.e. Ω_s:

$$\int_{\Omega_s} (\vec{\nabla}\vec{w}_s)^T : \left(\delta\boldsymbol{\sigma}_s - (\vec{\nabla}\delta\vec{x}_s)^T \cdot \boldsymbol{\sigma}_s \right) d\Omega_s - \int_{\gamma} \vec{w}_s \cdot \delta\vec{\lambda} \, d\gamma = \int_{\Omega_s/\gamma} \vec{w}_s \cdot \vec{r}_s \, d\Omega_s/\gamma, \tag{A.23}$$

[2]The volume ratio factor $J(= J^{\Delta}J^n)$ describes the change in volume of Ω_s with respect to Ω_s^0. Hence, for incompressible materials, $J = 1$ at the known configuration Ω_s. Although in the linearization process Ω_s is yet unknown, J^{Δ} is taken to be 1 for the transformation of the integrals from Ω_s to Ω_s^n. However, a linearization of J is used for the incompressibility condition (A.25).

with the right hand side defined as

$$\int_{\Omega_s/\gamma} \vec{w}_s \cdot \vec{r}_s \, d\Omega_s/\gamma = -\int_{\Omega_s} (\vec{\nabla}\vec{w}_s)^T \cdot \boldsymbol{\sigma}_s \, d\Omega_s + \int_{\gamma} \vec{w}_s \cdot \vec{\lambda} \, d\gamma. \tag{A.24}$$

To linearize the continuity equation the volume ratio is written as $J + \delta J$, with $\delta J = J(\vec{\nabla} \cdot \delta\vec{x}_s)$. This yields

$$\int_{\Omega_s} q_s (\vec{\nabla} \cdot \delta\vec{x}_s) \, d\Omega_s = -\int_{\Omega_s} q_s \frac{(J-1)}{J} \, d\Omega_s, \tag{A.25}$$

where both the left and right hand side have been divided by J. Substituting $\delta\boldsymbol{\sigma}_s = -\delta p_s \boldsymbol{I} + \delta\boldsymbol{\tau}_s$, the linearized weak form of (A.12) follows:

$$\begin{aligned} \int_{\Omega_s} (\vec{\nabla}\vec{w}_s)^T : \left(\delta\boldsymbol{\tau_s} - (\vec{\nabla}\delta\vec{x}_s)^T \cdot \boldsymbol{\sigma_s}\right) d\Omega_s - \int_{\Omega_s} \left(\vec{\nabla} \cdot \vec{w}_s\right) \delta p_s \, d\Omega_s \\ - \int_{\gamma} \vec{w}_s \cdot \delta\vec{\lambda} \, d\gamma = \int_{\Omega_s/\gamma} \vec{w}_s \cdot \vec{r}_s \, d\Omega_s/\gamma, \\ \int_{\Omega_s} q_s \left(\vec{\nabla} \cdot \delta\vec{x}_s\right) d\Omega_s = -\int_{\Omega_s} q_s \frac{(J-1)}{J} \, d\Omega_s. \end{aligned} \tag{A.26}$$

In the sequal the structural velocity field is considered rather than the displacement field. To this end a first-order approximation is used, yielding $\delta\vec{x}_s = \Delta t \, \delta\vec{v}_s$.

Coupling equation

It is straightforward to show that the linearization of the coupling equation (A.13), based on the estimates for the fluid and structural velocity fields, is given by

$$\int_{\gamma} \vec{\ell} \cdot (\delta\vec{v}_f - \delta\vec{v}_s) \, d\gamma = -\int_{\gamma} \vec{\ell} \cdot (\vec{v}_f - \vec{v}_s) \, d\gamma. \tag{A.27}$$

Again, the effect of the changing boundary γ on the linearization procedure is neglected. Considering the structural velocity field rather than the displacement field has consequences for the structural finite element matrix, which will be shown further on.

A.3 Galerkin spatial discretization

The Equations (A.18), (A.26) and (A.27) are spatially discretized using the finite element method (Bathe, 1982; Reddy, 1993). In this method the domains Ω_g, Ω_s and boundary γ are divided into a number of non-overlapping subdomains (elements), Ω_g^e, Ω_s^e and γ^e. Every element consists of a number of nodal points at which the velocity unknowns, pressure unknowns or Lagrange multipliers are defined. The unknowns $\delta\vec{v}_\alpha$ ($\alpha = f, s$), δp_α and $\delta\vec{\lambda}$ at position $\vec{x}_\alpha$ in the associated domain Ω_g^e, Ω_s^e or on boundary γ^e for time t can be approximated by $\delta\vec{v}_\alpha^h$, δp_α^h and $\delta\vec{\lambda}^h$, respectively, using a polynomial interpolation based on the corresponding nodal values. Introducing the column notation ($\underset{\sim}{\cdot}$) and matrix notation ($\underline{\cdot}$), with respect to a Cartesian basis, these interpolation

expressions read:

$$\delta\vec{v}_\alpha^h(\vec{x}_\alpha,t) \quad \rightarrow \quad \delta\underset{\sim}{v}_\alpha(\underset{\sim}{x}_\alpha,t)=\sum_{i=1}^{N}\phi_\alpha^i(\underset{\sim}{x}_\alpha)\delta\underset{\sim}{v}_\alpha^i(t)=\underline{\Phi}_\alpha\delta\underset{\sim}{v}_\alpha^e, \tag{A.28}$$

$$\delta p_\alpha^h(\vec{x}_\alpha,t) \quad \rightarrow \quad \delta p_\alpha(\underset{\sim}{x}_\alpha,t)=\sum_{i=1}^{M}\psi_\alpha^i(\underset{\sim}{x}_\alpha)\delta p_\alpha^i(t)=(\underset{\sim}{\Psi}_\alpha)^T\delta\underset{\sim}{p}_\alpha^e, \tag{A.29}$$

$$\delta\vec{\lambda}^h(\vec{x}_\alpha,t) \quad \rightarrow \quad \delta\underset{\sim}{\lambda}(\underset{\sim}{x}_\alpha,t)=\sum_{i=1}^{L}\theta^i(\underset{\sim}{x}_\alpha)\delta\underset{\sim}{\lambda}^i(t)=\underline{\Theta}\delta\underset{\sim}{\lambda}^e, \tag{A.30}$$

with N, M and L the number of nodal points for the velocity, pressure and Lagrange multipliers, respectively. The functions ϕ_α^i, ψ_α^i and θ^i are the so-called shape functions in nodal point i, which are fully determined by the field $\underset{\sim}{x}_\alpha$ and are associated with the nodal point variables $\delta\underset{\sim}{v}_\alpha^i$, δp_α^i and $\delta\underset{\sim}{\lambda}^i$, which are only functions of time. The columns $(\underset{\sim}{\cdot})^e$ contain the components of all corresponding nodal variables in Ω_g^e, Ω_s^e or on γ^e.

Following the Galerkin method, the discretization of the weighting functions and the unknowns are chosen identical, i.e. Equations (A.28) to (A.30) are defined likewise for the polynomial approximations $\vec{w}_\alpha^h$, q_α^h and $\vec{\ell}^h$ of the corresponding weighting functions using the same shape functions. To this end the finite dimensional subspaces $\mathcal{W}_\alpha^h \subset \mathcal{W}_\alpha$, $\mathcal{Q}_\alpha^h \subset \mathcal{Q}_\alpha$ and $\mathcal{L}^h \subset \mathcal{L}$ are constructed, where $\mathcal{W}_\alpha^h$, $\mathcal{Q}_\alpha^h$ and $\mathcal{L}^h$ are spanned by the set $\left(\phi_\alpha^i, i=1,N\right)$, $\left(\psi_\alpha^i, i=1,M\right)$ and $\left(\theta^i, i=1,L\right)$, respectively. Equations (A.18), (A.26) and (A.27) must now hold for $\vec{w}_\alpha^h \in \mathcal{W}_\alpha^h$, $q_\alpha^h \in \mathcal{Q}_\alpha^h$ and $\vec{\lambda}^h \in \mathcal{L}^h$.

With respect to the terms $\vec{\nabla}\vec{a}$ (with $\vec{a}=\vec{v}_f, \delta\vec{v}_f, \delta\vec{x}_s$, see previous section) it is convenient to introduce the matrix notation

$$\vec{\nabla}\vec{a} \quad \rightarrow \quad \underline{\nabla}_a=\underset{\sim}{\nabla}\underset{\sim}{a}^T. \tag{A.31}$$

A column containing the entries of matrix $\underline{\nabla}_a$ can be defined in terms of the nodal variables $\underset{\sim}{a}^e$ associated with an element:

$$\underline{\nabla}_a \quad \rightarrow \quad \underset{\sim}{\nabla}_a=\underline{\mathrm{B}}_\alpha\,\underset{\sim}{a}^e, \tag{A.32}$$

where matrix $\underline{\mathrm{B}}_\alpha$ transforms the nodal variables $\underset{\sim}{a}^e$ to their partial derivatives and is in structural analysis often referred to as strain-displacement matrix.

Using (A.31) and (A.32) the next characteristic terms appearing in (A.18) are elaborated to arrive at matrix-column notations:

$$\vec{w}_f\cdot\vec{V}\cdot\vec{\nabla}\delta\vec{v}_f=\vec{w}_f\vec{V}:\vec{\nabla}\delta\vec{v}_f \quad \rightarrow \quad \mathrm{tr}(\underset{\sim}{w}_f\underset{\sim}{V}^T\underline{\nabla}_{\delta v_f})=\underset{\sim}{w}_f^T\,\underline{\mathrm{V}}\,\underset{\sim}{\nabla}_{\delta v_f}, \tag{A.33}$$

$$\vec{w}_f\cdot\delta\vec{v}_f\cdot\vec{\nabla}\vec{v}_f=\vec{w}_f\delta\vec{v}_f:\vec{\nabla}\vec{v}_f \quad \rightarrow \quad \mathrm{tr}(\underset{\sim}{w}_f\delta\underset{\sim}{v}_f^T\underline{\nabla}_{v_f})=\underset{\sim}{w}_f^T(\underline{\nabla}_{v_f})^T\delta\underset{\sim}{v}_f, \tag{A.34}$$

$$(\vec{\nabla}\cdot\vec{w}_f)\delta p_f=(\vec{\nabla}\vec{w}_f)^T:\boldsymbol{I}\delta p_f \quad \rightarrow \quad \mathrm{tr}(\underline{\nabla}_{w_f}\underline{I}\delta p_f)=(\underset{\sim}{\nabla}_{w_f})^T\,\underset{\sim}{I}\delta p_f, \tag{A.35}$$

$$(\vec{\nabla}\vec{w}_f)^T:\delta\boldsymbol{\tau}_f \quad \rightarrow \quad \mathrm{tr}(\underline{\nabla}_{w_f}\delta\underline{\tau}_f)=(\underset{\sim}{\nabla}_{w_f})^T\underline{\mathrm{D}}_f\underset{\sim}{\nabla}_{\delta v_f}, \tag{A.36}$$

where the matrix $\underline{\mathrm{D}}_f$ has been introduced to incorporate the contribution of the extra stress tensor $\delta\boldsymbol{\tau}_f$, and $\underset{\sim}{I}$ is the column representation of the unity matrix $\underline{I}$. A formulation similar to (A.35) and (A.36) can be derived for the corresponding structural terms in

Equation (A.26). It is left to the reader to derive a matrix-column notation for the remaining terms in (A.18), (A.26) and (A.27).

Applying a first-order approximation for the structural velocity field[3] , i.e. $\delta \underset{\sim}{x}_s = \Delta t \delta \underset{\sim}{v}_s$, and using (A.28) to (A.30) and (A.33) to (A.36), the discretized version of Equations (A.18), (A.26) and (A.27) on the element level reads:

$$\begin{aligned} &\underset{\sim}{w}_f^{eT}(\underline{\mathrm{M}}_f + \underline{\mathrm{C}}_f + \underline{\mathrm{K}}_f)\delta \underset{\sim}{v}_f^e + \underset{\sim}{w}_f^{eT}\underline{\mathrm{P}}_f^T \delta \underset{\sim}{p}_f^e + \underset{\sim}{w}_f^{eT}\underline{\mathrm{L}}_f^T \delta \underset{\sim}{\lambda}^e = \underset{\sim}{w}_f^{eT} \underset{\sim}{f}_f^v, \\ &\underset{\sim}{q}_f^{eT}\underline{\mathrm{P}}_f \delta \underset{\sim}{v}_f^e = -\underset{\sim}{q}_f^{eT}\underline{\mathrm{P}}_f \underset{\sim}{v}_f^e, \end{aligned} \tag{A.37}$$

$$\begin{aligned} &\underset{\sim}{w}_s^{eT}\Delta t\, \underline{\mathrm{K}}_s \delta \underset{\sim}{v}_s^e + \underset{\sim}{w}_s^{eT}\underline{\mathrm{P}}_s^T \delta \underset{\sim}{p}_s^e + \underset{\sim}{w}_s^{eT}\underline{\mathrm{L}}_s^T \delta \underset{\sim}{\lambda}^e = \underset{\sim}{w}_s^{eT} \underset{\sim}{f}_s^v, \\ &\underset{\sim}{q}_s^{eT}\Delta t\, \underline{\mathrm{P}}_s \delta \underset{\sim}{v}_s^e = \underset{\sim}{q}_s^{eT}(\underset{\sim}{\Psi}_s)^T\left(\frac{J-1}{J}\right), \end{aligned} \tag{A.38}$$

$$\underset{\sim}{\ell}^{eT}(\underline{\mathrm{L}}_f \delta \underset{\sim}{v}_f^e + \underline{\mathrm{L}}_s \delta \underset{\sim}{v}_s^e) = -\underset{\sim}{\ell}^{eT}(\underline{\mathrm{L}}_f \underset{\sim}{v}_f^e + \underline{\mathrm{L}}_s \underset{\sim}{v}_s^e), \tag{A.39}$$

with $\underline{\mathrm{M}}_f$ the fluid mass matrix, $\underline{\mathrm{C}}_f$ the convection matrix and $\underline{\mathrm{K}}_f$ the diffusion matrix:

$$\underline{\mathrm{M}}_f = \int_{\Omega_g^e} \frac{\rho_f}{\Delta t}\, \underline{\boldsymbol{\Phi}}_f^T\, \underline{\boldsymbol{\Phi}}_f\, d\Omega_g^e\,; \quad \underline{\mathrm{C}}_f = \int_{\Omega_g^e} \rho_f\, \underline{\boldsymbol{\Phi}}_f^T \left(\underline{\mathrm{V}}\, \underline{\mathrm{B}}_f + \underline{\nabla}_{v_f}\, \underline{\boldsymbol{\Phi}}\right)\, d\Omega_g^e, \tag{A.40}$$

$$\underline{\mathrm{K}}_f = \int_{\Omega_g^e} \underline{\mathrm{B}}_f^T\, \underline{\mathrm{D}}_f\, \underline{\mathrm{B}}_f\, d\Omega_g^e, \tag{A.41}$$

The divergence matrix $\underline{\mathrm{P}}_f$, coupling matrix $\underline{\mathrm{L}}_f$ and right hand side column $\underset{\sim}{f}_f^v$ read:

$$\underline{\mathrm{P}}_f^T = -\int_{\Omega_g^e} \underline{\mathrm{B}}_f^T\, \underset{\sim}{I}\, \underset{\sim}{\Psi}_f^T\, d\Omega_g^e; \qquad \underline{\mathrm{L}}_f^T = \int_{\gamma^e} \underline{\boldsymbol{\Phi}}_f^T \underline{\Theta}\, d\gamma^e, \tag{A.42}$$

$$\underset{\sim}{f}_f^v = \int_{\Omega_g^e} \underline{\boldsymbol{\Phi}}_f^T\, \underset{\sim}{r}_f^e\, d\Omega_g^e + \int_{\Gamma_f^e} \underline{\boldsymbol{\Phi}}_f^T\, \underset{\sim}{t}_f^e\, d\Gamma_f^e, \tag{A.43}$$

The equivalent structural matrices and columns are expressed by:

$$\underline{\mathrm{P}}_s^T = -\int_{\Omega_s^e} \underline{\mathrm{B}}_s^T\, \underset{\sim}{I}\, \underset{\sim}{\Psi}_s^T\, d\Omega_s^e; \quad \underline{\mathrm{K}}_s = \int_{\Omega_s^e} \underline{\mathrm{B}}_s^T\, (\underline{\mathrm{D}}_s + \underline{\hat{\mathrm{D}}}_s)\, \underline{\mathrm{B}}_s\, d\Omega_s^e, \tag{A.44}$$

$$\underline{\mathrm{L}}_s^T = -\int_{\gamma^e} \underline{\boldsymbol{\Phi}}_s^T\, \underline{\Theta}\, d\gamma^e; \qquad \underset{\sim}{f}_s^v = \int_{\Omega_s^e} \underline{\boldsymbol{\Phi}}_s^T\, \underset{\sim}{r}_s^e\, d\Omega_s^e, \tag{A.45}$$

where $\underline{\hat{\mathrm{D}}}_s$ incorporates the Cauchy stress contribution associated with the most recently computed configuration. The matrices $\underline{\mathrm{K}}_\alpha$ and column $\underset{\sim}{f}_\alpha^v$ ($\alpha = f, s$) depend on the choice of the applied constitutive relations. To preserve generality these will not be elaborated here.

Since Equation (A.37) to (A.39) must hold for all admissible weighting functions the resulting linearized matrix-column notation of the total system assembled over all elements can now be written as

[3]Consider $\underset{\sim}{\hat{v}}_s = \frac{\underset{\sim}{\hat{x}}_s - \underset{\sim}{x}_s^n}{\Delta t}$ defining the structural velocity with $\underset{\sim}{x}_s^n$ the position field at $t = n$. Substituting $\underset{\sim}{\hat{v}}_s = \underset{\sim}{v}_s + \delta \underset{\sim}{v}_s$ and $\underset{\sim}{\hat{x}}_s = \underset{\sim}{x}_s + \delta \underset{\sim}{x}_s$ yields the error in the estimate $\underset{\sim}{v}_s (= \frac{\underset{\sim}{x}_s - \underset{\sim}{x}_s^n}{\Delta t})$ defined by $\delta \underset{\sim}{v}_s = \frac{\delta \underset{\sim}{x}_s}{\Delta t}$.

$$\begin{pmatrix} \begin{bmatrix} \underline{\mathrm{K}}_f^* & \underline{\mathrm{P}}_f^T \\ \underline{\mathrm{P}}_f & \underline{0} \end{bmatrix} & \begin{bmatrix} \\ Z \\ \\ \end{bmatrix} & \begin{bmatrix} \underline{\mathrm{L}}_f^T \\ \underline{0} \end{bmatrix} \\ \begin{bmatrix} \\ Z \\ \\ \end{bmatrix} & \begin{bmatrix} \underline{\mathrm{K}}_s^* & \underline{\mathrm{P}}_s^T \\ \underline{\mathrm{P}}_s^* & \underline{0} \end{bmatrix} & \begin{bmatrix} \underline{\mathrm{L}}_s^T \\ \underline{0} \end{bmatrix} \\ \begin{bmatrix} \underline{\mathrm{L}}_f & \underline{0} \end{bmatrix} & \begin{bmatrix} \underline{\mathrm{L}}_s & \underline{0} \end{bmatrix} & \begin{bmatrix} Z \end{bmatrix} \end{pmatrix} \cdot \begin{pmatrix} \delta \underset{\sim}{v}_f \\ \delta \underset{\sim}{p}_f \\ \delta \underset{\sim}{v}_s \\ \delta \underset{\sim}{p}_s \\ \delta \underset{\sim}{\lambda} \end{pmatrix} = \begin{pmatrix} \underset{\sim}{f}_f^v \\ \underset{\sim}{f}_f^p \\ \underset{\sim}{f}_s^v \\ \underset{\sim}{f}_s^p \\ \underset{\sim}{f}_\lambda \end{pmatrix} \tag{A.46}$$

where $\underline{\mathrm{K}}_f^* = \underline{\mathrm{M}}_f + \underline{\mathrm{C}}_f + \underline{\mathrm{K}}_f$, $\underline{\mathrm{K}}_s^* = \Delta t\, \underline{\mathrm{K}}_s$, $\underline{\mathrm{P}}_s^* = \Delta t\, \underline{\mathrm{P}}_s$ and Z represents the corresponding zero entries. The right hand side vectors associated with the pressure degrees of freedom are given by $\underset{\sim}{f}_f^p = -\underline{\mathrm{P}}_f \underset{\sim}{v}_f$ for the fluid problem and $\underset{\sim}{f}_s^p = (\underset{\sim}{\Psi}_s)^T \frac{J-1}{J}$ for the structure problem. The column operating on the Lagrange multipliers is defined by $\underset{\sim}{f}_\lambda = -(\underline{\mathrm{L}}_f \underset{\sim}{v}_f + \underline{\mathrm{L}}_s \underset{\sim}{v}_s)$. This system of linear algebraic equations can readily be solved. A Newton-Raphson iterative procedure is adopted within each time step to obtain a converged solution. Some details on the solution procedure and linear solver can be found in Appendix D.

References

Bathe, K.J., 1982. *Finite Element Procedures in Engineering Analysis*. Prentice-Hall, Inc., New Jersey, USA.

Cuvelier, C., Segal, A., Van Steenhoven, A.A., 1986. *Finite Element Methods and Navier-Stokes Equations*. D. Reidel Publishing Company, Dordrecht.

Fortin, M., Glowinski, R., 1983. *The Augmented Lagrangian method*. North-Holland, Amsterdam.

Hughes, T.J.R., 1987. *The Finite Element Method: Linear Static and Dynamic Finite Element Analysis*. Prentice-Hall, Inc., New Jersey.

Reddy, J.N., 1993. *An Introduction to the Finite Element Method*. McGraw-Hill, London.

Appendix B

Lagrange multiplier method

The appearance of the Lagrange multiplier in the weighted residuals formulation of problems to which constraints are imposed using the Lagrange multiplier method has most commonly been based on invoking stationarity of an energy functional of the original formulation. A short derivation of the resulting set of equations is given for common linear partial differential equations, which is frequently generalized to hold for non-linear problems.

B.1 Minimization problem

Consider, for example, the class of problems constituted by the following partial differential equation (PDE):

$$\mathcal{L}_\alpha \vec{v}_\alpha = \vec{f}_\alpha \qquad \text{in} \quad \Omega_\alpha, \quad \text{for} \quad \alpha = a, b \tag{B.1}$$

where $\mathcal{L}$ is a linear differential operator, operating on the state variable $\vec{v}_\alpha$ in Ω_α and $\vec{f}_\alpha$ represents a body force. Clearly, equation (B.1) must be supplemented with appropriate boundary conditions. Then, the energy functional $I_\alpha(\vec{v}_\alpha)$ can be written as

$$I_\alpha(\vec{v}_\alpha) = \frac{1}{2}\int_{\Omega_\alpha} \vec{v}_\alpha \cdot \mathcal{L}_\alpha \vec{v}_\alpha \, d\Omega_\alpha - \int_{\Omega_\alpha} \vec{v}_\alpha \cdot \vec{f}_\alpha \, d\Omega_\alpha, \quad \text{for} \quad \alpha = a, b \tag{B.2}$$

Considering the combined system consisting of Ω_a and Ω_b and enforcing the constraint defined by $\vec{v}_a = \vec{v}_b$ at the interface γ of Ω_a and Ω_b, the Lagrangian (Fortin *et al.*, 1983) reads

$$L(\vec{v}_a, \vec{v}_b, \vec{\lambda}) = I_a(\vec{v}_a) + I_b(\vec{v}_b) + \int_\gamma \vec{\lambda} \cdot (\vec{v}_a - \vec{v}_b) \, d\gamma. \tag{B.3}$$

Invoking stationarity of the Lagrangian with respect to $\vec{v}_a$, $\vec{v}_b$ and $\vec{\lambda}$ involves vanishing of the first variation of $L(\vec{v}_a, \vec{v}_b, \vec{\lambda})$ with respect to $\delta\vec{v}_a$, $\delta\vec{v}_b$ and $\delta\vec{\lambda}$ (Cuvelier *et al.*, 1986; Bathe, 1982):

$$\begin{aligned} \delta L = \delta I_a(\vec{v}_a) + \delta I_b(\vec{v}_b) + \int_\gamma \delta\vec{\lambda} \cdot (\vec{v}_a - \vec{v}_b) \, d\gamma + \\ \int_\gamma \vec{\lambda} \cdot \delta\vec{v}_a \, d\gamma - \int_\gamma \vec{\lambda} \cdot \delta\vec{v}_b \, d\gamma = 0 \qquad \forall \quad \delta\vec{v}_a \wedge \delta\vec{v}_b \wedge \delta\vec{\lambda}, \end{aligned} \tag{B.4}$$

where $\delta I_\alpha(\vec{v}_\alpha)$, for $\alpha = a, b$, can be written as

$$\delta I_\alpha(\vec{v}_\alpha) = \int_{\Omega_\alpha} \delta\vec{v}_\alpha \cdot \mathcal{L}\vec{v}_\alpha \, d\Omega_\alpha - \int_{\Omega_\alpha} \delta\vec{v}_\alpha \cdot \vec{f}_\alpha \, d\Omega_\alpha. \tag{B.5}$$

Grouping the variational terms $\delta\vec{v}_a, \delta\vec{v}_b, \delta\vec{\lambda}$ and requiring stationarity for each of these terms results in

$$\int_{\Omega_a} \delta\vec{v}_a \cdot \mathcal{L}\vec{v}_a \, d\Omega_a + \int_\gamma \delta\vec{v}_a \cdot \vec{\lambda} \, d\gamma = \int_{\Omega_a} \delta\vec{v}_a \cdot \vec{f}_a \, d\Omega_a \qquad \forall \quad \delta\vec{v}_a, \tag{B.6}$$

$$\int_{\Omega_b} \delta\vec{v}_b \cdot \mathcal{L}\vec{v}_b \, d\Omega_b - \int_\gamma \delta\vec{v}_b \cdot \vec{\lambda} \, d\gamma = \int_{\Omega_b} \delta\vec{v}_b \cdot \vec{f}_b \, d\Omega_b \qquad \forall \quad \delta\vec{v}_b, \tag{B.7}$$

$$\int_\gamma \delta\vec{\lambda} \cdot (\vec{v}_a - \vec{v}_b) \, d\gamma = 0 \qquad \forall \quad \delta\vec{\lambda}, \tag{B.8}$$

which demonstrates the contribution of $\vec{\lambda}$ and its variational counterpart $\delta\vec{\lambda}$ to the set of system equations.

B.2 Generalization

A sufficient condition for a PDE to have an equivalent energy functional is that the operator $\mathcal{L}$ must be linear. To this class of linear PDE belong all operators appearing in formulations derived in this thesis, except for the non-linear convective term of the Navier-Stokes problem. In other words, there does not exist an equivalent energy functional for convection-diffusion problems. However, the results given here are most commonly generalized to hold for any class of problem to which the weighted residuals formulation is applied. Consequently, the Lagrange multiplier method operates on the Galerkin finite element formulation of the problem to be solved, see e.g. Cuvelier *et al.* (1986) and Bathe (1982).

References

Bathe, K.J., 1982. *Finite Element Procedures in Engineering Analysis*. Prentice-Hall, Inc., New Jersey, USA.

Cuvelier, C., Segal, A., Van Steenhoven, A.A., 1986. *Finite Element Methods and Navier-Stokes Equations*. D. Reidel Publishing Company, Dordrecht.

Fortin, M., Glowinski, R., 1983. *The Augmented Lagrangian method*. North-Holland Amsterdam.

Appendix C

Arbitrary Lagrange-Euler method

The arbitrary Lagrange-Euler (ALE) method is nowadays frequently applied in the computational analysis of problems that involve fluid-structure interaction. Many variants fall within the class of ALE procedures, each differing in the method of controlling the domain configuration. In all these methods the governing equations describing the motion of the continuum are adapted equivalently. The impact on the equilibrium equations describing the fluid problem is briefly outlined in this appendix.

C.1 Coordinate reference systems

One of the basic concepts of the ALE method is the introduction of three separate reference systems for identification of the points in the continuum (Schreurs *et al.*, 1986): the Spatial Reference System (SRS) which is fixed in space according to an Eulerian approach, the Material Reference System (MRS) which moves with the material according to a Lagrangian approach, and the Computational Reference System (CRS) which may move arbitrarily with respect to the considered continuum. These coordinate reference systems each support a different way of labeling the points in the continuum. A point in the MRS is called a material point, and its position with respect to the SRS is denoted by $\vec{x}(t)$ (Figure C.1). The position of this material point with respect to the CRS is denoted by $\vec{x}_g(t)$.

The physical quantities in the governing equations describing the fluid and structure problem are defined with respect to the SRS and MRS respectively. However, in the ALE method the finite element discretization of the fluid domain Ω_f is performed in the CRS (Donea *et al.*, 1982; Johnson *et al.*, 1994; Nomura *et al.*, 1991). Consequently, the finite element formulation of the fluid problem in the CRS can only be accomplished if the quantities defined in the CRS can be coupled to the quantities in the SRS.

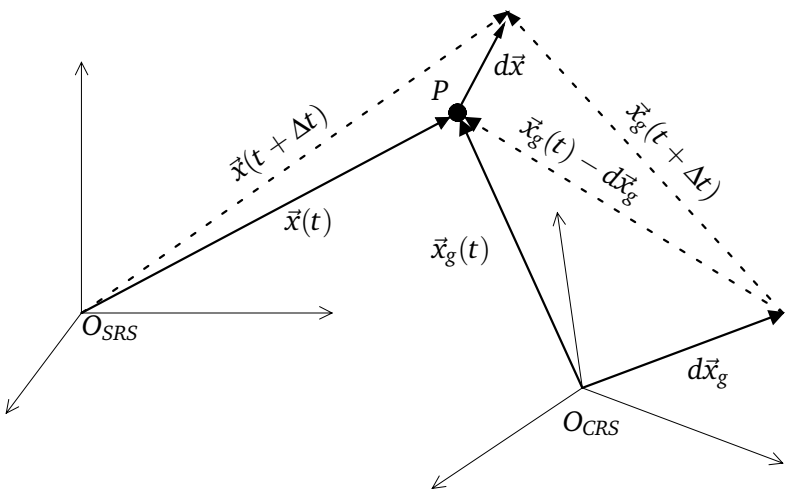

Figure C.1: *Relation between SRS and CRS for a particular material point P.*

C.2 Material derivatives

To couple the CRS with SRS, the evolution of a state variable $\phi(\vec{x},t)$ in material point P is considered and a relation between the material and spatial time derivative is derived.

For an infinitesimally small time step Δt, the position of a material point P with respect to the SRS has changed from $\vec{x}(t)$ to $\vec{x}(t+\Delta t) = \vec{x}(t) + d\vec{x}$, see Figure (C.1).

Then the material derivative for $\Delta t \to 0$ can be written as

$$\begin{aligned}\frac{\mathrm{D}\phi}{\mathrm{D}t} &= \lim_{\Delta t\to 0}\frac{1}{\Delta t}\Big(\phi(\vec{x}+d\vec{x},t+\Delta t)-\phi(\vec{x},t)\Big)\\ &= \lim_{\Delta t\to 0}\frac{1}{\Delta t}\Big(\phi(\vec{x}+d\vec{x},t+\Delta t)-\phi(\vec{x},t+\Delta t)+\phi(\vec{x},t+\Delta t)-\phi(\vec{x},t)\Big)\\ &= \lim_{\Delta t\to 0}\frac{1}{\Delta t}\Big(d\vec{x}\cdot(\vec{\nabla}\phi)+\phi(\vec{x},t+\Delta t)-\phi(\vec{x},t)\Big)\\ &= \vec{v}\cdot(\vec{\nabla}\phi)+\left.\frac{\partial\phi}{\partial t}\right|_{\vec{x}},\end{aligned} \tag{C.1}$$

where $\vec{v}$ is the velocity of the material point and $\vec{\nabla}$ the gradient operator with respect to the SRS.

The position of the material point P with respect to the CRS changes from $\vec{x}_g(t)$ to $\vec{x}_g(t+\Delta t) = \vec{x}_g(t) + (d\vec{x} - d\vec{x}_g)$. By replacing $\vec{x}$ and $d\vec{x}$ in equation (C.1) with $\vec{x}_g$ and $(d\vec{x} - d\vec{x}_g)$, respectively, it is straightforward to show that

$$\frac{\mathrm{D}\phi}{\mathrm{D}t} = (\vec{v}-\vec{v}_g)\cdot(\vec{\nabla}\phi)+\left.\frac{\partial\phi}{\partial t}\right|_{\vec{x}_g}, \tag{C.2}$$

where $\vec{v}_g$ denotes the grid velocity and $\vec{\nabla}$ remains operating with respect to the SRS. Notice that the term $\frac{\partial\phi}{\partial t}$ is now defined in the grid point $\vec{x}_g$.

Consider next a material point P in a moving fluid domain Ω_g, which is defined in the CRS. The momentum and continuity equation in this point read (using the previously defined notation):

$$\begin{aligned}\rho_f\frac{\mathrm{D}\vec{v}_f}{\mathrm{D}t} &= \vec{\nabla}\cdot\boldsymbol{\sigma}_f+\vec{f}_f,\\ \frac{\mathrm{D}\rho_f}{\mathrm{D}t} &= \rho_f\vec{\nabla}\cdot\vec{v}_f.\end{aligned} \tag{C.3}$$

Elaboration of the material derivative of $\vec{v}_f$ and ρ_f yields the ALE formulation of the momentum and continuity equations:

$$\rho_f\frac{\partial\vec{v}_f}{\partial t}+\rho_f(\vec{v}_f-\vec{v}_g)\cdot\vec{\nabla}\vec{v}_f = \vec{\nabla}\cdot\boldsymbol{\sigma}_f+\vec{f}_f, \tag{C.4}$$

$$\frac{\partial\rho_f}{\partial t}+(\vec{v}_f-\vec{v}_g)\cdot\nabla\rho_f = \rho_f\vec{\nabla}\cdot\vec{v}_f. \tag{C.5}$$

Substitution of the constitutive equation defined by $\boldsymbol{\sigma}_f = -p_f\boldsymbol{I}+2\eta\boldsymbol{D}_f$ yields the well-known Navier-Stokes equation

$$\rho_f\left(\frac{\partial\vec{v}_f}{\partial t}+(\vec{v}_f-\vec{v}_g)\cdot\vec{\nabla}\vec{v}_f\right) = -\vec{\nabla}p_f+\vec{\nabla}\cdot 2\eta\boldsymbol{D}_f+\vec{f}_f, \tag{C.6}$$

while the incompressible behaviour, in case of a constant density ρ_f, simplifies the continuity equation (C.5) to

$$\vec{\nabla}\cdot\vec{v}_f = 0, \tag{C.7}$$

Hence, the ALE formulation of the Navier-Stokes equation is equivalent to its Eulerian formulation (i.e. $\vec{v}_g = \vec{0}$) except for the additive convective term $-\vec{v}_g \cdot \vec{\nabla}\vec{v}_f$ and the term $\frac{\partial \vec{v}_f}{\partial t}$, which is defined in $\vec{x}_g$. The Lagrangian formulation can easily be obtained if in any point at any time the grid velocity equals the velocity of the material points, i.e. $\vec{v}_g = \vec{v}_f$, and thus material and grid points coincide.

References

Donea, J., Giuliani, S., Halleux, J.P., 1982. An arbitrary Lagrangian-Eulerian finite element method for transient dynamic fluid-structure interactions. *Computer Methods in Applied Mechanics and Engineering*, **33**: 689-723.

Johnson, A.A., Tezduyar, T.E., 1994. Mesh update strategies in parallel finite element computations of flow problems with moving boundaries and interfaces. *Computer Methods in Applied Mechanics and Engineering*, **119**: 73-94.

Nomura, T., Hughes, T.J.R., 1991. An arbitrary Lagrangian-Eulerian finite element method for interaction of fluid and a rigid body. *Computer Methods in Applied Mechanics and Engineering*, **95**: 115-138.

Schreurs, P.J.G., Veldpaus, F.E., Brekelmans, W.A.M., 1986. Simulation of forming processes, using the arbitrary Eulerian-Lagrangian formulation. *Computer Methods in Applied Mechanics and Engineering*, **58**: 19-36.

Appendix D

Solution procedures

Many strategies exist for solving coupled problems, each with their own amenities for the specific problem to be solved. In the aortic valve system the solution of each of the subproblems, i.e. the fluid, structure and, if aortic wall compliance is considered, moving grid problem[1]*, depends on the solution of the other subproblem. A distinction is made between weakly coupled and fully coupled approaches to obtain an approximation of the solution of the total system. In this appendix some of the weakly coupled strategies that have been tested are described and their failures in the application to the aortic valve are discussed. The merits and demerits of a fully coupled approach are outlined, leading to the solution scheme, which is adopted here to solve the fluid-structure problem.*

[1]The solution strategies given in this appendix incorporate the moving grid problem associated with the arbitrary Lagrange-Euler formulation for the fluid, which is discussed in Chapter 5.

D.1 Weakly coupled methods

In weakly coupled methods the subsystems are considered individually during one discrete time step rather than considering the total system. These methods are also referred to as partitioned or staggered procedures (Felippa *et al.*, 1998; Farhat *et al.*, 1998; Wall *et al.*, 1998), which are most frequently applied to solve three field problems, such as the fluid, structure and moving (fluid) grid problems presented in this thesis. In this approach the equilibrium equations associated with each subsystem are solved using the most recently computed solutions of the other subsystems. As a result, for each subproblem well established but distinct numerical solvers can be adopted, which are best suited for that particular subproblem. This makes the staggered approach very appealing in fluid-structure interaction problems.

A generally used weakly coupled strategy is described next and its application to the aortic valve system is discussed. Neglecting external body forces, the weak form of the isothermal and incompressible fluid problem in Ω_g (using previously defined notations) read for this strategy:

$$\begin{aligned}
&\int_{\Omega_g} \vec{w}_f \cdot \rho_f \left(\frac{\partial \vec{v}_f}{\partial t} + (\vec{v}_f - \vec{v}_g) \cdot \vec{\nabla} \vec{v}_f \right) d\Omega_g + \int_{\Omega_g} (\vec{\nabla} \vec{w}_f)^T : \boldsymbol{\tau}_f \, d\Omega_g - \\
&\qquad\qquad \int_{\Omega_g} (\vec{\nabla} \cdot \vec{w}_f) \, p_f \, d\Omega_g + \int_{\gamma^i} \vec{w}_f \cdot \vec{\lambda} \, d\gamma^i = \int_{\Gamma_g} \vec{w}_f \cdot \vec{t}_f \, d\Gamma_g, \\
&\int_{\Omega_g} q_f \, (\vec{\nabla} \cdot \vec{v}_f) \, d\Omega_g = 0, \\
&\int_{\gamma^i} \vec{\ell} \cdot \vec{v}_f \, d\gamma^i = \int_{\gamma^i} \vec{\ell} \cdot \vec{v}_s \, d\gamma^i,
\end{aligned} \tag{D.1}$$

with γ^i the boundary of the immersed structures and $\vec{t}_f$ the externally applied surface load. In this formulation the fluid velocity at γ^i is prescribed using the local structural velocity field ($\vec{v}_s$), which is assumed to be known. The solution of the fluid problem renders the surface traction $\vec{\lambda}$, resulting from the weakly enforced coupling constraint (last equation of D.1), and $(-p_f \boldsymbol{I} + \boldsymbol{\tau_f}) \cdot \vec{n}$, which the fluid exerts on γ^i and γ^b, respectively. These forces are applied to the incompressible structural problem defined in Ω_s:

$$\begin{aligned}
&\int_{\Omega_s} (\vec{\nabla} \vec{w}_s)^T : \boldsymbol{\tau}_s \, d\Omega_s - \int_{\Omega_s} (\vec{\nabla} \cdot \vec{w}_s) \, p_s \, d\Omega_s = \int_{\gamma^i} \vec{w}_s \cdot \vec{\lambda} \, d\gamma^i + \int_{\gamma^b} \vec{w}_s \cdot \vec{t}_s \, d\gamma^b, \\
&\int_{\Omega_s} q_s \left(\det(\boldsymbol{F}) - 1 \right) d\Omega_s = 0,
\end{aligned} \tag{D.2}$$

with γ^b the boundary of the bounding structures and $\vec{t}_s = (-p_f \boldsymbol{I} + \boldsymbol{\tau}_f) \cdot \vec{n}$ at γ^b. From the computed structural displacement field $\vec{u}_s$ the velocity field $\vec{v}_s$ at γ^i is derived using a first-order approximation in time. The structural displacement $\vec{u}_s$ at γ^b is used to accommodate the fluid domain to the change in γ^b. A proper fluid mesh quality is preserved by computing a fluid grid displacement field $\vec{u}_g$ from the linear elastic (moving grid) problem defined in Ω_g:

$$\int_{\Omega_g} \boldsymbol{\varepsilon}_{w_g} : \left({}^4\boldsymbol{C} : \boldsymbol{\varepsilon}_{u_g} \right) d\Omega_g = 0, \tag{D.3}$$

to which $\vec{u}_s$ at γ^b are prescribed. In this equation, ${}^4\boldsymbol{C}$ denotes the fourth-order Hookean elasticity tensor, ε_{u_g} the elastic strain tensor and $\boldsymbol{\varepsilon}_{w_g}$ its variational counterpart with respect to the field $\vec{w}_g$. The fluid mesh is accommodated accordingly and a grid velocity field $\vec{v}_g$ is computed (using also a first-order approximation). This velocity field and $\vec{v}_s$ at γ^i are passed back to the fluid problem D.1, which is subsequently solved again. This sequence is repeated for each time step or for each iteration within each time step, which is known to be the strongly coupled variant of staggered procedures. The procedure is schematically depicted in Figure D.1.

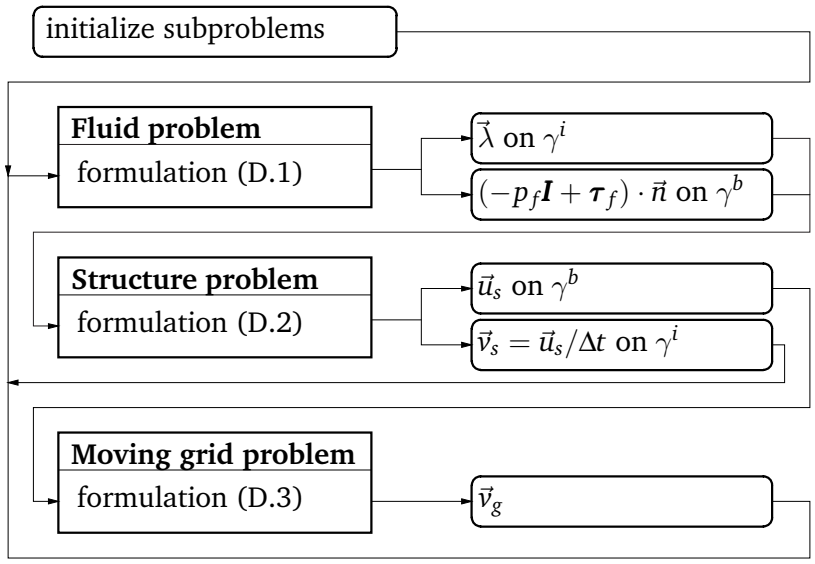

Figure D.1: *A three field staggered approach for solving fluid-structure interaction problems.*

The solution method described above cannot generally be applied to couple a fluid, with blood analog characteristics, and a structure, which has small inertia, damping and bending stiffness, like a heart valve leaflet. Consider for example the valve opening and closing phase when the valve leaflets are mostly subjected to very low strains or might even be partly strain free. Then, in some parts insignificant internal stresses are present and consequently, the fluid forces on both sides of the leaflets should balance. If the weakly coupled method illustrated in Figure D.1 is applied, first the position and/or velocity of the boundary γ^i is estimated. After solving the fluid problem, the fluid stresses on both sides of the leaflets generally will not balance. The resulting fluid load $\vec{\lambda}$ is applied to the leaflets and the displacement field is computed. Due to the small stiffness of the structure the displacements will be very large in order to obtain internal stresses which balance the fluid load. Apart from the numerical instabilities that arise, it will be clear that this situation is physically unrealistic. Hence, it is extremely important to control the load which is exerted on the leaflets, using e.g. an underrelaxation scheme, introducing artificial structural damping or decreasing the time step size. However, numerical experiments show that none of these interferences appears to be successful in analyzing the interaction with the highly flexible valve leaflets using the presented weakly coupled strategy. On the other hand, a simple underrelaxation scheme for the fluid load or a reasonable time step size is sufficient to describe the interaction with the aortic wall using the solution procedure described above.

An alternative decoupling of the total system may result in the next weak formulation of the fluid problem:

$$\begin{aligned}
&\int_{\Omega_g} \vec{w}_f \cdot \rho_f \left(\frac{\partial \vec{v}_f}{\partial t} + (\vec{v}_f - \vec{v}_g) \cdot \vec{\nabla} \vec{v}_f \right) d\Omega_g + \int_{\Omega_g} (\vec{\nabla} \vec{w}_f)^T : \boldsymbol{\tau}_f \, d\Omega_g - \\
&\qquad \int_{\Omega_g} (\vec{\nabla} \cdot \vec{w}_f) \, p_f \, d\Omega_g = \int_{\Gamma_g} \vec{w}_f \cdot \vec{t}_f \, d\Gamma_g - \int_{\gamma^i} \vec{w}_f \cdot \vec{\lambda} \, d\gamma^i, \\
&\int_{\Omega_g} q_f \, (\vec{\nabla} \cdot \vec{v}_f) \, d\Omega_g = 0.
\end{aligned} \tag{D.4}$$

The essential difference with the previous solution method is the transport of state variables from one subproblem to the other. Here the fluid velocity and pressure fields are computed without weakly enforcing the fluid-structure coupling constraint. Instead, the effect of this constraint is incorporated by prescribing the associated coupling force $\vec{\lambda}$, which is therefore assumed to be known. The fluid velocity field $\vec{v}_f$ at γ^i and fluid surface load $(-p_f \boldsymbol{I} + \boldsymbol{\tau}_f) \cdot \vec{n}$ at γ^b are passed to the structural problem, which is now defined by

$$\begin{aligned}
&\int_{\Omega_s} (\vec{\nabla} \vec{w}_s)^T : \boldsymbol{\tau}_s \, d\Omega_s - \int_{\Omega_s} (\vec{\nabla} \cdot \vec{w}_s) \, p_s \, d\Omega_s - \int_{\gamma^i} \vec{w}_s \cdot \vec{\lambda} \, d\gamma^i = \int_{\gamma^b} \vec{w}_s \cdot \vec{t}_s \, d\gamma^b, \\
&\int_{\Omega_s} q_s \, \Big(\det(\boldsymbol{F}) - 1 \Big) \, d\Omega_s = 0, \\
&\int_{\gamma^i} \vec{\ell} \cdot \vec{v}_s \, d\gamma^i = \int_{\gamma^i} \vec{\ell} \cdot \vec{v}_f \, d\gamma^i,
\end{aligned} \tag{D.5}$$

with $\vec{t}_s = (-p_f \boldsymbol{I} + \boldsymbol{\tau}_f) \cdot \vec{n}$ at γ^b. The solution of the structural problem renders the displacement field $\vec{u}_s$ and the coupling force $\vec{\lambda}$. The displacement field at γ^b is applied to the moving grid problem (D.3), which is subsequently solved. The resulting grid velocity field $\vec{v}_g$ and the force $\vec{\lambda}$ are coupled back to the fluid problem D.4. The staggered procedure for this decoupled strategy is summarized in Figure D.2.

This solution scheme as presented here neither appears to be successful in the analysis of the aortic valve system. The prescription of fluid velocities on the valve leaflets results in an unrealistic internal stress distribution that severely affects the fluid flow when applied back to the fluid problem. This can easily be understood by the fact that the highly flexible thin-walled structures are designed to bear tensile stresses rather than compressive stresses. Moreover, in the closed position the valve leaflets have to withstand a considerable pressure gradient. Corresponding structural stresses are of such a magnitude that instability in the flow computation is easily attained. To circumvent these instabilities a set of different numerical strategies have been examined. The use of an underrelaxation scheme for the prescribed fluid velocities along γ^i or a decrease of the time step size show no significant improvement. A simplification for the structural problem would be to neglect of the physically unrealistic compressive stresses, although still prescribing the fluid velocities along γ^i. Combined with a distribution of the coupling force $\vec{\lambda}$ to a larger area surrounding the leaflets, an improvement of the numerical stability is most probably to be achieved. A similar approach was adopted by Peskin *et al.* (1977) and Peskin *et al.* (1995) for low Reynolds number problems, where the structural domain is described by sets of fibers. However, applied to more

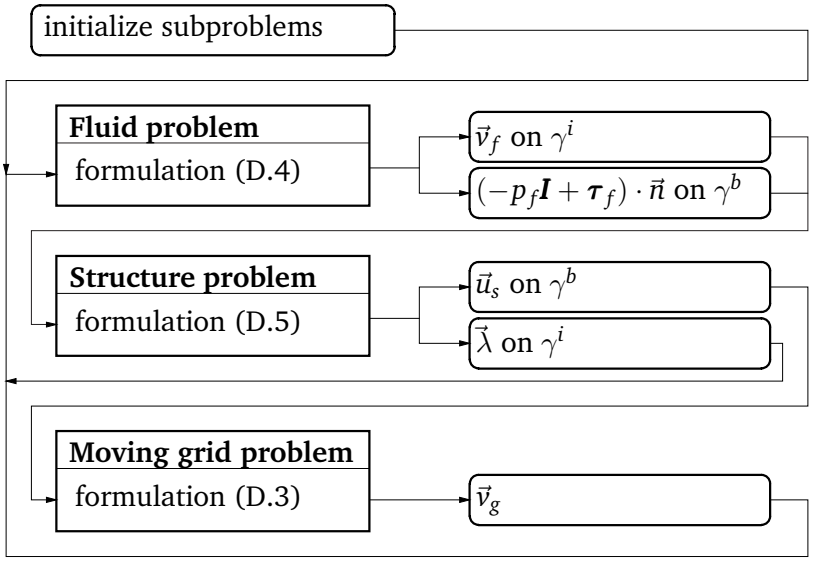

Figure D.2: *Alternative staggered approach for solving fluid-structure interaction problems.*

sophisticated structures that are partly able to bear compression this method is likely to fail. An interesting solution to this, from a numerical point of view, unstable behaviour of the system would be to prescribe the normal fluid velocities and the tangential fluid load at the interface γ^i. In combination with an appropriate distribution of the coupling forces to the fluid domain this approach is worthwhile to be considered in the future as a possible solution to this instability problem.

D.2 Fully coupled method

To circumvent the numerical instabilities mentioned above, a fully coupled approach is adopted to solve the aortic valve model described in this thesis. To this end the following problem formulations are defined. Neglecting external body forces and surface tractions, the governing equations for the fluid are written

$$\begin{aligned}\int_{\Omega_g} \vec{w}_f \cdot \rho_f \left(\frac{\partial \vec{v}_f}{\partial t} + (\vec{v}_f - \vec{v}_g)\cdot\vec{\nabla}\vec{v}_f \right) d\Omega_g + \int_{\Omega_g} (\vec{\nabla}\vec{w}_f)^T : \boldsymbol{\tau}_f \, d\Omega_g - \\ \int_{\Omega_g} (\vec{\nabla}\cdot\vec{w}_f)\, p_f \, d\Omega_g + \int_{\gamma^i} \vec{w}_f \cdot \vec{\lambda} \, d\gamma^i = \int_{\Gamma_g} \vec{w}_f \cdot \vec{t}_f \, d\Gamma_g, \\ \int_{\Omega_g} q_f \, (\vec{\nabla}\cdot\vec{v}_f)\, d\Omega_g = 0,\end{aligned} \tag{D.6}$$

while the structural problem is defined by

$$\begin{aligned}\int_{\Omega_s} (\vec{\nabla}\vec{w}_s)^T : \boldsymbol{\tau}_s \, d\Omega_s - \int_{\Omega_s} (\vec{\nabla}\cdot\vec{w}_s)\, p_s \, d\Omega_s - \int_{\gamma^i} \vec{w}_s \cdot \vec{\lambda} \, d\gamma^i = 0, \\ \int_{\Omega_s} q_s \left(\det(\boldsymbol{F}) - 1 \right) d\Omega_s = 0.\end{aligned} \tag{D.7}$$

In these equations $\vec{\lambda}$ is an extra unknown related to the usual coupling constraint defined by

$$\int_{\gamma^i} \vec{\ell} \cdot (\vec{v}_f - \vec{v}_s)\, d\gamma^i = 0. \tag{D.8}$$

Again, the moving grid problem remains unchanged and is described by D.3. Notice, that the interaction on γ^b is taken into account implicitly, since fluid and structural discretizations along γ^b are taken identical (see Chapter 5). The solution procedure which is adopted here is depicted in Figure D.3 and described next.

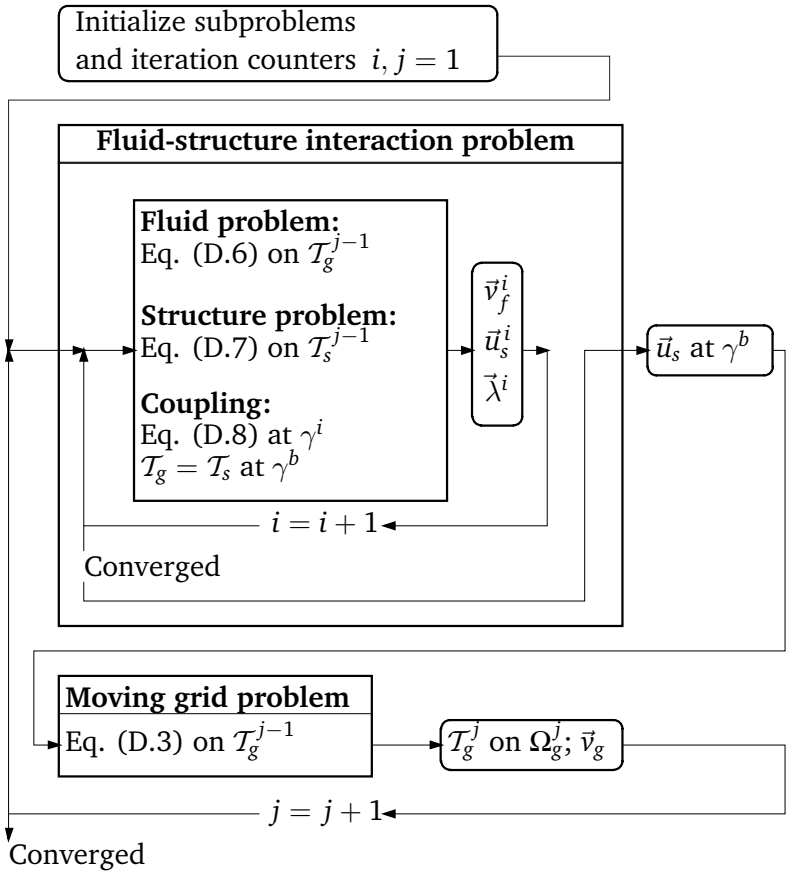

Figure D.3: *The fully coupled iterative solution procedure.*

First the initial configurations of the fluid domain Ω_g and Ω_s are discretized to obtain a mesh $\mathcal{T}_g$ on Ω_g and $\mathcal{T}_s$ on Ω_s. The iteration counters i for the fluid-structure interaction problem and j for the total problem, including the moving grid problem, are set to one. Then for each time step the following actions are taken. The fluid problem and structural problem are solved simultaneously with the additional coupling constraint (D.8). The solution of this fully coupled problem is checked for convergence with respect to the state variables $\vec{v}_f$, $\vec{u}_s$ and $\vec{\lambda}$ and with respect to the residual in the right hand side vector. If convergence is obtained the structural displacement field at γ^b is prescribed to the moving grid problem. $\mathcal{T}_g^{j-1}$ is updated and $\vec{v}_g$ is computed. Next, j is upgraded and the fluid-structure interaction problem is solved again where the fluid velocity and

pressure fields are solved on $\mathcal{T}_g^j$. This process is repeated until convergence for the total system has been reached.

There are a few interesting points concerning this scheme. First of all, with each Newton iteration i the displacement field of the structure is fully coupled to the velocity field of the fluid. This obviates the need for an additional iterative procedure between the fluid and structural subproblems. Secondly, at each Newton iteration the fluid-structure coupling through equation (D.8) is enforced using the location of γ^i defined at the beginning of the current time step. Enforcement on the most recently computed location of γ^i affects the convergence rate. Analog to the previously described weakly coupled strategies the moving grid problem is decoupled from the fluid and structural subproblems. Consequently, the update of $\mathcal{T}_g$ at each iteration j implies that the corresponding grid velocity $\vec{v}_g$, passes back to the fluid problem, results in an explicit definition for the additional convection. This simplifies the linearization process described in Appendix A significantly. The decoupling of the moving grid problem results in a linear contribution of the extra convective term to the system equations, improving the convergence rate of the total system with respect to an implicit grid update.

On the other hand, the fully coupled strategy leads to a matrix-vector structure (see Appendix A), which is far from being efficient to solve numerically. The ill-conditioned matrix requires special attention on the choice of the linear solver being applied.

D.3 Linear solver

In the following, the attention will be focused on the linearized system of equations related to the fluid-structure interaction problem rather than to the moving grid problem, which is fairly easy to solve. The linearized system of algebraic equations associated with the fluid-structure interaction problem can be written in matrix-vector format:

$$\underline{A}\,\underset{\sim}{b} = \underset{\sim}{c} \tag{D.9}$$

where the column $\underset{\sim}{b}$ is related to the entities that have to be solved, the matrix $\underline{A}$ is constructed from the element and control point contributions, and $\underset{\sim}{c}$ follows from the contribution of the boundary conditions to the loads on the elements. Because of the number of degrees of freedom ($\mathcal{O}(10^4 - 10^5)$) a linear direct solver would require inadmissible amounts of memory and CPU time and, therefore, a linear iterative solver is used. The robustness and effectiveness of an iterative solver decreases when the size and/or the condition number of the system matrix, $\kappa(\underline{A}) = \|\underline{A}\|\ \|\underline{A}^{-1}\|$, increases. The condition number will increase when the elements that are used to assemble $\underline{A}$ become distorted or when the different material parameters display large variations. This is one of the reasons why fully coupled procedures, as presented above, are sporadicly found in fluid-structure interaction applications, since both fluid and structure entities, which differ several orders of magnitude ($\mathcal{O}(10^9)$), are incorporated and the elements may become distorted. Moreover, the addition of the Lagrange multipliers to the system matrix involves addition of zero blocks on the main diagonal and an increase of the matrix bandwidth.

Using an fully coupled solution strategy for the mixed formulations of fluid and structural problem, i.e. the velocity and pressure fields ($\underset{\sim}{v}_f$, p_f) and ($\underset{\sim}{v}_s$, p_s) are solved

simultaneously, the system of equations defined by formulation (D.6) to (D.8) can be cast into the matrix-vector notation as described in Appendix A. The structure of this matrix is illustrated in Figure D.4 where the positions of nonzero entries in the matrix are shown. In Figure D.4(a) the fluid and structure degrees of freedom are ordered such that first all velocities are considered and subsequently all pressures. To improve the convergence properties of the matrix the degrees of freedom are renumbered per level, see Figure D.4(b), where a level is defined by the cluster of nodal points based on their spatial position in the domain (Segal, 2000). However, the solvability of the matrix is still in both cases significantly affected by the presence of the submatrices $\underline{\Lambda}_\alpha$ associated with the Lagrange multipliers. Elimination of the Lagrange multipliers from the fluid and structure matrix block (static condensation) could enhance the solvability of the matrix. Although this approach results in an additional off-diagonal block it is worthwhile to be considered in the near future.

Since this matrix is square and positive definite, but non-symmetric, a considerable restriction is posed on the iterative solvers that can be applied. The iterative solver that has been adopted here is based on the Bi Conjugate Gradient Stabilized (BiCGStab) method (Saad, 1996). The robustness and convergence rate of the BiCGStab solver is improved by using a preconditioner. The matrix-vector equation is then premultiplied with a preconditioning matrix $\underline{P}$ (not to be confused with the divergence matrix $\underline{\mathrm{P}}_\alpha$) to render:

$$\underline{P}\,\underline{A}\,\underline{\tilde{b}} = \underline{P}\,\underline{\tilde{c}}. \tag{D.10}$$

The purpose of this preconditioning is to reduce the condition number of the linear system and thus increase the convergence of the iterative solver. The ideal preconditioning matrix is $\underline{P} = \underline{A}^{-1}$, because this matrix renders the solution immediately, as for a direct solver. The preconditioner used here is of the type ILU based on an incomplete factorization of the system matrix. A general Incomplete LU factorization process computes a sparse lower triangular matrix $\underline{L}$ and a sparse upper triangular matrix $\underline{U}$ so the residual

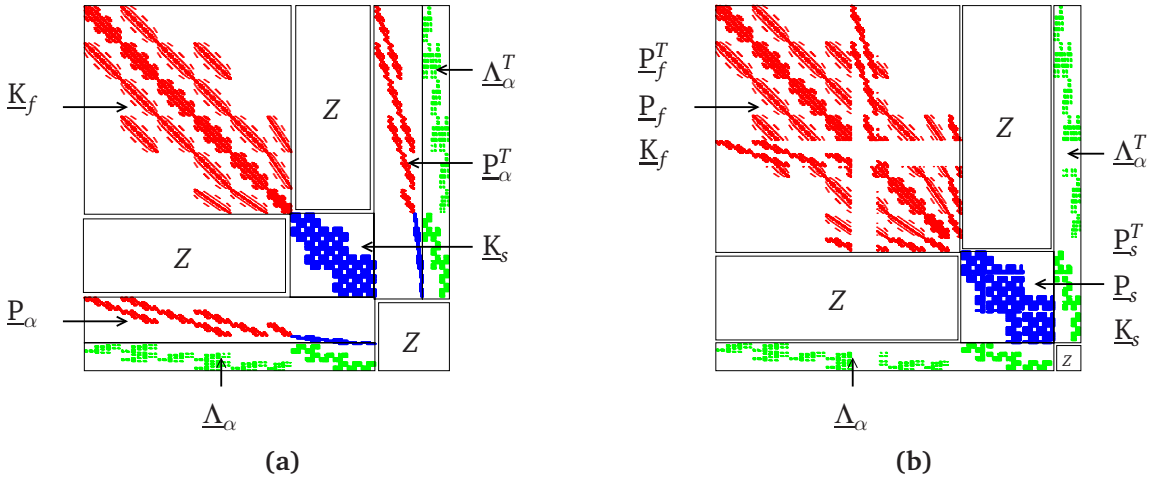

Figure D.4: *Structure of the system matrix for two different orderings of the degrees of freedom. See Appendix A for the explanation of the different submatrices. The subscript α denotes the fluid (f) and structure (s) submatrices.*

matrix $\underline{R} = \underline{L}\,\underline{U} - \underline{A}$ satisfies certain constraints, such as having zero entries at specific locations. To improve accuracy of the ILU factorization extra fill-in is allowed for $\underline{L}$ and $\underline{U}$. The main drawback of this method is the significant increase in the required memory and computational cost to build the preconditioner, which is not predictable. Moreover, the fill-in strategy is blind to numerical values and depends only on the structure of $\underline{A}$. To this end a threshold strategy is adopted for dropping small elements. For a detailed description of the dropping rules and fill-in strategy the reader is referred to Saad (1996).

References

Farhat, C., Lesoinne, M., LeTallec, P., 1998. Load and motion transfer algorithms for fluid/structure interaction problems with non-matching discrete interfaces: momentum and energy conservation, optimal discretization and application to aeroelastics. *Computer Methods in Applied Mechanics and Engineering*, **157**: 95-114.

Felippa, C.A., Park, K.-C., Farhat, C., 1998. Partitioned analysis of coupled systems. *Computational Mechanics, Proc. WCCM IV Conf.*, ed. by E. Oñate and S. Idelsohn, CIMNE, Barcelona.

Saad, Y., 1996. *Iterative Methods for Sparse Linear Systems*. PWS Publishing Company, Boston.

Segal, G., 2000. *SEPRAN Introduction, User's Manual, Programmer's Guide and Standard Problems*. Ingenieursbureau SEPRA, Leidschendam.

Wall, W.A., Ekkehard, R., 1998. Fluid-structure interaction based upon a stabilized (ALE) finite element method. *Computational Mechanics, Proc. WCCM IV Conf.*, ed. by E. Oñate and S. Idelsohn, CIMNE, Barcelona.

Samenvatting

Hartkleppen reguleren de unidirectionele stromingsrichting van het bloed door het lichaam. Elke ziekte van deze kleppen, die hun functionering beperkt, beïnvloed in sterke mate de gezondheidstoestand van het individu. De frequentie en medische consequentie van aandoeningen bij de aortaklep illustreren het belang van het correct functioneren van deze klep. De prestaties en duurzaamheid van de natuurlijke aortaklep kunnen echter (nog) niet geëvenaard worden door een vervangende klep. Onderzoek naar de medische complicaties in huidige klepprotheses is voornamelijk gebaseerd op dure en tijdrovende experimentele studies. Bovendien is de ontwikkeling van betere protheses grotendeels afhankelijk van empirisch vergaarde kennis. De toepassing van numerieke technieken kan deze ontwikkeling bevorderen door het aantal benodigde experimenten significant te reduceren en het inzicht in experimenteel moeilijk toegankelijke systeemresponsies te vergroten. Echter, gangbaar numeriek onderzoek is hoofdzakelijk gebaseerd op modellen, waarbij de interactie met het bloed wordt verwaarloosd. Deze interactie tussen bloed, klepvliezen, aortawortel en wand is essentieel voor het gedrag van de klep tijdens de systole hartfase. De klinische evaluatie van het functioneren van de klep dient dan ook gebaseerd te zijn op de mechanische eigenschappen van de klep en de dynamische interactie met de vloeistof.

Dit proefschrift beschrijft een vloeistof-vaste stof interactie model van de aortaklep dat gebaseerd is op de eindige-elementen methode. Met dit model is de invloed van vezelversterking van de vliezen en compliantie van de aortawortel op de klepkinematica en de vloeistofdynamica onderzocht. De ontwikkelde numerieke techniek maakt het mogelijk klinisch relevante problemen van de natuurlijke klep en klepprotheses te onderzoeken.

De modellering van de vloeistof-vaste stof interactie is complex door de grote verplaatsing van de klepvliezen door het vloeistofdomein. De mathematische representatie van de vloeistofbewegingsvergelijking wordt namelijk veelal beschreven in een Euler formulering, waarbij de ruimtelijk gefixeerde discretisatie geschikt is om stromingsverschijnselen te modelleren. Voor de vaste stof is een Lagrange beschrijvingswijze meer geschikt door de eindige beweging van het materiaal. Binnen deze formulering wordt de ruimtelijke discretisatie toegepast op het bewegende materiaal. Dientengevolge is de koppeling tussen de vloeistof en vaste stof discretisaties niet consistent gedurende de analyse. Technieken om de vloeistof discretisatie lokaal met de vaste stof mee te laten bewegen, zoals bijvoorbeeld remeshing of arbitrary Lagrange-Euler technieken, zijn, vanwege hun beperkingen, in deze studie niet gebruikt voor de interactie met de klepvliezen. In plaats daarvan wordt de ”fictitious domain” methode toegepast, waarbij met behulp van Lagrange multiplicatoren kinematische randvoorwaarden die de interactiekoppeling beschrijven, aan het systeem worden toegevoegd. De klassieke Euler

en Lagrange formuleringen voor de vloeistof en vaste stof blijven dan gehandhaafd. De fictitious domain methode is experimenteel gevalideerd met behulp van een tweedimensionaal klepmodel en blijkt geschikt te zijn voor de beschrijving van de interactie tussen het bloed en de klepvliezen. De interactie met de compliante aortawortel wordt correct beschreven met de gebruikelijke arbitrary Lagrange-Euler methode.

De geometrische eigenschappen van het numerieke model zijn gebaseerd op data genomen uit de literatuur. De vloeistof is gemodelleerd als een Newtonse vloeistof met bloedkarakteristieken. Het niet-lineaire, anisotrope materiaalgedrag van de klepvliezen is gemodelleerd met behulp van vezelversterking. Het materiaalgedrag van de aortawortel en wand is lineair elastisch en isotroop verondersteld. Stromings- en drukvariabelen zijn voorgeschreven aan het model en de bijbehorende Reynolds en Strouhal getallen zijn respectievelijk 1500 en 0.12.

De vloeistof en vaste stof variabelen worden simultaan opgelost en zijn dus direct in evenwicht. Een iteratief oplosschema om de twee fases aan elkaar te koppelen is daardoor overbodig. Met betrekking tot de bewegende aortawand wordt het vloeistof domein expliciet aangepast. Om evenwicht van het totale, niet-lineaire systeem te verkrijgen wordt gebruik gemaakt van het Newton-Raphson iteratie proces. Per iteratie slag worden de gelineariseerde vergelijkingen opgelost met behulp van de BiCGStab iteratieve solver, waarvoor een preconditioner gebaseerd op een incomplete LU factorisatie nodig is.

De toepassing van vezelversterking verbetert de mechanische eigenschappen van de klep aanzienlijk, terwijl de vloeistofdynamische eigenschappen behouden blijven. Het compliantie gedrag van de aortawortel blijkt een grote invloed te hebben op het openingsgedrag van de klep en beperkt in belangrijke mate de buigdeformaties van de klepvliezen. De combinatie van de fictitious domain en arbitrary Lagrange-Euler methode voor de interactie van het bloed met de klepvliezen, en de aortawortel en wand blijkt een geschikte manier om de systole klepfunctie te beschrijven. In diastole fase moet het aantal koppelingsvoorwaarden worden uitgebreid om stroming door de klep te voorkomen. Dit beïnvloed ernstig de oplosbaarheid van het systeem. Vloeistofdynamische effecten zijn echter van minder belang in deze fase en zijn bovendien goed te voorspellen met bestaande vaste stof modellen.

Concluderend kan worden gesteld dat het ontwikkelde model gebruikt kan worden als een numeriek ontwerpgereedschap om betere klepprotheses te maken. Bovendien lijkt het model in de toekomst gebruikt te kunnen worden in de kliniek om extra input te geven voor het bepalen van het moment en type chirurgische ingrepen met betrekking tot zieke aortakleppen.

Dankwoord

Ik heb moeten graven daar waar ik wilde grazen. Dat had ik nooit kunnen doen zonder de hulp en ondersteuning van een aantal mensen, waar ik mijn waardering voor uit wil spreken.

Mijn grote dank gaat uit naar Gerrit Peters, Piet Schreurs en Frank Baaijens. De discussies met Gerrit, die niet noodzakelijk betrekking hadden op het onderzoek, zijn belangrijk geweest voor de ontwikkelingen die ik de afgelopen jaren heb doorlopen. Piet heeft, door de rustiek in zijn methode en werkwijze, ervoor gezorgd dat ik niet te hard van stapel liep door mijn enthousiasme. De vastberadenheid van Frank om de fictitious domain methode toe te passen heeft uiteindelijk zijn vruchten afgeworpen.

Ik wil Veronica Papa bedanken, die met haar gedrevenheid in staat is geweest om de twee-dimensionale LDA experimenten een belangrijke waarde te geven binnen dit onderzoek. Alessandro Radealli heeft een eerste aanzet gegeven om de drie-dimensionale modellen experimenteel te valideren met PIV. Helaas konden deze resultaten niet passend in dit proefschrift opgenomen worden.

Naast alle collega's van de Materials Technology groep wil ik met name bedanken: Chris van Oijen, Marco Stijnen, Frans van de Vosse, Leo Wouters, Patrick van Brakel en degenen die hun bijdrage hebben geleverd bij het realiseren van de experimentele opstelling. De bereidwilligheid van Guus Segal en toegankelijkheid van SEPRAN heeft bovendien in belangrijke mate dit onderzoek bevorderd.

Voor de afwisselende en soms onzinnige discussies bedank ik mijn (oud)-kamergenoten: Mascha Maenhout, Hein Schellens, Bernard Schrauwen, Frank Swartjes en alle anderen die het woord kletspraat een nog ondiepere betekenis hebben gegeven.

Mijn dank gaat echter vooral uit naar mijn vader en moeder voor wie dit werk meestal moeilijk te begrijpen was maar desondanks altijd vertrouwen bleven hebben. Zonder hun bijdrage en ondersteuning was dit proefschrift nooit tot stand gekomen.

Jurgen de Hart,
Eindhoven, 1 maart 2002.